Spatio-Temporal Characterization of Arctic Landscapes Using Geospatial Analytics

A Dissertation Presented for the

Doctor of Philosophy

Degree

The University of Tennessee, Knoxville

Zachary Lance Langford

December 2017

© by Zachary Lance Langford, 2017
All Rights Reserved.

I dedicate this dissertation to my wife:

Scarlet Langford

and to my parents:

Chris and Melaina Langford

Abstract

Amplified warming in the Arctic has likely increased the rate of landscape change and disturbances in northern high latitude regions. Satellite remote sensing is a valuable tool for monitoring natural and anthropogenic changes occurring in remote, northern high latitude environments over multiple time scales. It offers the potential to characterize the vegetation, land cover, hydrology, geomorphology and permafrost characteristics of the Arctic landscape and improve and improve our understanding of changes these ecosystems are undergoing due to effect of natural and anthropogenic climate change and changing disturbance regimes. Combined with ground based observations of ecological processes, remote sensing offers opportunities for upscaling the ground based measurements to better understand the larger landscape.

In this dissertation research I have developed 1) new techniques for integration of remote sensing data set from a range of platforms with different spatial and temporal resolutions; 2) computationally efficient statistical and machine learning techniques to get ecological insights from large volumes of high dimensional remote sensing data; 3) methods to characterize and map vegetation characteristics at NGEE Arctic field sites in Alaska; and 4) techniques for identification and attribution of disturbance regimes in Alaska. In a close partnership with field ecologist, geospatial and machine learning techniques I have developed in this research has led to new insights and high resolution datasets of Arctic vegetation processes.

Table of Contents

1 Introduction **1**

1.1 Arctic Climate Change . . . 2

1.1.1 Role of Satellite Remote Sensing . . . 4

1.1.2 Geospatial Analytics . . . 5

1.2 Dissertation Objectives . . . 6

2 Mapping Arctic Plant Functional Type Distributions in the Barrow Environmental Observatory Using WorldView-2 and LiDAR Datasets **8**

2.1 Abstract . . . 9

2.2 Introduction . . . 10

2.3 Methodology . . . 14

2.3.1 Study area and datasets . . . 15

2.3.2 Characterizing the heterogeneous landscape . . . 21

2.3.3 Quantifying representativeness of field vegetation observations . . . 23

2.3.4 Statistical upscaling of PFT distribution on the landscape . . . 23

2.3.5 Validation of PFT upscaling . . . 25

2.4 Results . . . 27

2.4.1 Analysis of datasets . . . 27

2.4.2 Landscape characterization using unsupervised clustering . . . 30

2.4.3 Upscaling of PFT distributions . . . 31

2.4.4 Validation of upscaled PFT distribution . . . 35

2.5 Conclusions . . . 43

3 Convolutional Neural Network Approach for Mapping Arctic Vegetation using Multi-Sensor Remote Sensing Fusion **44**

3.1 Abstract . . . 45
3.2 Introduction . . . 46
3.3 Materials . . . 48
3.3.1 Study Area . . . 48
3.3.2 Remote Sensing Datasets . . . 49
3.3.3 Vegetation Data . . . 50
3.4 Methodology . . . 51
3.4.1 Data Processing . . . 51
3.4.2 Training Dataset . . . 53
3.4.3 Convolutional Neural Network . . . 54
3.5 Results and Discussion . . . 58
3.5.1 Patch-Level CNN Approach . . . 60
3.5.2 Pixel-Level CNN Approach . . . 62
3.5.3 CNN Architectures . . . 66
3.6 Conclusion . . . 67

4 Integrating Optical and SAR Datasets for Field-Scale Arctic Vegetation Mapping in the Seward Peninsula, Alaska **68**

4.1 Abstract . . . 69
4.2 Introduction . . . 70
4.3 Study Area . . . 74
4.4 Methodology . . . 75
4.4.1 Geospatial and *in situ* datasets . . . 76
4.4.2 Data Processing . . . 78
4.4.3 Unsupervised Classification based Vegetation Mapping . . . 81
4.4.4 Convolutional Neural Network Models for Vegetation Mapping . . . 83
4.4.5 Validation of vegetation maps . . . 84

4.5 Results . . . 85
4.5.1 Analysis of Remote Sensing Datasets . . . 85
4.5.2 Vegetation Classifications . . . 88
4.6 Discussion . . . 96
4.6.1 Importance of high-resolution datasets . . . 96
4.6.2 Vegetation classification . . . 98
4.7 Conclusions . . . 100

5 Wildfire Mapping in Interior Alaska Based on MODIS and Daymet Products 103
5.1 Abstract . . . 104
5.2 Introduction . . . 104
5.3 Study Area . . . 108
5.4 Methodology . . . 109
5.4.1 Geospatial Datasets . . . 109
5.4.2 Data processing . . . 111
5.4.3 Wildfire Mapping Algorithms . . . 112
5.5 Results . . . 114
5.5.1 Analyzing Spectral Variations . . . 114
5.5.2 Estimated Wildfires . . . 119
5.5.3 Identifying Best Features . . . 120
5.6 Discussion . . . 122
5.7 Conclusions . . . 124

6 Conclusion 126
6.1 Importance of Geospatial Analytics . . . 127
6.2 Incorporation of Field Samples . . . 129
6.3 Implications for Climate Studies . . . 129

Bibliography 131

Appendices 159

A Surface Water Analysis **160**

Vita **162**

List of Tables

2.1 Areas A, B, C, D polygonal features and environmental characteristics. . . . 17

2.2 The 6 and 31 characteristics used in the k-means clustering algorithm for the without and with phenology classification, respectively. 22

2.3 Number of vegetation samples partitioned by the k clusters, with the top k values representing the cluster number when setting the initial k values from 3 to 10 (left column). 25

2.4 R^2, Adjusted R^2, and Akaike information criterion (AIC) performed on the field data and the WorldView-2 spectral characteristics. 27

2.5 Mean and standard deviations of observed PFT distributions at areas A, B, C, and D by polygonal feature (i.e., centers, edges, and troughs). 29

3.1 List of remote sensing datasets used in this study 50

3.2 Area of the AKEVT vegetation classes for the study region (343.72 km^2). . . 50

3.3 Multi-sensor vegetation classification cases 52

3.4 Accuracy values for the vegetation maps (UCVM) produced by the *Mapcurves* method using unsupervised classification at different levels (k) at 5 m and 12.5 m resolution, with cases with best scores indicated by bold font. 59

3.5 Accuracy of the patch-level CNNs using varying patch sizes (i.e., 6×6, 12×12, and 16×16) at 5 m and 12.5 m resolution using AKEVT and UCVM maps for training. 61

3.6 Accuracy values for the AKEVT and Mapcurves vegetation maps produced by U-Net varying by patch size (i.e., 16, 32, 64) at 5 m and 12.5 m resolution. 64

4.1 Area (km^2) of the AKEVT vegetation classes for the study region (SR) and the Kougarok watershed (KW). The crosswalk, number of plots, and the size of field plots by vegetation type are also presented. The gray columns indicate no data. 78
4.2 Multi-sensor vegetation classification cases 80
4.3 Spectral and topographic variables used in the optical- and SAR-derived classifications 81
4.4 Area of the D7 vegetation classes for the study region and the Kougarok watershed. 93
4.5 Comparison of the various vegetation maps developed for Case D7 against the 30 field vegetation plots. (AW: Alder-Willow Shrub; DL: Dryas/Lichen Dwarf Shrub Tundra; MS: Mixed Shrub-Sedge Tussock Tundra-Bog; NV: Non-Vegetated; SW: Sedge-Willow-Dryas Tundra, and W: Water). The highlighted areas indicate were the vegetation class identified by vegetation maps developed in our did not match observations from vegetation plots. . 102

5.1 Raster predictor variables used for the study. 111
5.2 List of the number of variables used in the study. 112
5.3 Number of pixels (500×500) used for training and testing the RF algorithm. 114

List of Figures

1.1 Average air temperature (°C) and projected air temperature for the decades spanning 2010-2039, 2040-2069, and 2070-2099. Data and maps for future time periods are based on a composite of projections from five GCMs (CCSM4, GFDL-CM3, GISS-E2-R, IPSL-CM5A-LR, and MRI-CGCM3) under the AR5-RCP 8.5. Data courtesy of Scenarios Network for Alaska and Arctic Planning (SNAP). 3

1.2 Map showing the burn extent for 2015 over Alaska. 5

2.1 Flowchart of the methods used in this study. 15

2.2 Natural-color composite WorldView-2 image from 3 August 2010, showing the study area within the Barrow Environmental Observatory (BEO) (yellow) and the LiDAR data extent for sampling areas A, B, C, and D. The spatial extent of each sampling area is 100 m $\times$ 100 m. NextView License ©2016 DigitalGlobe. 16

2.3 (a) Location of vegetation plots for sampling areas A, B, C, and D. (b) Area A vegetation plots, (c) showing the sampling by the polygonal features centers, edges, and troughs. (d) Field photos taken during the sampling campaign in late July 2012 for a center (left), edge (middle), and trough (right). The center plot consisted of 48.8 % wet tundra graminoids, 5 % mosses, and 47.5 % bare ground. The edge plot consisted of 59.8 % wet tundra graminoids, 11.5 % dry tundra graminoids, 2 % forbs, 9.7 % lichens, 25 % mosses, and 21.3 % bare ground. The troughs consisted of 24 % wet tundra graminoids and 85 % mosses. 20
2.4 Clustering based stratification of the landscape ($k = 6$) for the *with phenology* case for areas A, B, C, and D at 0.25 m resolution. 31
2.5 Density of PFT distribution for the *with phenology* case within sampling areas A (blue), B (red), C (black), and D (orange). 32
2.6 PFT estimation (%) for the *with phenology* case. The figure is structured as: (a) wet tundra graminoid estimation; (b) moss estimation; (c) lichen estimation; (d) forb estimation; (e) dry tundra graminoid estimation; and (f) bare ground estimation. 33
2.7 Distribution of PFTs for the *without phenology* classification from pixels within sampling areas A (blue), B (red), C (black), and D (orange). 34
2.8 PFT estimation (%) for the *without phenology* case. The figure is structured as: (a) wet tundra graminoid estimation; (b) moss estimation; (c) lichen estimation; (d) forb estimation; (e) dry tundra graminoid estimation; and (f) bare ground estimation. 34
2.9 Representativeness of the vegetation samples across the study region for the (a) *without phenology* and (b) *with phenology* cases, with whiter colors indicating well-represented values and darker colors indicating under-represented areas. 35
2.10 Difference from subtracting the *with phenology* and *without phenology* classifications of (a) mosses and (b) wet tundra graminoids. 36

2.11 Model validation statistics for estimated PFTs compared to ground-truthing observations for the (a) *with phenology* and (b) *without phenology* case (DTG: dry tundra graminoids; WTG: wet tundra graminoids). Error indicators are RMSE (Root Mean Squared Error) and MAE (Mean Absolute Error). The points are color coded by PFT; mosses are orange, lichens are green, forbs are blue, WTGs are black, and DTGs are red. 37
2.12 Model validation statistics for the (a) the improved model and (b) the original model for the *with phenology* case. (DTG: dry tundra graminoids; WTG: wet tundra graminoids) Error indicators are RMSE (Root Mean Squared Error) and MAE (Mean Absolute Error). The points are color coded by PFT; mosses are orange, lichens are green, forbs are blue, WTGs are black, and DTGs are red. 38
2.13 Density of PFT distributions using the improved model for areas A, B, C, D (blue) and larger study region (red). 39

3.1 Study area based on the EO-1 Hyperion footprint, showing (a) SPOT-5 false color image, (b) digital elevation model, and (c) vegetation classes. 49
3.2 Flowchart of the study for fusion of remote sensing datasets and to generate high-resolution vegetation maps. 51
3.3 Example architecture of a seven layer patch-based CNN model. A 12 by 12 crop of an image (with 200 bands) is presented as the input. This is convolved with 64 different 1^{st} layer filters, with a kernel size of 5×5, using pooling with stride 2. Similar operations are repeated in the following layers. The last two layers are fully connected, taking features from the top convolutional layer as inputs. The final layer is a softmax function, corresponding to the number of classes. 56

3.4 An example of the u-net pixel-based architecture from taking a 32×32 pixel patch with 200 bands. The architecture has a series of convolutional and max pooling layers when downsampling. Upsampling and feature concatenating, which means this process uses information from the previous layers, was performed. There is a constant number of 64 filters throughout the network. The final output feature maps are fed to a softmax classifier for pixel-wise classification. 57
3.5 (a) Unsupervised classification map (k=25) from using D14 (EO-1, Landsat 8 OLI, ALOS-1 PALSAR, SPOT-5, IfSAR); (b) The original AKEVT vegetation maps; (c) UCVM vegetation map generated using *Mapcurves* method; (d) and EO-1 Hyperion false color image. 59
3.6 CNN Model accuracies for D14. The green line represents the validation set (10% of data) and the blue line represents the training dataset (90% of data). 63
3.7 Model accuracies for D5. The green line represents the validation set (10% of data) and the blue line represents the training dataset (90% of data). . . . 65

4.1 The study area located on the Seward Peninsula, showing the 2.5 m SPOT 5 false-color image. The Kougarok watershed is located in the lower section of the SPOT 5 image, zoomed in images on the right show the vegetation plot localities and a publicly available 30 m Alaska Existing Vegetation Type (AKVET) (http://akevt.gina.alaska.edu/) map used in the study. 75
4.2 Steps applied for the processing of the remote sensing datasets to develop vegetation classifications. 76

4.3 Example architecture of a seven layer CNN model. A 12 by 12 crop of an image (with 200 bands) is presented as the input. This is convolved with 64 different 1^{st} layer filters, with a kernel size of 5 x 5, using pooling with stride 2. Similar operations are repeated in the following layers. The last two layers are fully connected, taking features from the top convolutional layer as inputs. The final layer is a softmax function, corresponding to the number of classes. 84
4.4 Spectral characteristics of the EO-1 Hyperion dataset (400-2500 nm) for each vegetation class. 86
4.5 Box-plots representing variation in the DNs of Landsat 8 (L8 B1-B9), SPOT-5 data (green, red, NIR), ALOS-1 PALSAR (HH and HV), and IfSAR elevation values. The values were segregated by vegetation type, where AW, DL, MS, NV, SW, and W stand for Alder-Willow Shrub, Dryas/Lichen Dwarf Shrub Tundra, Mixed Shrub-Sedge Tussock Tundra-Bog, Non-Vegetation, Sedge-Willow-Dryas Tundra, and Water, respectively. 87
4.6 (a) Cluster value of 50 for D7 for the study region. (b) The reclassed map of D7 k=50 when performing UCVM for the study region. (c) SPOT-5 false color image for the study region. (d) Kougarok watershed of k=50 for D7. (e) The reclassed map of D7 k=50 when performing UCVM for the Kougarok watershed. (f) SPOT-5 false color image for the Kougarok watershed. (g) EO-1 Hyperion false color image for the Kougarok watershed. (h) The AKEVT map for the Kougarok watershed. 89
4.7 Study region wide validation statistics for Cases D3 (EO-1, ALOS-1 PALSAR, IfSAR), D6 (EO-1, ALOS-1 PALSAR, Landsat 8 OLI, IfSAR), and D7 (EO-1, SPOT-5, Landsat 8 OLI, IfSAR) that performed best using k =10, 25, and 50 unsupervised clustering respectively. (AW: Alder-Willow Shrub; DL: Dryas/Lichen Dwarf Shrub Tundra; MS: Mixed Shrub-Sedge Tussock Tundra-Bog;, NV: Non-Vegetated; SW: Sedge-Willow-Dryas Tundra, and W: Water) 91

4.8 Validation statistics using field vegetation observations in the Kougarok watershed for Cases D4 (EO-1, SPOT-5, IfSAR), D4, and D7 (EO-1, SPOT-5, Landsat 8 OLI, IfSAR) that performed best using k = 10, 25, and 50 unsupervised clustering respectively. (AW: Alder-Willow Shrub; DL: Dryas/Lichen Dwarf Shrub Tundra; MS: Mixed Shrub-Sedge Tussock Tundra-Bogr;, NV: Non-Vegetated; SW: Sedge-Willow-Dryas Tundra, and W: Water) 92
4.9 Validation of the CNN models trained using AKEVT dataset (a–c) and UCVM dataset (d–f) within the study region. (AW: Alder-Willow Shrub; DL: Dryas/Lichen Dwarf Shrub Tundra; MS: Mixed Shrub-Sedge Tussock Tundra-Bogr;, NV: Non-Vegetated; SW: Sedge-Willow-Dryas Tundra, and W: Water) 94
4.10 CNN model model convergence through 100 epochs for patch size of 3×3. . 95
4.11 SPOT-5 false color image (a) and CNN vegetation map (b) surrounding the vegetation plots. 96
4.12 Validation statistics using field based vegetation observations for the CNN models trained using AKEVT dataset (a–c) and UCVM dataset (d–f) within the study region. (AW: Alder-Willow Shrub; DL: Dryas/Lichen Dwarf Shrub Tundra; MS: Mixed Shrub-Sedge Tussock Tundra-Bog;, NV: Non-Vegetated; SW: Sedge-Willow-Dryas Tundra, and W: Water) 97

5.1 Study area for this study (yellow lines) and the 2004 wildfire boundaries (red polygons). 108
5.2 Flowchart for the proposed study. 109
5.3 Area of wildfires across the study region from 2000 to 2015. 110
5.4 Boundary wildfire perimeter and location. 115
5.5 Time series of averaged MODIS surface reflectance (a) and LST (b) variables for the Boundary wildfire perimeter. The vertical line indicates the DOY (165) of the wildfire. 116
5.6 Daymet variables for the Boundary wildfire perimeter. 118

5.7 Precision, recall, and F1-score using the MODIS (a) and MODIS and Daymet (b) variables on the test dataset. The red boxes indicate the lowest scores and the blue boxes represents the highest scores. The color table is weighted to the values within each dataset. 119
5.8 Feature importance for the MODIS variables. 120
5.9 Feature importance for the MODIS and Daymet variables, with vp, tmin, tmax, swe, srad, prcp, and dayl indicating vapor pressure, minimum temperature, maximum temperature, snow-water equivalent, shortwave radiation, precipitation, and day length, respectively. 121
5.10 EVI responses for the Boundary wildfire. Three periods are shown: before the wildfire (9 June, 2004), 4 days after the wildfire (17 June, 2004), and 68 days after the wildfire (20 August, 2004). 122

A.1 NDSWI values for areas A, B, C, and D for 2010 WorldView-2 images (June 10, June 24, July 21, July 26, August 03, and August 04) and one WorldView-2 image in 2012 July 19. 161

Chapter 1

Introduction

1.1 Arctic Climate Change

In the Arctic and sub-Arctic regions, including Alaska, warming trends have been accelerating and the increased trend in surface temperature in the region over the past decade is twofold higher than that in the whole northern hemisphere [73]. The Arctic has emerged as an important focal point for the study of climate change due to the greatest regional warming on Earth in recent decades, with an 0.8°C increase since the 1880s [108]. By 2099, the increases in average surface air temperature in the Arctic are expected to range between 5°C and 6°C, nearly double the global average of 3°C based on a multi-model mean [73]. Observations also suggest that permafrost thaw is common in high-latitude ecosystems and is expected to drive changes in climate forcing through biogeochemical and biophysical feedbacks [79]. This is also due to Arctic amplification, which is a response to climate feedbacks (e.g., sea ice-temperature, permafrost-carbon) [107, 122, Grosse et al.]. Terrestrial carbon models indicate that the Arctic could shift from a sink to a source of carbon and amplifying climate change within the $21st$ century, as organic matter is decomposed and released to the atmosphere as carbon dioxide (CO_2) or methane (CH_4) [96, 86]. Projections of future permafrost degradation indicate that active layer thickness will increase and the areal extent of near-surface permafrost will decrease [146].

These interacting feedbacks will take place in an environment expected to undergo dramatic geomorphic change and landscape reorganization [142]. The combined effects of multiple positive feedbacks can explain much of the recent and suggested future Arctic warming [122]. Figure 1.1 shows the baseline (1961-1990) average air temperature (°C) and projected air temperature for the decades spanning 2010-2039, 2040-2069, and 2070-2099 based on climate models.

Arctic plant communities are also changing in response to warming in this region over recent decades [112, 127]. Vegetation changes in albedo have been documented [22] and will have climate impacts [112]. Model experiments in the Arctic demonstrate that the associated feedbacks with vegetation are positive, and failing to account for them in future climate studies may result in inaccurate projections [112]. For example, expansion

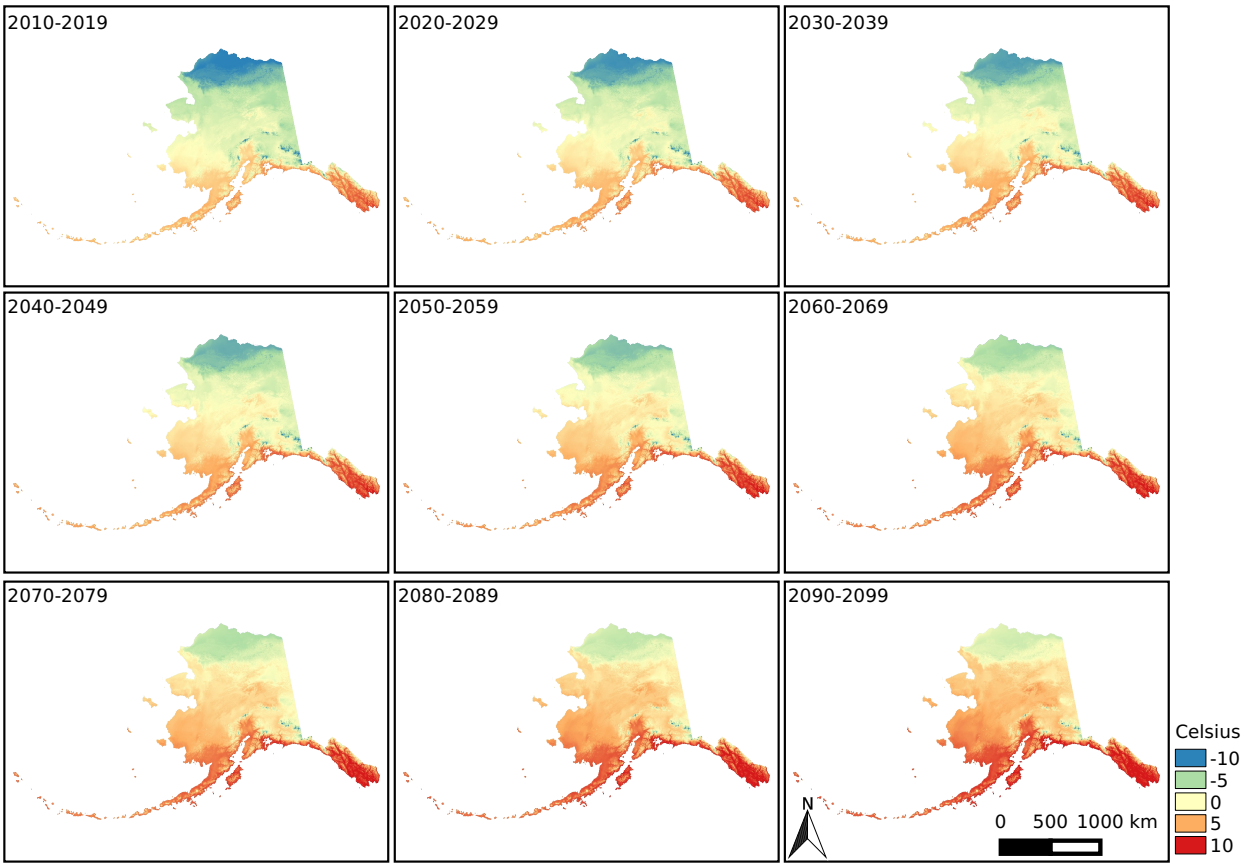


Figure 1.1: Average air temperature (°C) and projected air temperature for the decades spanning 2010-2039, 2040-2069, and 2070-2099. Data and maps for future time periods are based on a composite of projections from five GCMs (CCSM4, GFDL-CM3, GISS-E2-R, IPSL-CM5A-LR, and MRI-CGCM3) under the AR5-RCP 8.5. Data courtesy of Scenarios Network for Alaska and Arctic Planning (SNAP).

of woody shrubs and trees into the tundra biome will act as a positive feedback to climate warming through increased surface net short-wave radiation associated with reductions in albedo [22, 127]. Warmer conditions and increased atmospheric CO_2 will enhance plant growth that will remove some CO_2 from the atmosphere [147]. It is important to to adopt vegetation dynamics parameterisations that reflect climate feedbacks of Arctic plant types and communities to climate change.

Improving climate prediction in high-latitude ecosystems requires understanding of many complex systems of a changing geophysical system on vegetation, subsurface processes, land-atmospheric interactions, and landscape processes. The Department of

Energy's (DOE) Next-Generation Ecosystem Experiment (NGEE) Arctic seeks to address this challenge by quantifying the physical, chemical, and biological behavior of terrestrial ecosystems in Alaska [32]. NGEE Arctic seeks to build a scaling framework, based on field samples and remote sensing datasets, that will deliver a process-rich ecosystem model, extending from bedrock to the top of the atmosphere, in which the evolution of Arctic ecosystems in a changing climate can be modeled at the scale of a high resolution ESM grid cell (10 $\times$ 10 km grid size). New methods are needed for generating datasets for building and evaluating models in Arctic ecosystems.

1.1.1 Role of Satellite Remote Sensing

Satellite remote sensing provides an excellent tool for observing, documenting, and better understanding landscape change in the Arctic from local, to regional, to Pan-Arctic scales. Satellite remote sensing has successfully been used to detect and map thermokarst features [134], wetlands [25], active layer thickness [145], vegetation greening [41], and wildfires [76] over Alaska. Therefore, it's important to develop new remote sensing technologies for detecting near-surface and subsurface changes in the Arctic. For example, high-resolution satellite imagery (e.g., WorldView-2) is becoming more available and deriving parameters from these imagery could help drive models. The possibility of including realistic Arctic plant functional types (PFTs) derived from high-resolution imagery will provide a better representation of surface energy balance, physiology, nutrient interactions, and subsurface interactions between roots and permafrost [32].

The total burned area and frequency of large, naturally ignited fires has increased dramatically over the past four decades in Alaska [83]. Figure 1.2 shows the 2015 wildfire season in Alaska, where over 5 million acres burned. NASA's Moderate Resolution Imaging Spectroradiometer (MODIS) active fire products [80] have been used to help answer a broad range of scientific questions across Alaska [53, 174, 126].

Due to large characteristic differences between satellite sensors and their resolution, data from different remote sensing platforms are traditionally used independently in

ecosystem studies. Different sensors capture different aspect of land surface properties and vegetation and thus provides a unique opportunity to realize their individual strenghts. In this research I focus on multi-sensor fusion techniques using a range of available remote sensing platforms.

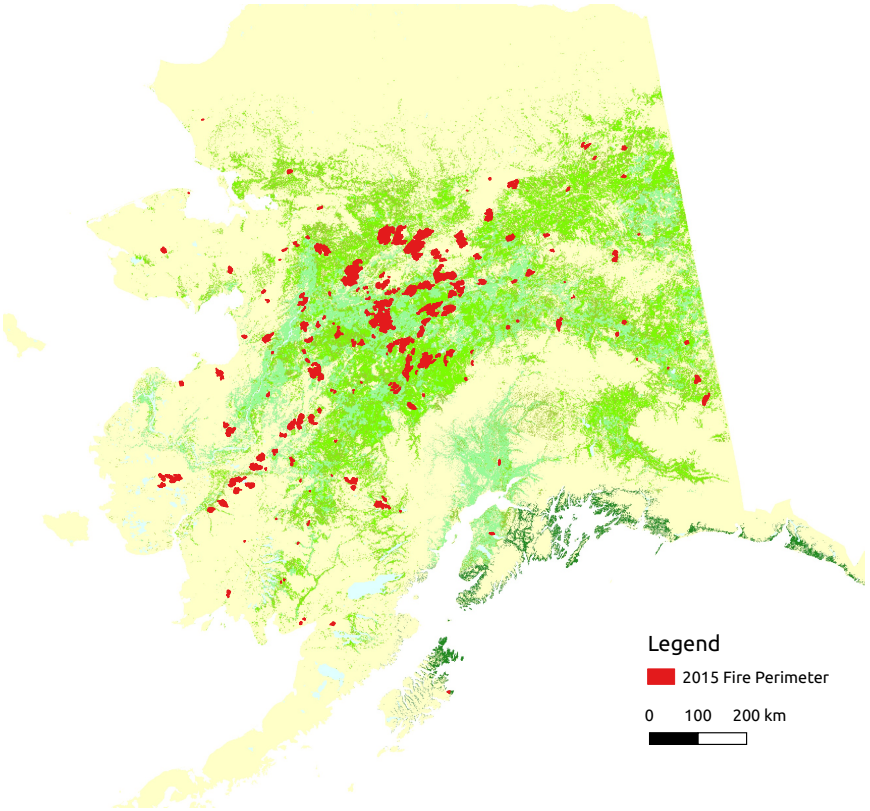


Figure 1.2: Map showing the burn extent for 2015 over Alaska.

1.1.2 Geospatial Analytics

A wide variety of data mining and machine learning techniques are now being applied to the growing body of Earth science data for Arctic research. Hoffman et al. [67] applied a multivariate spatio-temporal clustering analysis to derive ecoregions for Alaska using set of 37 climate, permafrost and topographic properties. That study was used to identify field sites for NGEE–Arctic. Ueyama et al. [170] upscaled carbon dioxide (CO_2) fluxes from a network of 21 eddy covariance towers to estimate the Alaskan CO_2 budget from

2000 to 2011 by combining satellite remote sensing data, disturbance information, and a support vector regression model. These studies indicate the importance for sophisticated techniques for ongoing monitoring and modeling efforts associated with Arctic climate change.

Diversity of Arctic ecosystem, combined with the volume and complexity of data in Arctic calls development of new analytics techniques. In this research I develop new statistical, machine learning and deep learning algorithms and implementations to study Arctic vegetation.

1.2 Dissertation Objectives

This dissertation seeks to advance the research of satellite remote sensing for landscape characterization of Arctic related processes, with four main goals:

1. develop high resolution characterization of Arctic vegetation,
2. explore and realize the potential of remote sensing for understanding Arctic ecosystems,
3. develop new geospatial analytics techniques and deep learning methods or mapping and characterization of Arctic vegetation, and
4. develop improved understanding of disturbance dynamics and their climate stressors in Alaska.

In Chapter 2, I developed a technique for mapping of Plant Function Type (PFT) distribution within Barrow Environmental Observatory in Alaska at sub-meter resolution using WorldView-2 and LiDAR datasets. Using field based vegetation survey data for training, I developed accurate and high resolution of mapping of PFT distribution in polygonal tundra landscape. I validated the developed PFT distribution in field to iteratively improve the mapping through a optimal sampling design. In Chapter 3, I developed Convolutional Neural Network models for mapping vegetation at Seward

Peninsula of Alaska. In this study I explored the potential of multi-sensor fusion using hyper-spectral, optical, and radar remote sensing dataset. In Chapter 4, I validated the Convolutional Neural Network based vegetation maps for Seward Peninsula using field vegetation plots and analyzed the patterns of vegetation within Kougarok watershed. In Chapter 5, I developed a Random Forest approach using MODIS based remote sensing and DAYMET meteorology datasets to map wildfires in interior Alaska. I also analyzed the spectral signatures of the wildfire burned area before and after the wildfire and feature importance of variables in the Random Forest classifier.

Chapter 2

Mapping Arctic Plant Functional Type Distributions in the Barrow Environmental Observatory Using WorldView-2 and LiDAR Datasets

Langford, Z. L., Kumar, J., Hoffman, F. M., Norby, R. J., Wullschleger, S. D., Sloan, V. L., and Iversen, C. M. (2016). Mapping Arctic Plant Functional Type Distributions in the Barrow Environmental Observatory Using WorldView-2 and LiDAR Datasets. *Remote Sensing*, 8(9):733.

2.1 Abstract

Multi-scale modeling of Arctic tundra vegetation requires characterization of the heterogeneous tundra landscape, which includes representation of distinct plant functional types (PFTs). We combined high-resolution multi-spectral remote sensing imagery from the WorldView-2 satellite with Light Detecting and Ranging (LiDAR)-derived digital elevation models (DEM) to characterize the tundra landscape in and around the Barrow Environmental Observatory (BEO), a 3021 hectare research reserve located at the northern edge of the Alaskan Arctic Coastal Plain. Vegetation surveys were conducted during the growing season (June–August) of 2012 from 48 1 m $\times$ 1 m plots in the study region for estimating percent cover of PFTs (i.e., sedges, grasses, forbs, shrubs, lichens, and mosses). Statistical relationships were developed between spectral and topographic remote sensing characteristics and PFT fractions at the vegetation plots from field surveys. These derived relationships were employed to statistically upscale PFT fractions for our study region of 586 hectares at 0.25 m resolution around the sampling areas within the BEO, which was bounded by the LiDAR footprint. We employed an unsupervised clustering for stratification of this polygonal tundra landscape and used the clusters for segregating the field data for our upscaling algorithm over our study region, which was an Inverse Distance Weighted (IDW) interpolation. We describe two versions of PFT distribution maps upscaled by IDW from WorldView-2 imagery and LiDAR: 1) a version computed from a single image in the middle of the growing season and 2) a version computed from multiple images through the growing season. This approach allowed us to quantify the value of phenology for improving PFT distribution estimates. We also evaluated the representativeness of the field surveys by measuring the Euclidean distance between

every pixel. This guided the ground-truthing campaign in late-July of 2014 for addressing uncertainty based on representativeness analysis by selecting 24 1 m $\times$ 1 m plots that were well and poorly represented. Ground-truthing indicated that including phenology had a better accuracy ($R^2 = 0.75$, $RMSE = 9.94$) than the single image upscaling ($R^2 = 0.63$, $RMSE = 12.05$) predicted from IDW. We also updated our upscaling approach to include the 24 ground-truthing plots and a second ground-truthing campaign in late-August of 2014 indicated a better accuracy for the phenology model ($R^2 = 0.61$, $RMSE = 13.78$) then only using the original 48 plots for the phenology model ($R^2 = 0.23$, $RMSE = 17.49$). We believe that the cluster-based IDW upscaling approach and the representativeness analysis offers new insights for upscaling high-resolution data in fragmented landscapes. This analysis and approach provides PFT maps needed to inform land surface models in Arctic ecosystems.

2.2 Introduction

The Arctic has emerged as an important focal point for the study of climate change, with rates of recent climate warming approximately twice the global average [73]. Climate warming is projected to continue in this region with broad implications for sensitive tundra ecosystems and globally important climate feedbacks [2]. Observations also suggest that permafrost thaw is common in high-latitude ecosystems and is expected to drive changes in climate forcing through biogeochemical and biophysical feedbacks [79]. These interacting feedbacks will take place in an environment expected to undergo dramatic geomorphic change and landscape reorganization [142]. Increases in active-layer thickness at some locations have driven ecosystem responses, including changes in vegetation cover [63]. Changes in vegetation community composition and distribution can affect albedo and energy partitioning in the Arctic [63, 117]. Furthermore, recent studies indicate that the phenology of vegetation (the timing of processes throughout the growing season) is a primary indicator of the dynamic responses of terrestrial ecosystems to climate change [39].

Terrestrial vegetation plays an important role in the dynamics of the Earth system through water and energy exchange and is one of the largest sources of uncertainty in climate change predictions [185]. In the Community Land Model (CLM), a component of the Community Earth System Model (CESM), as with most other models [185], vegetation is not represented as biomes but rather as plant functional types (PFTs) [120]. Each PFT groups plant species that share similar responses to environmental factors and effects on ecosystems [156, 162]. Most climate models currently use only two PFTs (one grass and one shrub type) to represent Arctic vegetation, greatly limiting the representation of plant functions and feedbacks in simulating Arctic responses to a warming climate [120]. Chapin et al. [21, 20] recommended the use of Arctic- and boreal-specific PFTs in vegetation models, including deciduous shrubs, evergreen shrubs, sedges, grasses, forbs, *Sphagnum* moss, non-*Sphagnum* moss and lichens, to capture Arctic vegetation processes.

Poulter et al. [130] showed that accurate PFT datasets are important for reducing the uncertainty of terrestrial biogeochemical processes to climate variability in Earth system models. Satellite datasets have been used to extract PFT information from the landscape and can contribute to improved predictive capabilities of land-atmosphere interactions [70]. Different remote sensing-based PFT products are available for Earth system models [162, 173, 130]. However, these products for parameterzing PFTs are at a coarse resolution (hundreds of meters to kilometers). New high resolution products are needed to capture the fine-scale heterogeneity of PFTs observed in the field.

There is a growing interest in understanding and resolving the subgrid scale processes in heterogeneous Arctic ecosystem. The U.S. Department of Energy's Office of Science Next Generation Ecosystem Experiments (NGEE) – Arctic project seeks to couple high-resolution models to Earth system models to represent Arctic land surface and subsurface processes and their interactions in a warming climate, such as high-resolution hydrologic (e.g., Arctic Terrestrial Simulator, PFLOTRAN) [3, 89], biogeochemical (PFLOTRAN) [165] and biosphere models (eg., CLM, CLM-PFLOTRAN) [165] can run at fine spatial and temporal resolutions and require high-resolution data sets. This need for parameterzing

high-resolution land surface models require new approaches for developing such high-resolution products.

Most optical remote sensing studies of Arctic vegetation consist of coarse resolution datasets from 30 m to 250 m [161, 149, 70] and few studies have been performed at the WorldView-2 resolution ($\sim$0.5 – $\sim$2 m) [4]. Medium resolution satellite datasets are useful for characterizing PFT coverage at regional to global scales, but there are challenges to integrating such datasets with sparse small-scale point measurements for upscaling. WorldView-2 multispectral satellite imagery has a much higher spatial resolution and can help capture the fine scale variation in PFTs.

There has been considerable recent progress in the development of methods for handling and analyzing high-resolution remote sensing data. Dalmayne et al. [28] used WorldView-2 satellite spectral dissimilarity to infer environmental heterogeneity in dry semi-natural grasslands, which revealed a significant positive association between spectral dissimilarity and fine-scale plant species beta diversity. Ramoelo et al. [132] monitored leaf N and above-ground biomass as an indicator of rangeland quality and quantity using WorldView-2 satellite images and random forest technique. Karna et al. [81] integrated WorldView-2 satellite image with small footprint airborne LiDAR data for estimation of tree carbon at species level. Mutanga et al. [116] demonstrated the utility of WorldView-2 imagery and random forest regression in estimating and mapping vegetation biomass at high density. Gangodagamage et al. [45] used LiDAR and WorldView-2 data to show variability in active layer thickness and the controls of local microtopography in Barrow, AK. These studies suggest that high spatial resolution data, such as WorldView-2 and LiDAR data, may potentially contribute to the development of improved methods for mapping and monitoring of vegetation at fine scales and use for high-resolution land surface models.

Phenology, seasonal changes in plants and animals from year to year, can be a useful proxy for monitoring vegetation [137]. Remote sensing phenology studies use data gathered by satellite sensors that measure wavelengths of light absorbed and reflected by green plants. Several remote sensing studies of phenology use satellites to track

seasonal changes in vegetation on regional, continental, and global scales [114, 180]. However, very few studies have used high-resolution (e.g., WorldView-2/3) image time series for understanding seasonal patterns in reflectance that can enable detection and change of vegetation at fine spatial scales. It's important to develop analysis techniques to capitalize on rich time series of imagery from high-resolution sensors as they become more available. In this study, we hypothesize that capturing the vegetation phenology using repeat imagery from high-resolution satellite data will help improve the characterization of the PFT distributions at our study site.

In situ field measurements are made at relatively few and specific geographic points and are representative samples of regions of similar characteristics. To upscale the *in situ* field measurements at larger scales for estimating landscape-scale characteristics, the representativeness of those measurements must be quantified. A representativeness metric provides insight into coverage provides by the field samples, the selection of optimal sampling locations, and offer a quantitative approach for down-scaling of remote sensing data and extrapolation of measurements to unsampled domains [67]. Sampling in under-represented sites, guided by the representativeness metric, can lead improved accuracy in upscaling of measured quantity (PFTs in current study).

The objectives of this study are to (1) characterize the landscape using high-resolution multi-spectral WorldView-2 satellite imagery and LiDAR-derived DEM; (2) use an interpolation algorithm for upscaling vegetation surveys and creating gridded PFT datasets based on remote sensing imagery; (3) use salient differences in growing season phenology (timing and magnitude of greenness) to help discriminate among various PFTs; (4) quantify the uncertainty in gridded estimates of PFT distributions upscaled from point observations using a representativeness metric; (5) devise optimal sampling strategies for ground-truthing and to improve PFT estimates and reduce uncertainty.

Interpolation is a process of using measurements about a process at a limited number of point locations to make estimates about the process at other, unmeasured locations. In this study, the term upscaling is defined as a interpolation process to employ point measurements to develop gridded estimates. An important objective was to develop

new data analytic approach to mine high resolution spectral remote sensing data sets for signatures of surface vegetation to develop estimates of PFT distributions at high spatial resolution (0.25 m $\times$ 0.25 m) across fragmented Arctic landscape.

2.3 Methodology

The methodology section follows the structure shown in Figure 2.1. Section 2.3.1 describes the study sites (Section 2.3.1), field vegetation surveys (Section 2.3.1), and the remote sensing datasets used in this study (Section 2.3.1). The k-means algorithm for stratifying the heterogeneous landscape using remote sensing data sets is described in Section 2.3.2. Section 2.3.3 describes the methodology to quantify the representativeness of the field vegetation surveys in context of larger study region. Section 2.3.4 presents the approach for statistically upscaling the PFT distribution on the landscape using the clusters from Section 2.3.2. Section 2.3.5 describes the approach for validation of the upscaled PFT distributions using a bootstrapping approach (Section 2.3.5) and on the ground via additional field surveys (Section 2.3.5).

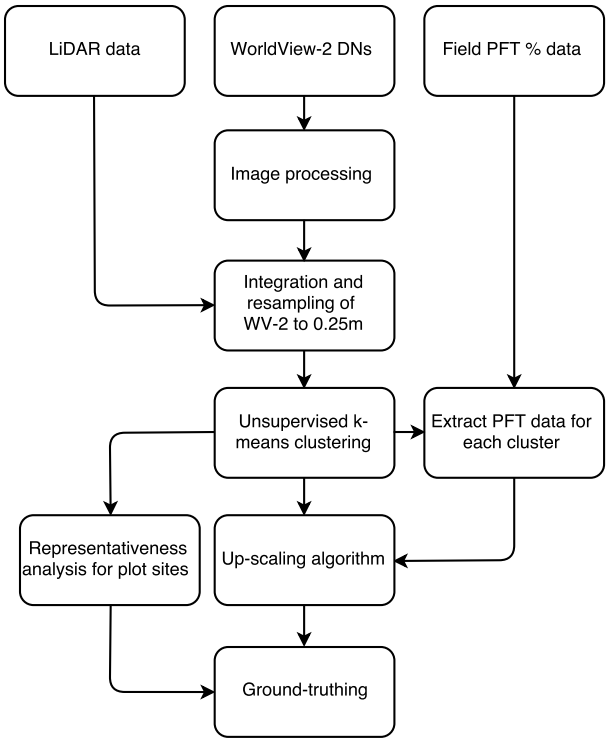


Figure 2.1: Flowchart of the methods used in this study.

2.3.1 Study area and datasets

Study area

The study area is located within the Barrow Environmental Observatory (BEO) located 6 km east of Barrow, Alaska (71.3°N, 156.5°W), as part of the U.S. Department of Energy's Office of Science Next Generation Ecosystem Experiments (NGEE) – Arctic project (Figure 2.2). The NGEE Arctic project (http://ngee-arctic.ornl.gov/) seeks to reduce uncertainty in climate prediction by better understanding critical land–atmosphere feedbacks in terrestrial ecosystems of Alaska. NGEE – Arctic has established four 100 m $\times$ 100 m intensively sampled areas (A, B, C and D, Figure 2.2; Table 2.1) within the BEO. The mean annual air temperature is -12°C and the mean temperature from June–August is 3.2°C [103]. The annual adjusted precipitation is 173 $mm\ yr^{-1}$ [103], with the majority of precipitation falling during the summer months. Soils on the BEO are generally classified as Gelisols, which are characterized by an organic-rich surface layer underlain by a horizon

of silty clay to silt-loam textured mineral material and a frozen organic-rich mineral layer. The seasonally active layer thickness ranges between 30 and 90 cm at the BEO [11, 69].

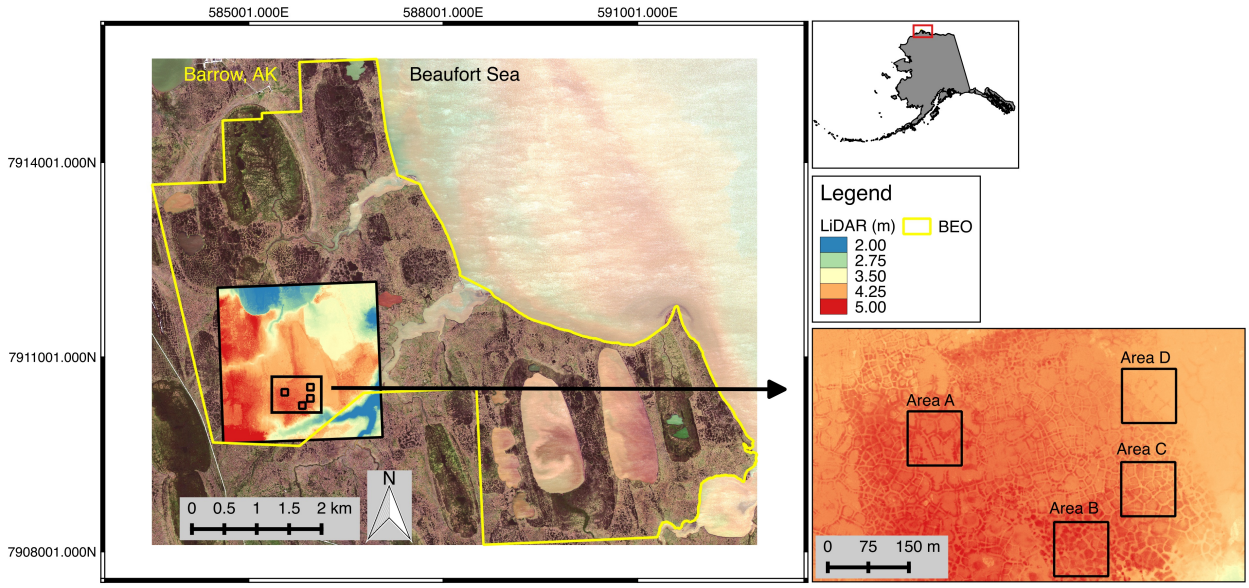


Figure 2.2: Natural-color composite WorldView-2 image from 3 August 2010, showing the study area within the Barrow Environmental Observatory (BEO) (yellow) and the LiDAR data extent for sampling areas A, B, C, and D. The spatial extent of each sampling area is 100 m $\times$ 100 m. NextView License ©2016 DigitalGlobe.

The BEO is a low relief landscape, with $< 7\ m$ differences in topography (Figure 2.2), and a low hydraulic gradient region characterized by thaw lakes and drained basins [17]. Seasonal freeze and thaw processes have produced a polygonal network of high centered polygons, low centered polygons, and transitional polygons [182]. Table 2.1 lists the polygonal characteristics for areas A, B, C, and D.

Table 2.1: Areas A, B, C, D polygonal features and environmental characteristics.

Area	Characteristics	Relative Elevation	Moisture Conditions
A	Low center polygons (with edges and troughs)	Low	Inundated
B	High center polygons	High	Desiccated
C	Transitional low center polygons (with edges and troughs)	Moderate	Moderately Dry
D	Low center polygons (few edges and troughs)	Low	Inundated

Field vegetation surveys

Plant community surveys were undertaken at 48 permanently marked 1 $m \times 1$ m plots in and around the four NGEE–Arctic sites (12 plots for areas A, B, C, and D) dominated by differing polygon types (Table 2.1; Figure 2.2). Plots were located in homogeneous vegetation communities in the centers, edges and troughs of four polygons per area, and the locations of the plot corners surveyed using dGPS. Aerial fractional coverages of all vascular, bryophyte and lichen species or genera, and bare ground were visually estimated by a single surveyor between July 17^{th} and 29^{th}, 2012. Rare species were assigned nominal values of 0.1 % (single individual), 1 % (multiple individuals) and 3 % (few individuals forming < 5 % coverage), and all remaining species recorded to the nearest 5 %. Canopies were considered to have two layers, with taller vascular plant coverage of up to 100 %, and a ground layer including some or all of mosses, lichens, prostrate vascular plants and bare ground with coverage of up to 100 %. Standing water was not present in any plots at the time of survey, although in polygon troughs moss and sedge vegetation was "floating" on saturated soil. Recorded species were assigned to PFTs using the descriptions of Chapin et al. [20], with the "grass" category modified here to "wet tundra graminoids" (to include true grasses such as *Dupontia fisheri*) and the "sedge" category to "dry tundra graminoids" (to include *Luzula spp.*). Fractional coverage of any PFT was the sum of all species in that category. Shrubs (deciduous and evergreen) were a very small component (mean of 1.27 %

for areas A, B, C, and D) of plant community composition across the study region and were thus omitted in this analysis.

Remote sensing datasets

We used cloud-free WorldView-2 satellite (DigitalGlobe) multispectral imagery (~2 m resolution) provided by the Polar Geospatial Center (PGC). The imagery was radiometrically corrected by DigitalGlobe and orthorectified by the PGC. We assume the geolocational error to be minimal, but some errors may be possible. We analyzed the *Blue* (450–510 nm), *Green* (510–581 nm), *Red* (630–690 nm), and *Near-Infrared (NIR)* (770–895 nm) bands. Images from 6 different days during the 2010 growing season (June 10, June 24, July 21, July 26, August 3 and August 4) were acquired to capture the vegetation phenology.

The 0.25 m spatial resolution LiDAR digital elevation model, DEM, used in this study was developed by AeroMetric, now known as Quantum Spatial, Inc., and flown on 4 October 2005. The DEM pixel values represent the ground elevation above sea level, with elevation values ranging from 0.00-7.06 m (mean 3.82 m). The DEM pixels show a mean difference of 0.003 meters (median = 0.004, RMSE = 0.043 meters) compared to survey data (n=286 points) collected in August 2006. More information on the LiDAR dataset can be found at http://dx.doi.org/10.5065/D6KS6PQ3. We assumed that the spatial variability of PFTs during WorldView-2 and LiDAR image collection in 2010 and 2005, respectively, were similar to the field surveys conducted during 2012 for comparison of remotely-sensed data with field observations.

We converted all WorldView-2 imagery to *top-of-atmosphere* (TOA) reflectance. TOA reflectance is the reflectance measured by the space-based sensor flying higher than the Earth's atmosphere. TOA reflectance does not account for topographic, atmospheric, or bidirectional reflectance distribution function (BRDF) differences. The pixel *Digital Numbers* (DNs) were converted to top-of-atmosphere band-averaged reflectance according to Updike and Comp [172].

A commonly used index for the estimation of vegetation properties using satellite remote sensing is the normalized difference vegetation index (NDVI). NDVI is based on the contrast between absorption in the *Red* band by chlorophyll pigments and reflectance in the *NIR* band caused by internal scattering within leaves [141]. NDVI calculated from different WorldView-2 satellite bands have been used for the estimation of fine-scale species diversity in semi-natural grasslands [28]. NDVI was calculated as:

$$\text{NDVI} = \frac{\rho_{\text{nir}} - \rho_{\text{red}}}{\rho_{\text{nir}} + \rho_{\text{red}}} \tag{2.1}$$

where ρ_{red} and ρ_{nir} stand for the TOA reflectance measurements acquired in the *Red* and *NIR* regions, respectively. TOA reflectance values vary between 0.0 and 1.0, thus NDVI varies between -1.0 (no vegetation) and $+1.0$ (green vegetation).

The WorldView-2 data sets were resampled to the LiDAR resolution of 0.25 m $\times$ 0.25 m, using the nearest-neighbor resampling algorithm. The spectral and topographic characteristics were extracted from the remote sensing datasets at the corners of the 48 field plots (192 plot corners) using Global Positioning System (GPS) coordinates. The spectral (WorldView-2) and topographic (LiDAR) characteristics varied on scales as small as 0.25 m $\times$ 0.25 m, and thus each of the 48 field vegetation plots can encompass multiple fine-scale topographic properties (Figure 2.3 c). To preserve and capture this heterogeneity, the PFT % values were extracted at the 192 plot corners. The PFT fraction used in the upscaling model consisted of percent averages for the 1 m $\times$ 1 m plot (Figure 2.3 d). The resampling of WorldView-2 and extraction of remote sensing data at the plot corners allowed for evaluating the topographic controls on the PFT upscaling.

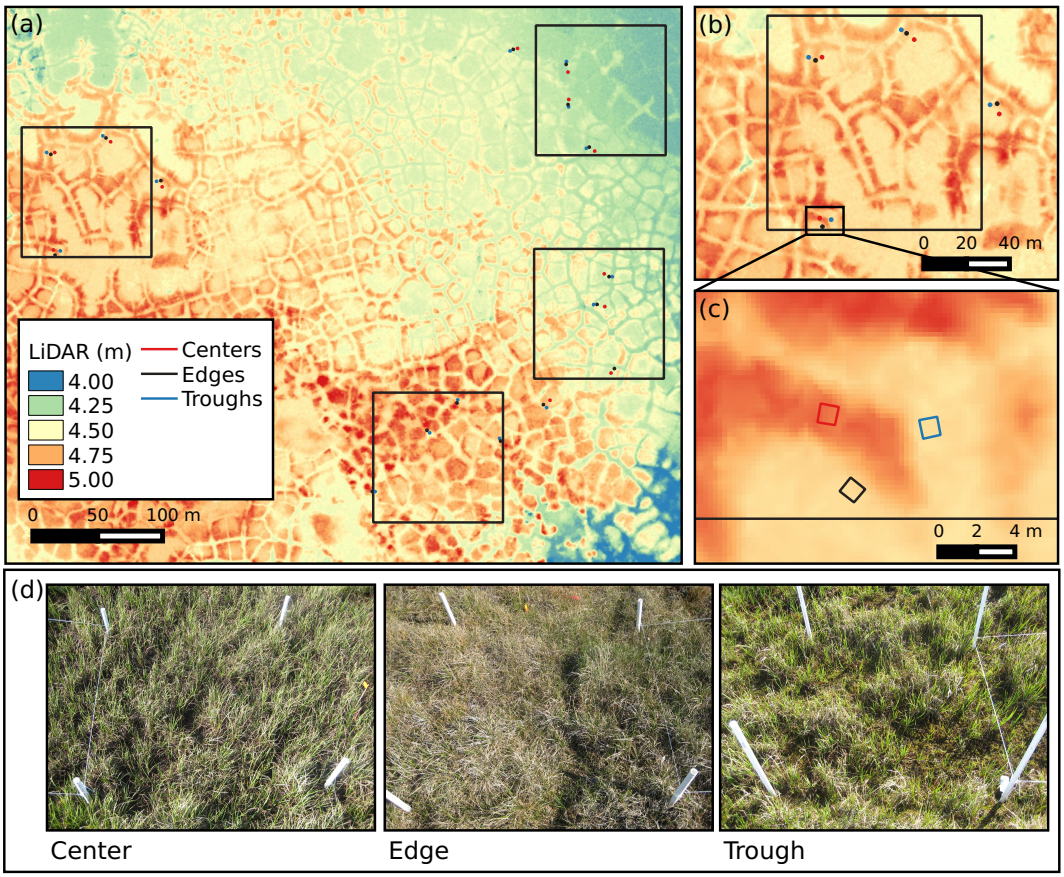


Figure 2.3: (a) Location of vegetation plots for sampling areas A, B, C, and D. (b) Area A vegetation plots, (c) showing the sampling by the polygonal features centers, edges, and troughs. (d) Field photos taken during the sampling campaign in late July 2012 for a center (left), edge (middle), and trough (right). The center plot consisted of 48.8 % wet tundra graminoids, 5 % mosses, and 47.5 % bare ground. The edge plot consisted of 59.8 % wet tundra graminoids, 11.5 % dry tundra graminoids, 2 % forbs, 9.7 % lichens, 25 % mosses, and 21.3 % bare ground. The troughs consisted of 24 % wet tundra graminoids and 85 % mosses.

2.3.2 Characterizing the heterogeneous landscape

Complex geomorphology, hydrology and biogeochemisty in the Arctic landscape leads to a highly heterogeneous distribution of vegetation on the landscape. These heterogeneities are captured by remote sensing as spectral responses of the vegetation. We characterize the landscape using remote sensing data sets to identify regions of similar characteristics. The classification of landscape would in turn allow development of accurate and specialized statistical models for upscaling of PFT distributions.

We used a k-means algorithm for stratification of the landscape using WorldView-2 and LiDAR datasets. Landscape classes determined by the algorithm, not directly used in upscaling process (Section 2.3.4), were only used as subregions for developing customized statistical upscaling model. The k-means algorithm clusters a dataset ($\vec{X}_1$, $\vec{X}_2$, ..., $\vec{X}_n$) with n records into a desired number of clusters, k, equalizing the full multi-dimensional variance across clusters [59]. The number of clusters, k, is supplied as an input and remains fixed. The k-means algorithm starts with initial centroid vectors ($\vec{C}_1$, $\vec{C}_2$, ..., $\vec{C}_k$) and calculates the Euclidean distance of each pixel ($\vec{X}_i$, $1 \leq i \leq n$) to every centroid ($\vec{C}_j$, $1 \leq j \leq k$), classifying it to the closest existing centroid. The centroid vector is recalculated as the vector mean of all dimensions of each pixel assigned to that centroid. This classification and re-calculation process is iteratively repeated until fewer than some fixed proportion of observations changes their cluster assignment between iterations. For this study, convergence was assumed once fewer than 0.05% of the observations change cluster assignments between two iterations.

Hoffman et al. [66] developed a parallel version of the k-means algorithm to accelerate convergence, handle empty cluster cases, and obtain initial centroids through a scalable implementation of the Bradley and Fayyad [14] method. Kumar et al. [90] extended this to a fully distributed and highly scalable parallel version of the k-means algorithm for analysis of very large datasets, which was used in this study.

One of the key hypotheses in this study was that phenology would help discriminate among various PFTs through salient differences in timing and magnitude of greenness

(NDVI) during the growing season. To test this hypothesis, two sets of analyses were conducted, *with* and *without* phenology. The *with phenology* case used a set of 31 characteristics at 0.25 m $\times$ 0.25 m resolution (Table 2.2). The characteristics included the blue, green, red, near-infrared bands and NDVI for the six snapshots from WorldView-2 during the growing season and the LiDAR elevation values. We found the LiDAR elevation values to be sufficient enough for capturing the microtopography effects on PFT patterns and thus we do not include other LiDAR metrics (e.g., slope and aspect) in the analysis.

For the *without phenology* case, a single WorldView-2 snapshot image from 21 July 2010 (middle of the growing season) that consisted of 6 characteristics (blue, green, red, near-infrared bands, NDVI, and LiDAR) was used. Both datasets were standardized such that each variable had a mean of zero and a standard deviation of one prior to clustering to equalize the contribution from each predictor variable. The remainder of the paper will refer to the multi-image analysis as "*with phenology*" and the analysis from a single image as "*without phenology*". The k-means clustering was performed on both sets of data to stratify the landscape at various levels of divisions (3 to 10). This was done for evaluating the the uncertainty associated with clusters and the upscaling algorithm.

Table 2.2: The 6 and 31 characteristics used in the k-means clustering algorithm for the without and with phenology classification, respectively.

Variables	Number of Variables (*without phenology*, *with phenology*)	Platform
Elevation	1, 1	LiDAR
TOA Red Band	1, 6	WorldView-2
TOA Blue Band	1, 6	WorldView-2
TOA Green Band	1, 6	WorldView-2
TOA NIR Band	1, 6	WorldView-2
NDVI	1, 6	WorldView-2

2.3.3 Quantifying representativeness of field vegetation observations

To statistically quantify the representativeness of field vegetation observations collected at the permanent plots at our site, we employ a representativeness metric described by Hargrove et al. [56] and Hoffman et al. [67] that provides a unit-less, relative measure of the dissimilarity and similarity in multi-variate data space between any two locations of interest. The representativeness metric was calculated for both the *with phenology* and the *without phenology* analysis (Table 2.2). This representativeness metric captures the full range of heterogeneity in the combinations of spectral and topographic conditions, providing a continuously varying measure of dissimilarity for every map cell with respect to any other map cell of interest. The representativeness metric is calculated as the Euclidean distance between field sampling location and any map cell/location of interest in the standardized n-dimensional state space. Areas with similar combinations of spectral and elevation characteristics will have a small Euclidean distance, representing a low dissimilarity value. Areas with very different combinations of characteristics will have a large Euclidean distance between them, and will have high dissimilarity values. The resulting map of representativeness quantifies, in multi-variate data space (Table 2.2), how well the set of field samples capture the heterogeneous landscape.

2.3.4 Statistical upscaling of PFT distribution on the landscape

Establishing relationships between remotely-sensed data and *in situ* observations can help extrapolate process understanding. Kriging-based extrapolation techniques have been widely used, however Arctic landscapes are often spatially fragmented due to geomorphological properties, rendering such methods not applicable. We were interested in an interpolation algorithm that used sparse, irregularly scattered data over a multidimensional domain, such as Inverse Distance Weighting (IDW). In IDW, the interpolating function is expressed as a weighted average of the data values, where the weights are inverse functions of the distances from the PFT sites in multi-dimensional data space. In an inverse interpolation scheme, an interpolated value is calculated as

$$\hat{z}(u) = \sum_{u_i \in \mathcal{N}(u)} w_i z(u_i) \tag{2.2}$$

where $\hat{z}$ represents the predicted PFT value, w_i represent weights, $z(u_i)$ is the input PFT percentages and variables listed in Table 2.2 and $\mathcal{N}(u)$ represents the neighborhood around u. $\mathcal{N}(u)$ can encompass the entire space so that all input samples contribute to the interpolated value. In IDW, the weights are set to

$$w_i = \frac{\gamma}{d_i(u)^2} \tag{2.3}$$

where γ is a normalization value chosen that $\sum w_i = 1$ and $d_i(u)$ is the Euclidean distance between u and u_i. The inverse interpolation scheme guarantees that each point in the output grid is assigned a predicted value [138].

We assumed that the k-means clustering can accurately stratify the fragmented landscape. In the IDW algorithm, $\mathcal{N}(u)$ was defined as the members of a given cluster, k, which uses input samples within the cluster (Table 2.3). That is, if $\bar{u}_k$ represents the mean state of cluster k, then $\mathcal{N}(\bar{u}_k)$ is the set of all points u_i included in cluster k. We believe that the landscape characterization performed by k-means clustering will lead to a better upscaling product when using the sampling points within each cluster. For example, if area C centers had high coverage of vascular PFTs, and using only the samples in the cluster that was associated with centers leads to a better classification of vascular PFTs in area C.

The IDW model was used for estimating wet tundra graminoids, dry tundra graminoids, forbs, mosses, lichens, and bare ground. For the upscaled PFTs, percent cover greater than 100 % refers to plot areas that have multiple layers of PFTs, while percent cover less than 100 % refers to areas that have some cover of standing water or standing dead vegetation. The upscaled PFTs were rescaled to 100 % and marked as standing water or standing dead vegetation for areas under 100 %. Appendix A describes how standing water was detected in the WorldView-2 satellite images and associated impacts on the upscaled estimations.

Table 2.3: Number of vegetation samples partitioned by the k clusters, with the top k values representing the cluster number when setting the initial k values from 3 to 10 (left column).

	Cluster Number									
k	1	2	3	4	5	6	7	8	9	10
3	116	1	75	–	–	–	–	–	–	–
4	115	1	76	0	–	–	–	–	–	–
5	79	68	44	0	1	–	–	–	–	–
6	0	0	63	49	79	1	–	–	–	–
7	54	50	1	65	0	22	0	–	–	–
8	0	22	0	54	1	65	50	0	–	–
9	0	55	51	45	4	18	19	0	0	–
10	33	26	0	1	50	0	0	10	54	18

2.3.5 Validation of PFT upscaling

Bootstrap validation

IDW was performed on $k = 3 \ldots 10$ for the *with phenology* and *without phenology* classifications. Bootstrap (random sampling) validation was used in order to evaluate how well IDW performed, which is essential due to strong autocorrelation at the sampling location. Bootstrapping creates an unbiased set, where every possible combination of sampling units has an equal and independent chance of being selected. 48 random samples (25 % of the plot corners) for wet tundra graminoids, dry tundra graminoids, forbs, mosses, lichens, and bare ground (total of 288 samples) were taken out for running IDW for $k = 3 \ldots 10$. This was performed for both the *without phenology* and *with phenology* cases. To allow for fair comparison, same set of randomly selected points were used for validation of both the cases. After running the IDW model, the estimated PFT values at the 48 held back locations were extracted and compared against the observation.

Ground–truthing

In addition to bootstrapping validation, an independent on-ground validation was performed by conducting field survey on July 29, 2014. The locations for field samples were strategically selected based on the representativeness analysis (Section 2.3.3). Within each sampling area (A, B, C, and D), three locations that were well-represented by the original field samples (determined by representativeness metric) were selected for field sampling. In addition, we also selected three locations at each of the four areas that were under-represented by the original vegetation samples. Thus, a total of 24 1 m $\times$ 1 m plots were selected for field sampling for validation of the upscaled PFT distribution products. High-resolution optical imagery was used to visually locate and extract plot coordinates across the various sampling areas. Similar to 48 1 m $\times$ 1 m plots, the 24 plots were surveyed using a dGPS. Unlike earlier survey of vegetation composition, no attempt was made to identify species or genera and only PFT measurements were made. Fractional area distributions of wet tundra graminoids, dry tundra graminoids, forbs, mosses, and lichens were determined in these 24 1 m $\times$ 1 m plots. All plots were sampled close to the peak growing season.

We expect the accuracy of the estimated PFT distributions at the plots well-represented by the vegetation samples to be better as compared to the plots that were under-represented. Representativeness metric helps identify the areas where additional observation can help improve the model. To test that hypothesis we added the observation at 24 well- and under-represented to the IDW model training data sets and repeated the analysis to generate a new estimate of PFT distribution. A second ground-truthing campaign was performed on August 30, 2014 at the same 24 plots using the same sampling strategy. Some senescence may have occurred by 30 August; however, it has been shown that the production of foliage can continue into late August in Barrow, AK [31]. The second ground-truthing serves to evaluate the estimation error when additional observations at well- and under-represented plots are included in the model development based on the field campaign on July 29, 2014.

2.4 Results

2.4.1 Analysis of datasets

While *without phenology* case used six variables, 31 variables were used for *with phenology* case (Table 2.2), significantly increasing the degrees of freedom and complexity of the model. We wanted to test the significance of adding extra variables (*with phenology*) to verify the benefit of added complexity. The *without phenology* and *with phenology* WorldView-2 variables (Table 2.2) were statistically compared to the field PFT data. The 192 points for the *without phenology* (n = 1152) and *with phenology* (n = 5952) were compared using multiple linear regression and Akaike information criterion (AIC). Table 2.4 shows the R^2, Adjusted R^2, and AIC for the *without phenology* and *with phenology* datasets on the PFT field data. All PFTs for the *with phenology* dataset shows higher R^2 and Adjusted R^2 and lower AIC. This gave us justification for using 31 variables in the IDW model.

Table 2.4: R^2, Adjusted R^2, and Akaike information criterion (AIC) performed on the field data and the WorldView-2 spectral characteristics.

	Without Phenology			*With Phenology*		
PFT %	R^2	Adjusted R^2	AIC	R^2	Adjusted R^2	AIC
Wet Tundra Graminoid	0.13	0.10	1575.00	0.58	0.50	1483.80
Dry Tundra Graminoid	0.34	0.32	1305.38	0.59	0.51	1263.48
Forb	0.26	0.23	1401.60	0.48	0.39	1380.26
Moss	0.26	0.24	1754.93	0.53	0.44	1717.31
Lichen	0.54	0.53	1393.88	0.75	0.70	1329.56
Bare Ground	0.37	0.35	1619.66	0.63	0.57	1563.31

Field vegetation observations collected in 2012 demonstrates a significant spatial variability in distribution of PFTs across the polygonal types and microtopographic locations. Wet tundra graminoids were most common in area A, while mosses were most common in area D (Table 2.5). Table 2.5 shows the mean and standard deviations of PFT fractions for areas A, B, C, and D by polygonal feature (centers, edges, and troughs).

Certain PFTs were most common in certain polygonal features. For example, forbs were most common in area C troughs and dry tundra graminoids were most common in area B centers. Analysis of NDVI values between June 10, 2010 and August 3, 2010 showed similar differences by polygonal feature for areas A, B, C, and D. Overall, lower NDVI values were associated with area A and higher NDVI values were associated with area C. This could be because of the moisture conditions (wet area A vs moderately dry area C) (Table 2.1) which drives the distribution of PFTs on the landscape.

Table 2.5: Mean and standard deviations of observed PFT distributions at areas A, B, C, and D by polygonal feature (i.e., centers, edges, and troughs).

PFT	*Centers*	*Edges*	*Troughs*
	M, SD	M, SD	M, SD
Wet Tundra Graminoids			
Area A	33.8, 12.1	45.2, 12.0	35.0, 7.8
Area B	2.6, 2.3	16.1, 11.0	24.2, 7.1
Area C	35.8, 21.0	10.7, 10.0	21.0, 12.1
Area D	25.5, 3.7	23.9, 7.9	35.8, 13.6
Dry Tundra Graminoids			
Area A	0.0, 0.0	6.0, 4.4	0.0, 0.0
Area B	23.3, 12.3	9.3, 5.1	2.1, 3.8
Area C	10.5, 12.6	13.7, 6.3	1.4, 1.2
Area D	2.5, 5.0	2.7, 1.9	0.2, 0.2
Forbs			
Area A	0.0, 0.0	3.3, 3.2	1.3, 2.6
Area B	1.5, 2.8	5.3, 5.8	11.0, 21.2
Area C	4.0, 2.7	9.0, 6.0	17.6, 22.1
Area D	2.3, 2.6	16.8, 11.0	1.3, 1.4
Mosses			
Area A	10.2, 5.3	48.1, 16.1	73.3, 18.6
Area B	19.0, 15.7	45.6, 7.1	53.3, 29.7
Area C	27.1, 22.0	61.3, 16.9	72.8, 20.8
Area D	41.0, 27.0	66.1, 14.1	73.2, 10.4
Lichens			
Area A	0.0, 0.0	16.4, 9.4	0.1, 0.1
Area B	37.3, 4.2	28.5, 7.2	1.2, 2.5
Area C	3.3, 1.8	16.3, 9.4	0.0, 0.0
Area D	0.1, 0.1	3.4, 4.6	0.0, 0.0
Bare Ground			
Area A	57.2, 10.0	5.3, 10.6	10.0, 14.1
Area B	14.3, 13.2	6.5, 5.7	15.3, 25.1
Area C	25.6, 15.3	8.1, 9.6	3.1, 6.2
Area D	30.6, 29.9	3.4, 3.7	1.5, 3.1

M = mean, SD = standard deviation
Wet tundra graminoids include *Dupontia fisheri* and dry tundra graminoids include *Luzula spp.*
Polygonal types: Area A: low centered polygon; Area B: high center polygons;
Area C: low centered polygon; Area D: low center polygons

2.4.2 Landscape characterization using unsupervised clustering

Unsupervised clustering was applied to the multi-variate data sets for *with phenology* and *without phenology* cases to stratify the landscapes at various levels of divisions ($k = 3 \ldots 10$). Bootstrap validation was performed for both the *without phenology* and *with phenology* cases (as described in Section 2.3.5). IDW models for estimating PFT distributions were developed for both *with phenology* and *without phenology* cased at each level of stratification ($k = 3 \ldots 10$) and they showed consistent coefficients of determination (R^2) ranging from 0.70 to 0.77.

The level of division of k = 6 (landscape stratified in six types) upscaled PFT distributions of wet tundra graminoids, dry tundra graminoids, forbs, mosses, lichens, and bare ground had the highest R^2 value for *with phenology* (0.77) and *without phenology* (0.76) cases using the bootstraping validation ($n = 288$). The choice of k = 6 was used for the remainder of the analysis presented in the paper.

Our results show that the patterns in the field-based distributions (Table 2.5) and the spectral variables used in the IDW model (Table 2.2) are significantly correlated with the polygonal features. The k-means clustering (k = 6) based stratification of the landscape well captured the polygonal microtopography (Figure 2.4) as demonstrated by the high correlation achieved during bootstrap validation (k = 6). For example, spectral characteristics of mosses may vary strongly between the polygon trough and edge, which would be delineated by topographic characteristics.

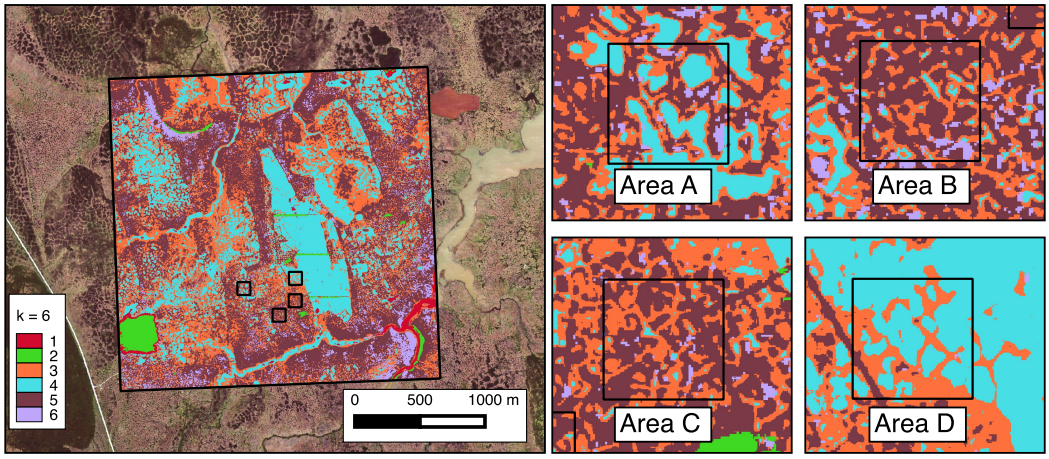


Figure 2.4: Clustering based stratification of the landscape (k = 6) for the *with phenology* case for areas A, B, C, and D at 0.25 m resolution.

2.4.3 Upscaling of PFT distributions

We developed and applied IDW model to upscale/estimate the distribution of PFT fractions across the footprint covered by the LiDAR data with a primary focus on the areas A, B, C, and D, each having an area of 0.01 km^2. Figure 2.5 shows the distribution density of all PFTs within areas A, B, C, and D (160,000 pixels) for the *with phenology* case. The IDW model (for *with phenology*) estimated that mosses had the highest percent cover for areas A, B, C, and D compared to other PFTs with mean values of 44.7 %, 46.9 %, 48.9 %, and 55.8 %, respectively.

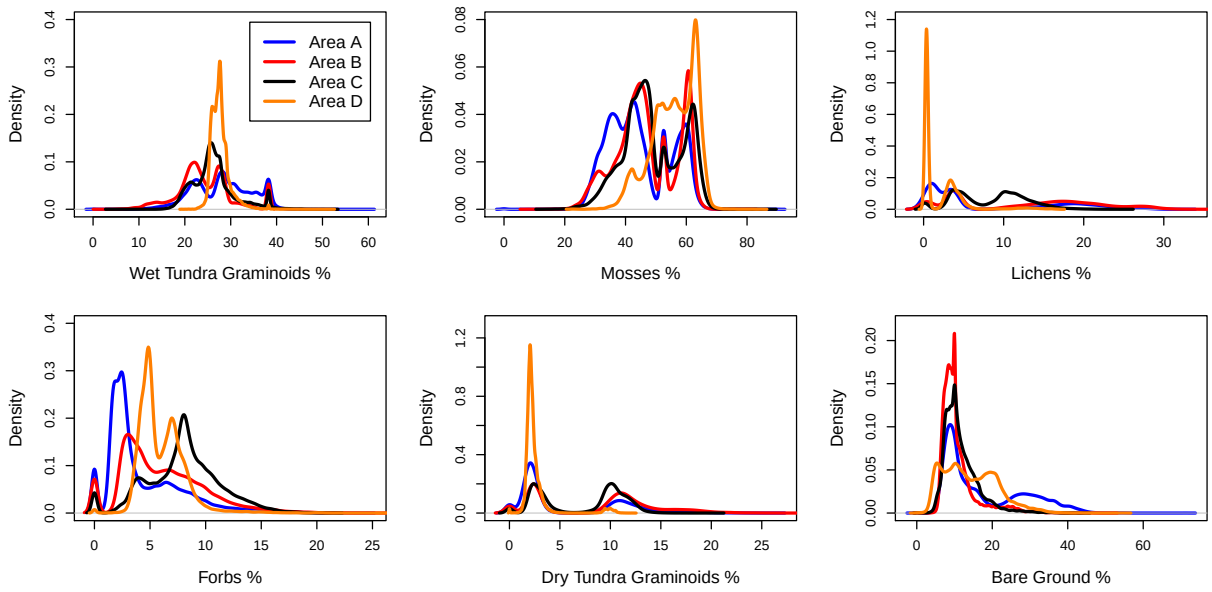


Figure 2.5: Density of PFT distribution for the *with phenology* case within sampling areas A (blue), B (red), C (black), and D (orange).

Wet tundra graminoids had the second highest percent cover for areas A, B, C, and D with mean values of 28.3 %, 24.1 %, 26.3 %, and 27.6 %, respectively. Bare ground had mean values of 17.5 %, 10.8 %, 11.6 %, and 14.3 % for areas A, B, C, and D, respectively. Lichens had mean values of 7.9 %, 12.5 %, 8.4 %, and 2.1 % for areas A, B, C, and D, respectively. Forbs had the lowest mean values of 4.3 %, 6.1 %, 8.1 %, and 6 % for areas A, B, C, and D, respectively. Analysis of PFT coverage suggested that the study areas have spatially heterogeneous distributions of PFTs, based on the different polygonal morphologies. For example, for the *with phenology* classification had higher wet tundra graminoid values were predicted for area A (Figure 2.6 a) and lower moss values predicted for area A (low centered polygons) (Figure 2.6 b).

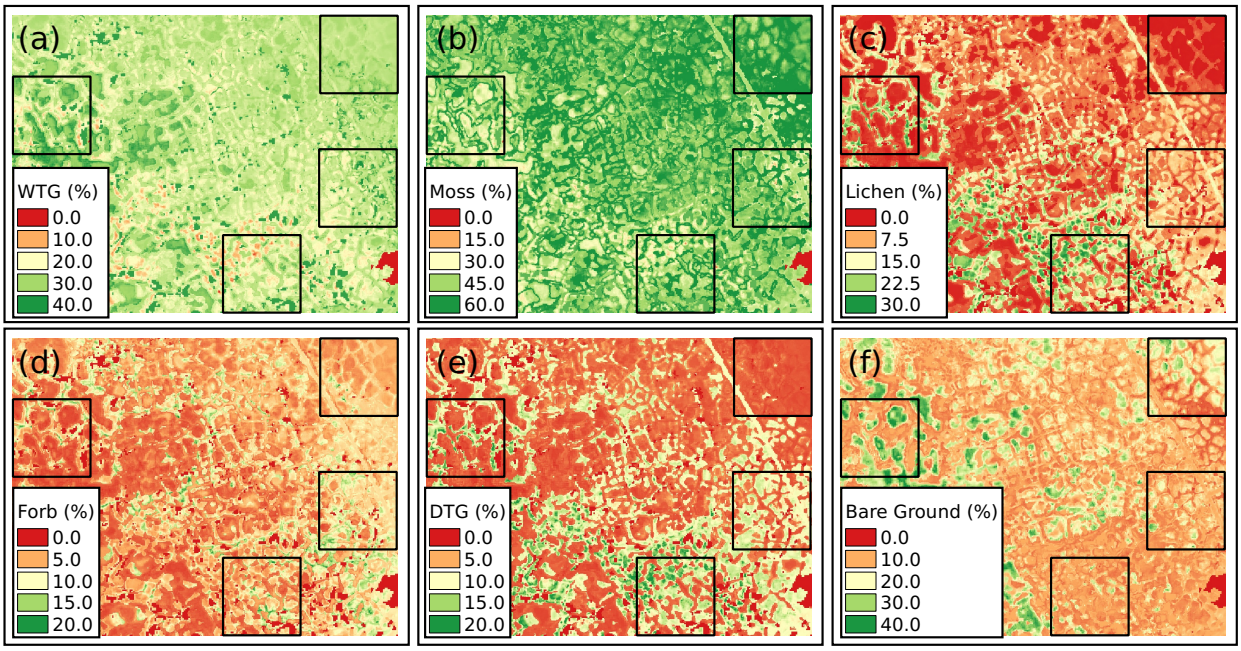


Figure 2.6: PFT estimation (%) for the *with phenology* case. The figure is structured as: (a) wet tundra graminoid estimation; (b) moss estimation; (c) lichen estimation; (d) forb estimation; (e) dry tundra graminoid estimation; and (f) bare ground estimation.

Figure 2.7 shows the average *without phenology* predicted PFT values for areas A, B, C, and D, which consists of 160,000 pixels. Results from the *without phenology* classification show PFT variability at both the polygon type and polygon feature scales. Bryophyte mosses were predicted to have the highest coverage in areas A, B, C, and D with mean values of 42.1 %, 44.8 %, 50.5 %, and 60.9 %, respectively. Wet tundra graminoids had the second highest coverage in areas A, B, C, and D with mean values of 30 %, 26.6 %, 27.1 %, and 27.9 %, respectively. Bare ground had mean values of 14.7 %, 12.9 %, 12.4 %, and 15.9 % for areas A, B, C, and D, respectively. Lichens had mean values of 9.7 %, 13.3 %, 7.3 %, and 1.4 % for areas A, B, C, and D, respectively. Dry tundra graminoids had mean values of 6.2 %, 8.5 %, 6.4 %, and 2.1 % for areas A, B, C, and D, respectively. Forbs had the lowest mean values of 4.4 %, 6.1 %, 8 %, and 7.3 % for areas A, B, C, and D, respectively. Figure 2.8 shows the spatial distribution for each PFT estimation for the *without phenology* case.

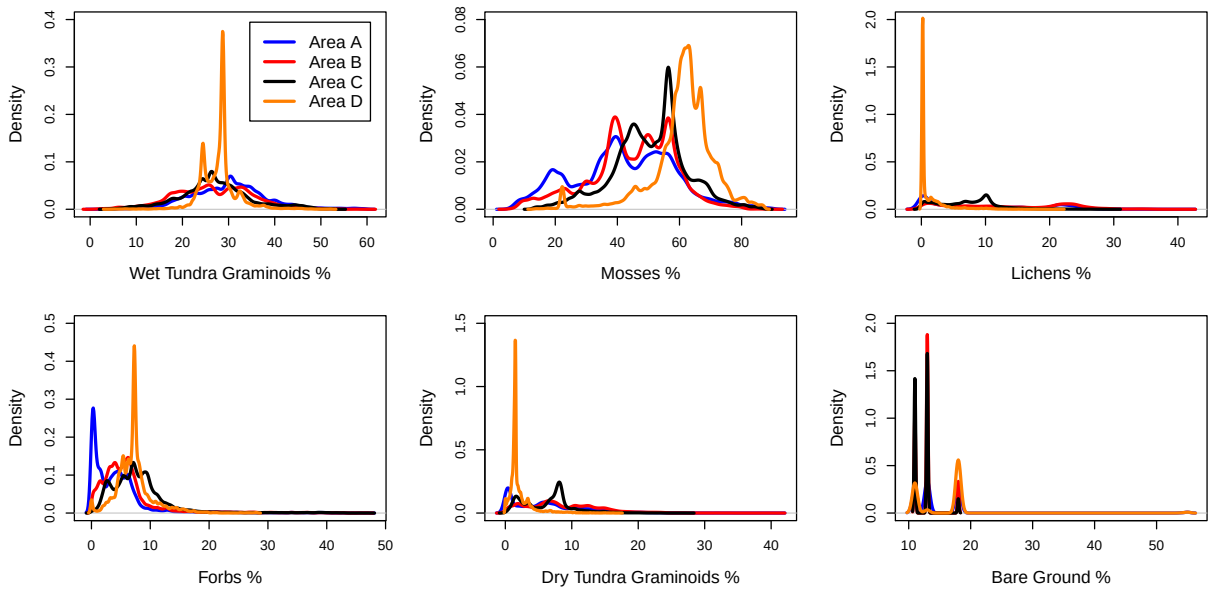


Figure 2.7: Distribution of PFTs for the *without phenology* classification from pixels within sampling areas A (blue), B (red), C (black), and D (orange).

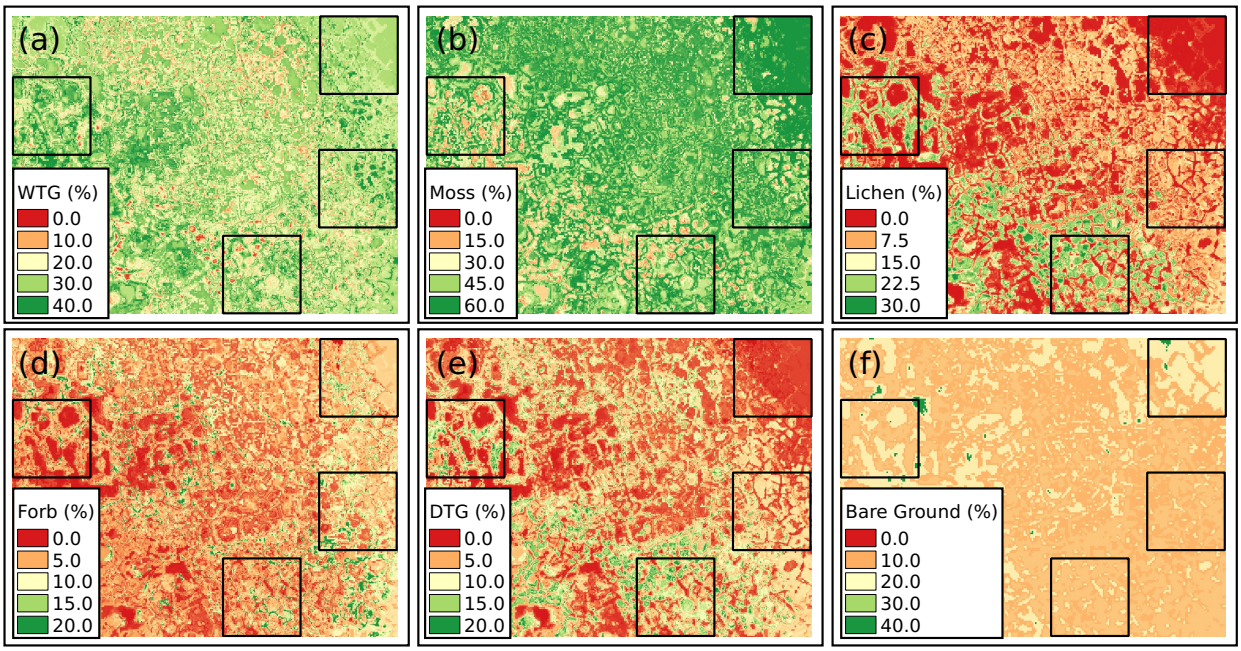


Figure 2.8: PFT estimation (%) for the *without phenology* case. The figure is structured as: (a) wet tundra graminoid estimation; (b) moss estimation; (c) lichen estimation; (d) forb estimation; (e) dry tundra graminoid estimation; and (f) bare ground estimation.

2.4.4 Validation of upscaled PFT distribution

Representativeness

Figure 2.9 shows the representativeness metric across the study areas A, B, C, and D for the *without phenology* (a) and *with phenology* (b) cases quantitatively representing how well the vegetation observations captured the variability in the multi-variate data space. The well-represented locations for areas A, B, C, and D had mean representativeness values of 1.71 and 0.35 for the *with phenology* and *without phenology* case, respectively. The under-represented locations for areas A, B, C, and D had mean representativeness values of 3.45 and 0.62 for the *with phenology* and *without phenology* case, respectively. The values of the representativeness metric for the *without phenology* case were lower because of the spectral similarities across data space when spectral data from a single date (i.e., 6 variables) during the growing season were used.

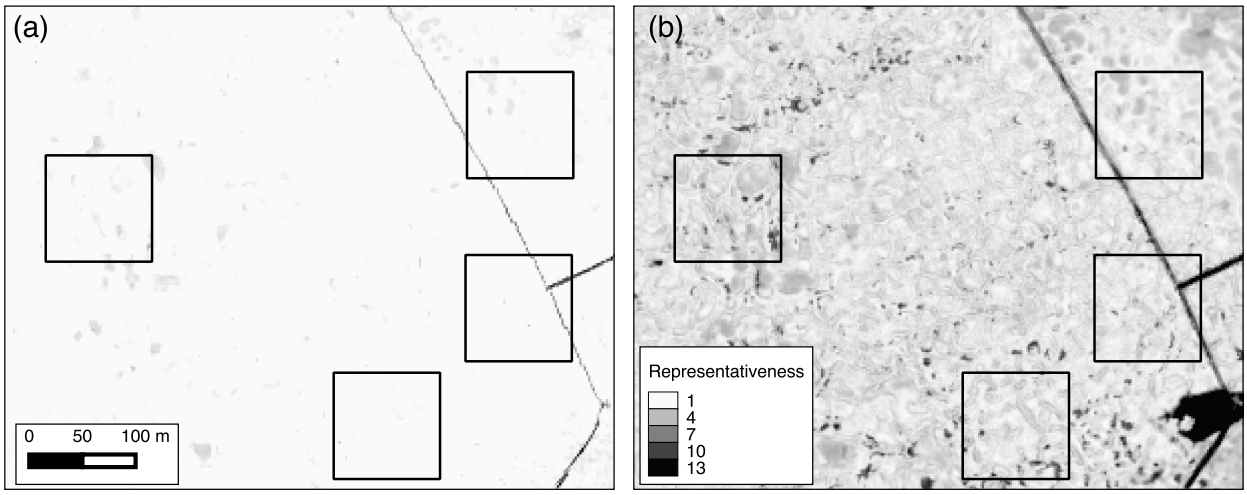


Figure 2.9: Representativeness of the vegetation samples across the study region for the (a) *without phenology* and (b) *with phenology* cases, with whiter colors indicating well-represented values and darker colors indicating under-represented areas.

To understand the difference in the estimated PFT distributions among two studied cases, difference maps were produced by subtracting the *with phenology* estimate from the *without phenology* estimate. Figure 2.10 shows the difference maps for moss (a) and wet tundra graminoid (b), with the greatest differences occurring in the under-represented

areas (Figure 2.9 b). Estimates of wet tundra graminoid and moss showed the greatest differences when including phenology, with mean absolute values of 5.9 % and 7.9 %, respectively. Forbs and dry tundra graminoids showed the lowest amount of difference, with mean absolute values of 2.7 % and 3.2 %, respectively. Lichens showed mean absolute differences of 4.1 %.

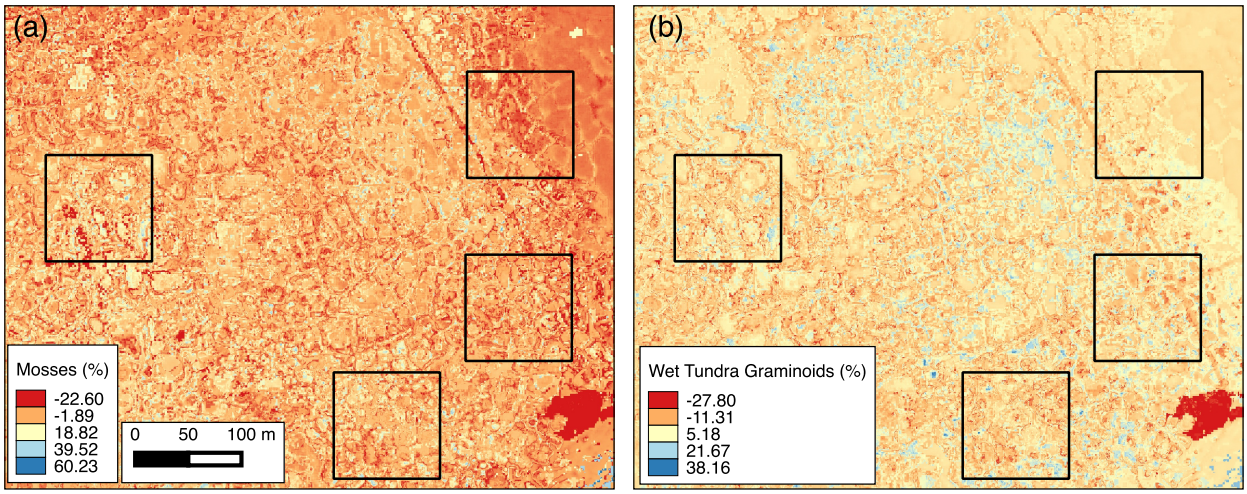


Figure 2.10: Difference from subtracting the *with phenology* and *without phenology* classifications of (a) mosses and (b) wet tundra graminoids.

Ground-truthing of the upscaled PFT distribution

The representativeness metric were used for the selection of sites for field-based ground-truthing (as described in Section 2.3.5). The mean PFT distributions at ground-truthing locations were similar to the PFT values from field observations conducted in 2012, which were used to train/develop the IDW model. For example, mean value for wet tundra graminoid for the ground-truthed data and input data into the IDW model was 25.9 % and 30 %, respectively. However, for some PFTs the range of the ground-truthed data wasn't as large as the 2012 PFT values. This could be due to a few sampling plots that had significant or less significant amount of PFT coverage.

Figure 2.11 shows the correlations and error statistics of the estimated PFT distributions for *with phenology* (a) and *without phenology* (b) cases (with all PFTs studies shown in different colors) compared against the 24 ground-truthed locations. The estimates from

with phenology case had better correlations and error statistics compared to the estimates from *without phenology* case. The slight differences in PFT distributions for different years and fewer sampling locations used during ground-truthing could be one of the reasons why some PFTs perform better than others. Wet tundra graminoids and mosses had the best correlation with the ground-truthing data for the *with phenology* case, which represent a large part of the landscape (Table 2.5). We infer that including multiple images during the growing season (capturing phenology) led to a better upscaling when compared to the *without phenology* case. Phenology appears to help discriminate various PFTs through salient differences in timing and magnitude of spectral information, reflecting differences in the timing of blooming and green-up during the growing season.

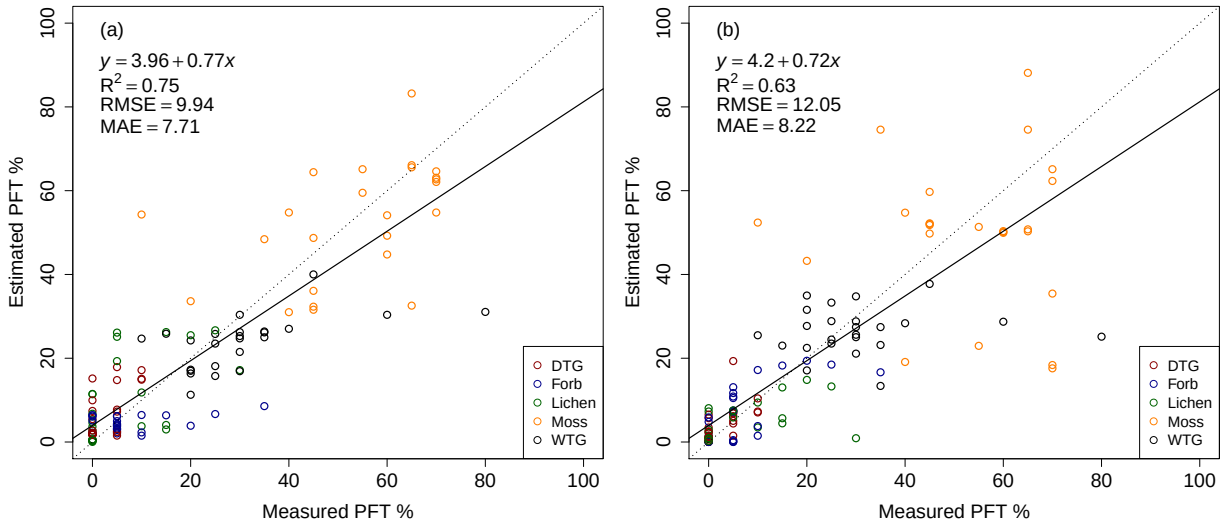


Figure 2.11: Model validation statistics for estimated PFTs compared to ground-truthing observations for the (a) *with phenology* and (b) *without phenology* case (DTG: dry tundra graminoids; WTG: wet tundra graminoids). Error indicators are RMSE (Root Mean Squared Error) and MAE (Mean Absolute Error). The points are color coded by PFT; mosses are orange, lichens are green, forbs are blue, WTGs are black, and DTGs are red.

Improving upscaling of PFTs using representativeness based sampling

The 24 ground-truthing locations were selected using representativeness, thus collecting 12 samples in the regions that were poorly sampled by the initial vegetation samples. The observations from the ground-truthing campaign were thus added to the training

set and the IDW model for all the PFTs for both the cases were recomputed. Including the 24 well- and under-represented ground-truthed sites (with the original PFT samples) in the IDW model improved the PFT estimation when performing the second ground-truthing campaign, with an $R^2 = 0.61$ compared to original model with an $R^2 = 0.23$ (Figure 2.12). Mosses underestimate and wet tundra graminoids overestimate the ground-truthing when using the original model.

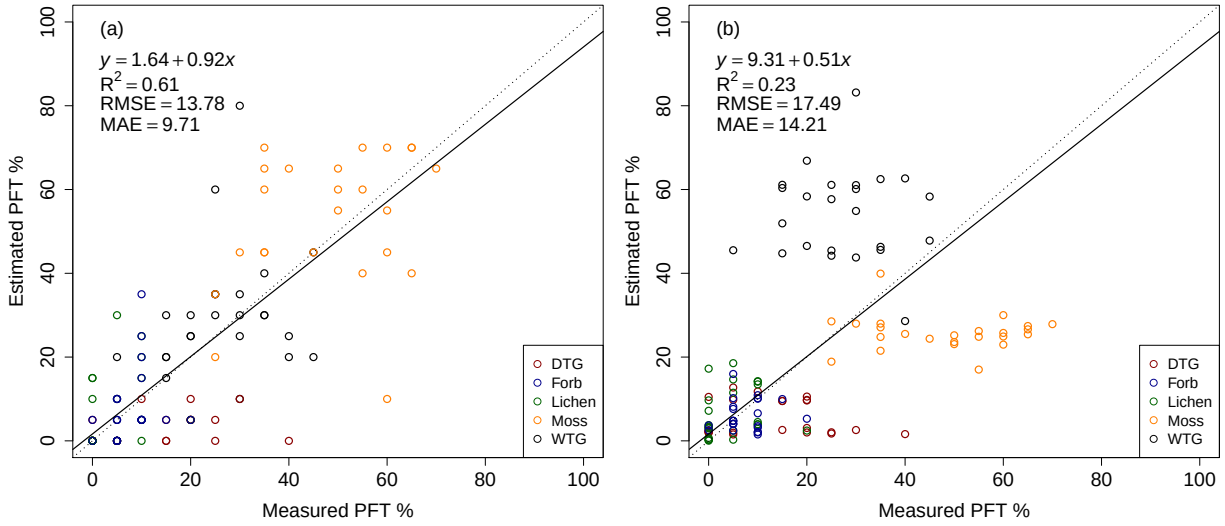


Figure 2.12: Model validation statistics for the (a) the improved model and (b) the original model for the *with phenology* case. (DTG: dry tundra graminoids; WTG: wet tundra graminoids) Error indicators are RMSE (Root Mean Squared Error) and MAE (Mean Absolute Error). The points are color coded by PFT; mosses are orange, lichens are green, forbs are blue, WTGs are black, and DTGs are red.

While we focused our discussion on the areas A, B, C, and D, our PFT upscaling was conducted over a larger region for which LiDAR data sets were available. Figure 2.13 shows the density distriution of PFTs for areas A, B, C, and D (160,000 pixels) in comparison to that for the larger study region defined by the LiDAR data extent (94,070,288 pixels). The distribution of PFTs for areas A, B, C, and D were similar to that for the larger study domain (Figure 2.13). The distribution shows relatively low proportions of lichens, dry tundra graminoids, and forbs and high proportions of wet tundra graminoids and mosses. Wet tundra graminoids had a mean value of 26.5 % for areas A, B, C, and D and the larger study domain, while mean values for mosses were 48.8 % and 46.9 %,

respectively. Accurate PFT maps over a large area are vital when running high-resolution land surface models (e.g., CLM) outside the sampling areas. This analysis could guide future field campaigns of vegetation sampling for extrapolating measurements over large areas in Arctic ecosystems. Our analysis indicates that including the representativeness analysis in the IDW model, by selecting sites that were not well represented, improved the estimated PFT distributions.

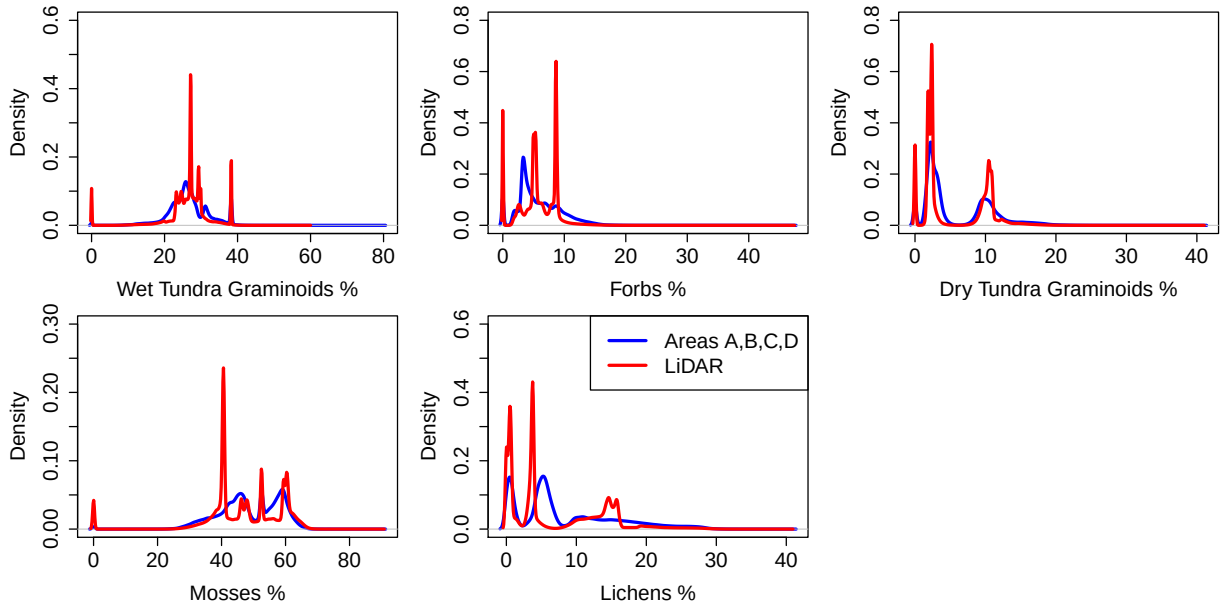


Figure 2.13: Density of PFT distributions using the improved model for areas A, B, C, D (blue) and larger study region (red).

High-resolution LiDAR and optical datasets are becoming more accessible and new approaches for analyzing such datasets are valuable to improving knowledge of Arctic ecosystems. This study estimated the distribution of PFTs using multiple high-resolution satellite imagery captured during the 2010 growing season. We developed an approach that combines k-means clustering [90], representativeness [56, 67], and interpolation methods for optimally using the sparse point measurements to develop continuous gridded PFT estimates; taking a different approach from previous studies.

WorldView-2 multispectral satellite imagery has a much higher resolution compared to commonly used satellites (e.g., Landsat, MODIS, etc.) and captures the fine-scale variation

in PFTs within a small sampling domain. Clustering the spectral and topographic characteristics together provided a systematic method for delineating the landscape and allowed for the development of better upscaling models using field observations from similar environment (in multi-variate data space). We conducted cluster analysis for varying level of divisions ($k = 3 \ldots 10$) with primary focus on stratifying the polygonal landscape. At our polygonal tundra sites with significant microtopography, cluster analysis at $k = 6$ level of division provided the best stratification of the landscape (Figure 2.4) and provided the highest correlation coefficient during the bootstap validation. For application to a different landscape, optimal level (k) for clustering based stratification can be adjusted to appropriately capture the heterogeneity and features of interest.

Data from the vegetation surveys (mid-July 2012) and first field ground-truthing campaign (late-July 2014) were very comparable, indicating similar vegetation conditions at the site during 2012 and 2014. The distribution of vegetation (PFTs) varies throughout the growing season, for example, early in the growing season standing biomass will be dominated by mosses and lichens, with the vascular plant component increasing as the season progresses [71]. Data indicates that including multiple images during seasonal growth, thus capturing phenology, captured this variance in our upscaling model. Including the targeted field observations at well- and under-represented sites collected as part of field based validation significantly improved the accuracy of PFT estimates. However, the R^2 was lower for the *with phenology* case (Figure 2.12 a) when compared to the first ground-truthing (Figure 2.11 a) exercise. Data shows that the second ground-truthing campaign was conducted in late-August 2014, while most the PFTs were beginning the “brown-down" period. Specifically, our *with phenology* IDW model captured the “green-up" period during the 2010 growing season and sufficient remote sensing data was not available to capture the “brown-down" period. Including more remote sensing images during the last part of the growing season would help capture the “brown-down" and, therefore, potentially further distinguish PFT distributions. Including the whole growing season in the PFT estimate may help represent dynamic PFTs for models.

IDW works well with high-resolution remote sensing datasets. In addition, by stratifying the landscape using cluster analysis, and developing separate model with each cluster and using the observations within the cluster allowed for spectral similarity and thus better and specialized models. The results of this study are applicable to the regions with similar vegetation and spectral characteristics. Also, this study is well suited for upscaling fine-scale measurements over areas similar to the BEO. For example, clouds may become an issue if one decides to study larger areas. However, the same approach could be applied to cloud-penetrating L-band Synthetic Aperture Radar or to a subset of imagery throughout the growing season.

The distribution of PFTs for areas A, B, C, and D shows a multimodal distribution, which could be due to the polygonal types and features and was also attributable to how observers estimated plant distributions by multiples of 5 or 10 % (Figure 2.13). For example, higher wet tundra graminoid values were predicted for area A (low centered polygons), while lower wet tundra graminoid values were predicted for area B (high centered polygons). This attribution of microtopography can also be seen in other upscaling studies around Barrow, AK [45]. For Arctic landscapes where the polygonal landscape are not the primary control, PFTs could depend on other criteria such as the topographic position and it is essential to find specific algorithms and model parameters with proper site-specific PFT measurements.

The Euclidean distance in multi-variate state space provided a metric for representativeness. Gray-scaled representativeness maps showed the similarity of every map cell to the vegetation sampling locations in the BEO. This provided a sampling strategy to identify under-represented areas for further field sampling. Including additional observations from the under-represented areas in the IDW model significantly improved the estimation of PFT distributions across the landscape. This analysis can provide model-inspired insights into optimal sampling strategies across space and through time [67]. The accuracy of the upscaled data were higher for areas well represented by the sampling sites and lower for areas that were under-represented. The difference maps from subtracting the *with phenology* and *without phenology* showed the greatest differences occur

in the poorly represented areas (Figure 2.10). These poorly represented areas are due to differences in the spectral and topographic differences, meaning that different vegetation characteristics could occur in these areas. Also, highly saturated areas could produce under-represented areas and adding moisture content to the upscaling approach could improve PFT estimates. The improved representativeness analysis still shows locations that are under-represented and should be investigated in future field campaigns.

The methods we utilized here have improved our ability to predict the vegetation cover across broad portions of the landscape on the BEO. On-going research to improve the relationships among species-specific tundra vegetation cover, biomass, and the allocation of carbon below-ground to the production of roots and rhizomes [154, 74] may extend the utility of remote-sensing from observable plant and environmental characteristics to unobservable characteristics and processes beneath the soil surface. Other Arctic landscapes could benefit from our research by gathering the measurements mentioned above and applying these methods (i.e., representativeness, clustering, interpolation). However, one might want to test different multivariate statistical methods (i.e., linear regression, neural networks).

The remote sensing imagery was collected in 2010, the training data used was collected in 2012, and the ground-truthing was conducted in 2014. Changes in vegetation composition and cover do occur through time, but they are much slower in the Arctic tundra compared to other parts of the world [161]. However, herbivory outbreaks can occur in the BEO. Villarreal et al. [178] saw low amounts of biomass in 2008 for all communities caused by a lemming population outbreak. We are assuming that dramatic changes in PFT percentages did not occur for 2010, 2012, and 2014, since we had high coefficients of determination from the ground-truthing campaigns. In order to accurately verify this, more high-resolution satellite and aerial imagery would be needed for these years.

Terrestrial vegetation plays an important role in the dynamics of the Earth system through water and energy exchange and is a large source of uncertainty in models (e.g., CLM). Chapin et al. [20] recommended the use of Arctic- and Boreal-specific PFTs in vegetation models, which includes deciduous shrubs, evergreen shrubs, sedges, grasses,

forbs, *Sphagnum* moss, non-*Sphagnum* moss and lichens. Estimates of PFT distribution from our study provides necessary inputs to model vegetation across larger landscapes for high-resolution land surface models (e.g., Arctic Terrestrial Simulator, PFLOTRAN). Efforts are underway to perform model simulations at the BEO and assess the sensitivity of including these Arctic-specific PFT distributions. The presented approach for upscaling *in situ* measurements using high-resolution satellite imagery provides a framework for future studies focusing on Arctic ecosystem change.

2.5 Conclusions

We presented a method for upscaling of field based observation of PFT distributions at a polygonal tundra site using high-resolution spectral remote sensing. Maps of Arctic PFT types in tundra ecosystem at 0.25 m spatial resolution developed in this study is the most detailed and high resolution PFT distribution product as per our knowledge. Results and analysis presented supports our hypothesis that the phenological pattern captured by the remote sensing helps improve the accuracy of upscaling algorithm. Phenology helps discriminate the vegetation types by their blooming and green-up behavior throughout the growing season. Developed method was demonstrated to perform well for upscaling of sparse observations. Landscape characterization helped stratify the heterogeneous landscape and allowed for upscaling of observation to area with similar properties and accurate upscaling model. Representativeness metric employed in the study provided a way to measure dissimilarity in pixels and provides an approach for optimal sampling design to reduce the uncertainties (Figure 2.12). This method takes a different approach than previous studies due to the high spatial and spectral resolution of the WorldView-2 and the covariation of vegetation with topography as captured by LiDAR-derived DEMs. Unlike previous studies we developed and applied a data analytic approach using high spectral and spatial resolution WorldView-2 and LiDAR data sets to upscale the field-based observations of PFT distributions. It offers an approach for upscaling of sparse field observations using increasingly available rich high-resolution remote sensing data sets.

Chapter 3

Convolutional Neural Network Approach for Mapping Arctic Vegetation using Multi-Sensor Remote Sensing Fusion

Langford, Z. L., Kumar, J., and Hoffman, F. M. (2017). Convolutional Neural Network Approach for Mapping Arctic Vegetation using Multi-Sensor Remote Sensing. In *International Conference on Data Mining Workshops (ICDM 2017)*. Institute of Electrical and Electronics Engineers (IEEE).

3.1 Abstract

Accurate and high-resolution maps of vegetation are critical for projects seeking to understand the terrestrial ecosystem processes and land-atmosphere interactions in Arctic ecosystems, such as U.S. Department of Energy's Next Generation Ecosystem Experiment (NGEE) Arctic. However, most existing Arctic vegetation maps are at a coarse resolution and with a varying degree of detail and accuracy. Remote sensing-based approaches for mapping vegetation, while promising, are challenging in high latitude environments due to frequent cloud cover, polar darkness, and limited availability of high-resolution remote sensing datasets (e.g., $\sim$ 5 m). This study proposes a new remote sensing based multi-sensor data fusion approach for developing high-resolution maps of vegetation in the Seward Peninsula, Alaska. We focus detailed analysis and validation study around the Kougarok river, located in the central Seward Peninsula of Alaska.

We seek to evaluate the integration of hyper-spectral, multi-spectral, radar, and terrain datasets using unsupervised and supervised classification techniques over a $\sim$343.72 km^2 area for generating vegetation classifications at a variety of resolutions (5 m and 12.5 m). We fist applied a quantitative goodness-of-fit method, called *Mapcurves*, that shows the degree of spatial concordance between the public coarse resolution maps and k-means clustering values and relabels the k values based on the best overlap. We develop a convolutional neural network (CNN) approach for developing high resolution vegetation maps for our study region in the Arctic. We compare two CNN approaches: (1) breaking up the images into small patches (e.g., 6 x 6) and predict the vegetation class for entire patch and (2) semantic segmentation to predict the vegetation class for every pixel. We also perform accuracy assessments of the developed data products and evaluate varying

CNN architectures. The fusion of hyper-spectral and optical datasets performed the best, with accuracy values increased from 0.64 to 0.96-0.97 when using training labels produced by unsupervised clustering and *Mapcurves* method for both CNN models.

3.2 Introduction

The Arctic has emerged as an important focal point for the study of climate change due to the greatest regional warming on Earth in recent decades, which was twice the rate of the global mean warming [159]. Increased warming in the Arctic will have potential climate feedbacks [107, 122, 148] and consequently influence ecosystems [62, 119]. Current climate models in the Arctic project an ongoing temperature increase for the next decades [122]. Many studies suggest that environmental changes associated with a warmer climate could have considerable consequences for terrestrial ecosystems, such as Arctic plant communities [192]. Continued greening over the next century will produce multiple climate feedbacks. Model experiments in the Arctic demonstrate that the associated feedbacks with vegetation are positive, and failing to account for them in future climate studies may result in inaccurate projections [112].

Model evaluations for future climate studies also show a poleward advance of the forest–tundra boundary, an expansion of tall shrub tundra, and a dominance shift from deciduous to evergreen boreal conifer forest [192, 158]. Therefore, an accurate accounting of Arctic vegetation is important for parameterization of models that reflect accurate feedbacks to climate change. For example, [93] used WorldView-2 and LiDAR datasets to create $\sim$0.25 m spatial resolution plant functional type (PFT) datasets for driving land-surface models in Barrow, AK. Kumar et. al, 2016 [89] utilizing similar remote sensing datasets to characterize the microtopography of polygonal tundra employed the open-source PFLOTRAN (massively parallel subsurface flow and reactive transport) code to simulate variability in subsurface thermal regimes of ice-wedge polygons at the field-scale at Barrow, AK.

High-resolution vegetation datasets are needed for current modeling projects in the Arctic, such as the Next-Generation Ecosystem Experiments (NGEE Arctic). NGEE Arctic is a Department of Energy (DOE) project that seeks to improve confidence in global climate projections through a coordinated series of model-inspired investigations (http://ngee-arctic.ornl.gov/). NGEE Arctic is working to couple 3-Dimensional surface-subsurface hydrology model PFLOTRAN with Accelerated Climate Model for Energy (ACME) Land Model (ALM) for modeling Arctic climate change at a variety of scales. High-resolution spatial datasets are needed to drive these models (e.g., vegetation, topographic, and hydrologic data). It's important to evaluate remote sensing imagery that can provide datasets to drive high-resolution models and guide field sampling campaigns. NGEE Arctic currently is conducting extensive field research at a series of sites across the Seward Peninsula, Alaska. The selection of the Seward Peninsula is based on an analysis indicating that western Alaska is a proxy for the future ecological and climatic regime of the North Slope of Alaska toward the end of the century[67].

Approaches based on hyper-spectral imagery, also named imaging spectroscopy, have shown to be effective for identification a wide range of vegetation types [166], including Arctic vegetation types [15, 29]. However, this has mostly been shown through hand held or airborne hyper-spectral sensors [29]. Multi-spectral datasets (e.g., IKONOS, SPOT, WorldView) are also becoming more available in Arctic and Boreal ecosystems. Synthetic aperture radar (SAR) is also a promising remote sensing dataset for vegetation classifications, enabling imaging in all weather conditions at any time of day or night. These different remote sensing platforms vary in their sensor characteristics, spatial and temporal resolution and have their strengths and weaknesses. While traditionally due to their characteristics these remote sensing data sets have been used independently, while multi-sensor data fusion holds promise to harvest their complementary strengths to characterize vegetation properties. Machine learning algorithms that are based on multiple datasets (i.e., multi/hyper-spectral images) are needed to develop and evaluate high-resolution vegetation maps using data from multiple remote sensing platforms.

The resolution and accuracy of current publicly available vegetation maps are often low and are too inaccurate to be used for field-scale studies. New methods and approaches are needed to increase the accuracies at a higher resolution. Objective of this paper is to 1) explore the predictability of multi-sensor data fusion, 2) develop Covolutional Neural Networks (CNN) for predicting vegetation type on the landscape using two approaches, (2A) by breaking up the images into small patches (e.g., 6 x 6) and predicting the vegetation class for entire patch; and (2B) evaluate localization using semantic segmentation. These approaches help identify the optimal CNN network and multi-sensor data fusion for Arctic vegetation mapping.

3.3 Materials

3.3.1 Study Area

The study area selected for this research is located on the Seward Peninsula on the western coast of Alaska. The analysis was performed near a watershed in the Seward Peninsula (Figure 3.1), due to the data collected for the NGEE Arctic project. The Seward Peninsula experiences a semi-maritime climate that is controlled by the Bering Sea and sea surface conditions (especially sea–ice extent) [72]. The Seward Peninsula lies at the important zone of vegetation transitions from boreal forest to tundra [152], making this part of Alaska an important region for studying vegetation characteristics. Most of the Seward Peninsula is treeless, with some smaller isolated mountain ranges and varied geologic substrates, including limestone, deep unglaciated loess, and lava flows of various ages [131].

The bounding region of the study area was determined by the overlapping raster boundaries from the SPOT-5 and EO-1 Hyperion imagery. The study area is located near the Kougarok River, located in the center of Seward Peninsula, Alaska, and consists of low Arctic tundra dominated by open low mixed shrub-sedge tussock tundra communities [177]. The mean annual temperature for this area is -2.4°C and with the mean annual temperature in July is 11.0°C; and the mean annual precipitation is 102.1 mm [118] . This

region is a zone of nearly continuous permafrost with an active layer that has a mean thickness of 56 cm [64].

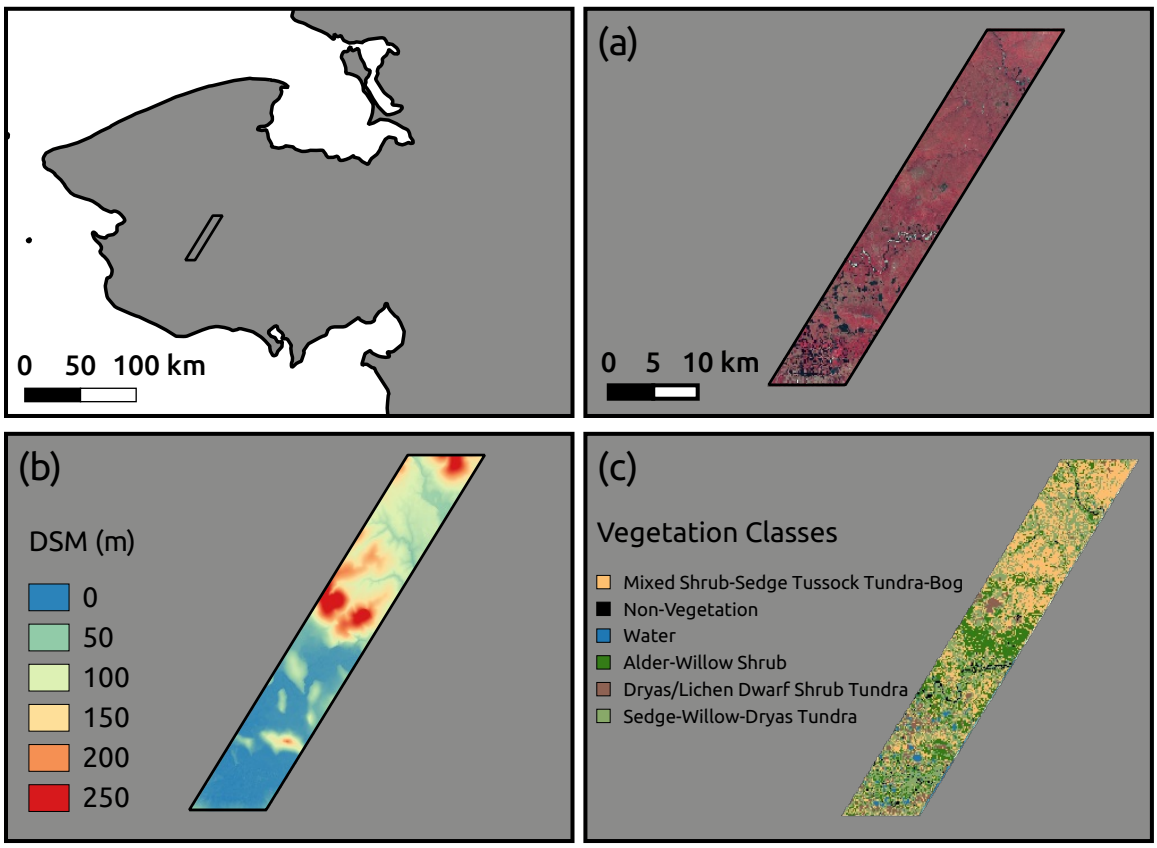


Figure 3.1: Study area based on the EO-1 Hyperion footprint, showing (a) SPOT-5 false color image, (b) digital elevation model, and (c) vegetation classes.

3.3.2 Remote Sensing Datasets

All datasets were processed in Alaska Albers Equal Area Conic (EPSG:3338), NAD83 horizontal datum and NAVD88 vertical datum. Table 3.1 lists the remote sensing products in this study. One ALOS PALSAR L-band SAR image with dual polarization (FBD) of HH (horizontal transmitting, horizontal receiving) and HV (horizontal transmitting, vertical receiving) that was radiometric and terrain corrected was collected, more information can be found at https://www.asf.alaska.edu/sar-data/palsar/. The EO-1 Hyperion and Landsat 8 OLI images were collected from USGS https://earthexplorer.usgs.gov/,

Table 3.1: List of remote sensing datasets used in this study

Dataset	Resolution	Acquisition Date
EO-1 Hyperion	30 m	24 June 2015
Landsat 8 OLI	30 m	17 August 2016
ALOS-1 PALSAR	12.5 m	29 August 2007
IfSAR DSM	5 m	Summer 2012
SPOT-5	2.5 m	Summer 2009 – 2012

with EO-1 Hyperion consisting of 198 calibrated bands (0.4 - 2.5 μm) and Landsat 8 OLI consisting of 11 bands, with 9 bands (0.4 - 2.29 μm) used in this study. The terrain corrected versions for EO-1 Hyperion (L1T) and Landsat 8 OLI (Level-1) were processed. The Digital Surface Model (DSM) IfSAR and SPOT-5 data were collected from the Geographic Information Network of Alaska (http://gina.alaska.edu/). The SPOT-5 satellite images used in this study were gathered by the "Alaska Statewide Digital Mapping Initiative", which produced a new statewide orthomosaic that provides complete multispectral coverage of the state at 2.5 m spatial resolution. The CIR SPOT-5 orthoimage was used over the study area, which consists of the green (0.50 - 0.59 μm), red (0.61 - 0.68 μm), and near infrared (0.78 - 0.89 μm) bands.

3.3.3 Vegetation Data

The 30 m Alaska Existing Vegetation Type (AKEVT) (http://akevt.gina.alaska.edu/) vegetation map for the study region for training and validating the models. Table 3.2 shows the area of the six chosen vegetation classes across the study region.

Table 3.2: Area of the AKEVT vegetation classes for the study region (343.72 km^2).

Class	Area (km^2)	Percentage
Mixed Shrub-Sedge Tussock Tundra-Bog	120.75	35.13%
Alder-Willow Shrub	74.33	21.63%
Dryas/Lichen Dwarf Shrub Tundra	20.52	5.97%
Sedge-Willow-Dryas Tundra	116.41	33.87%
Water	6.13	1.78%
Non-Vegetation	5.58	1.62%

Some vegetation classes were very small and merged into other classes of similar strata. This was also done based on the Alaska vegetation classification system [177]. For example, the willow shrubs covered only 0.38 % of the study region and was merged into the alder-willow shrub class. The AKEVT map was cropped to the study region and condensed the classes down to six vegetation types that exist in study region: mixed shrub-sedge tussock tundra-bog, alder-willow shrub, dryas/lichen dwarf shrub tundra, sedge-willow-dryas tundra, water, and non-vegetation.

3.4 Methodology

Figure 3.2 shows a flowchart of methodology developed in this study and describes the steps in detail in the following subsections.

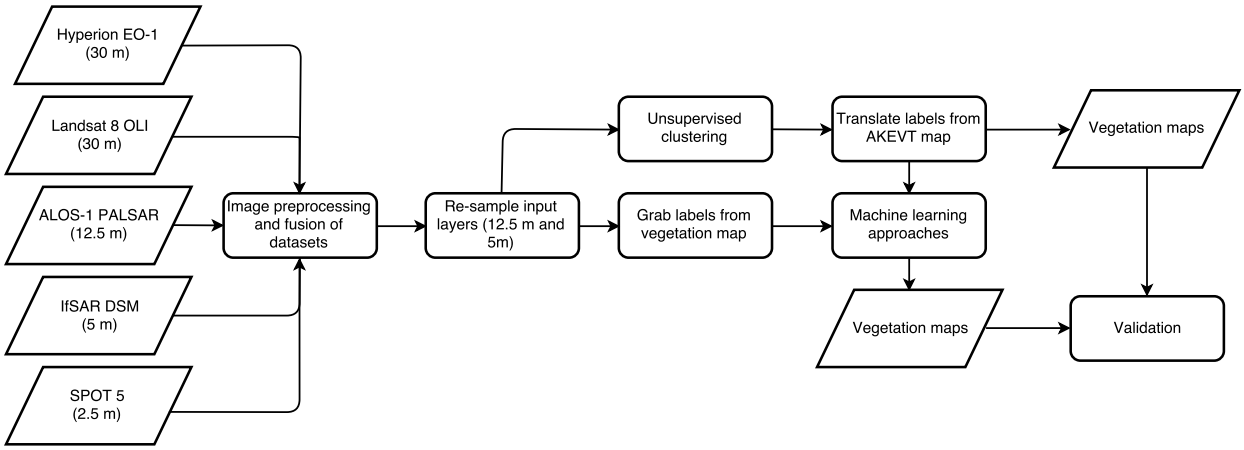


Figure 3.2: Flowchart of the study for fusion of remote sensing datasets and to generate high-resolution vegetation maps.

3.4.1 Data Processing

The terrain corrected versions for EO-1 Hyperion (L1T) and Landsat 8 OLI (Level-1) were processed. The EO-1 Hyperion and Landsat 8 OLI datasets were converted to Top Of Atmosphere (TOA) reflectance according to the USGS documentation. The SPOT-5 satellite images used in this study were gathered by the "Alaska Statewide

Digital Mapping Initiative", which have three statewide mosaics available at 2.5 m spatial resolution: color infrared (CIR), psuedo-natural color, and panchromatic (grayscale). The SPOT-5 orthoimage was radiometrically corrected for tone, balance, and geometry quality control along tile edges for terrain and linear features. The SPOT-5, PALSAR, and IfSAR datasets were normalized to between 0 and 1 for consistency among the TOA datasets. The Lee filtering algorithm (7×7 window) was applied to ALOS-1 PALSAR image to reduce the speckle [98]. All of the remote sensing datasets were re-sampled by pixel aggregation to 5 m and 12.5 m using the nearest-neighbor re-sampling. To explore the predictability of various remote sensing data sets in multi-sensor data fusion approach, fourteen sets of data to conduct case studies, which are describe in Table 3.3. Each specific dataset will be refereed to as as D by number (e.g., D14 refers to merging all the datasets together).

Table 3.3: Multi-sensor vegetation classification cases

Case	Fusion Combinations of Remote Sensing Datasets
D1	EO-1, IfSAR
D2	EO-1, Landsat 8 OLI, IfSAR
D3	EO-1, ALOS-1 PALSAR, IfSAR
D4	EO-1, SPOT-5, IfSAR
D5	EO-1, ALOS-1 PALSAR, SPOT-5, IfSAR
D6	EO-1, ALOS-1 PALSAR, Landsat 8 OLI, IfSAR
D7	EO-1, SPOT-5, Landsat 8 OLI, IfSAR
D8	Landsat 8 OLI, IfSAR
D9	Landsat 8 OLI, ALOS-1 PALSAR, IfSAR
D10	Landsat 8 OLI, SPOT-5, IfSAR
D11	ALOS-1 PALSAR, IfSAR
D12	ALOS-1 PALSAR, SPOT-5, IfSAR
D13	SPOT-5, IfSAR
D14	EO-1, Landsat 8 OLI, ALOS-1 PALSAR, SPOT-5, IfSAR

3.4.2 Training Dataset

High quality training dataset is critical for building robust and accurate CNN models. We employed two different data sets to train the CNN models.

Alaska Existing Vegetation Map

AKEVT is a landcover type map produced at 30m for a portion of Western Alaska Landscape Conservation Cooperative (WALCC) region by US Fish and Wildlife Services. Map was produced using field plot data, LANDSAT 7 ETM+ spectral data and environmental variables. AKEVT is one of the best publicly available vegetation map for the data poor region of the Seward Peninsula of Alaska, however, resolution is coarser than the target resolution of the current study.

Unsupervised Classification-Based Vegetation Map (*UCVM*)

Unsupervised multi-variate clustering techniques have been widely used in Earth science for delineation of ecoregions based on gridded datasets [65, 91]. We applied unsupervised classification on remote sensing data set (Table 3.1) to develop a high resolution map and improve the accuracy of AKEVT map for use as training data set. We then performed a principal component analysis (PCA) analysis of the remote sensing datasets (Table 3.1) and selected the top three components that explain 99% variance. A k-means algorithm was used to cluster the datasets into groups containing similar spectral characteristics [59].

While the unsupervised classification technique identifies groups of similar characteristics, the output classes are defined by their spectral properties and lack translation to an understandable vegetation type. The *Mapcurves* method developed by [55] provides a map algebraic approach to compare two maps. The *Mapcurves* method [55] calculates a goodness-of-fit (GOF) score that indicates the degree of spatial correspondence between polygons in two different maps, for example, the AKEVT map and the remote sensing datasets. GOF is a unitless measure of spatial overlap between map categories:

$$GOF = \sum_{polygons} \frac{C}{B+C} x \frac{C}{A+C}$$

where A is the map that is being compared, B is the reference map, and C is the proportion of the reference category (B) that shares with the tested category (A). The GOF weighs the presence of the intersecting categories, each of which might share a small or large spatial intersection with the category being tested. The GOF score is a unitless metric. For example, a high GOF score would represent high spatial overlap with the clusters (k) from the unsupervised clustering classifications and the AKEVT map.

Mapcurves was used to identify the best "translation table" between dataset clusters and vegetation types defined by the AKEVT map. The clusters with the highest GOF score and relabel the map accordingly. The *Mapcurves* reclassifies the remote sensing based unsupervised classification maps (*UCVM*) into AKEVT vegetation classes.

When used for training, the key purpose for using unsupervised clustering and *Mapcurves* method was to evaluate if updating the AKEVT vegetation classes using this simple method could increase the accuracies of the CNN models. We finally evaluate the accuracy scores based on the *UCVM* map and the AKEVT map to determine which dataset is appropriate to train the CNN models.

3.4.3 Convolutional Neural Network

Deep learning neural networks, which learn the representative and discriminative features in a hierarchical manner from the data, are becoming more efficient at image classification in the remote sensing community [190]. Convolutional Neural Networks (CNN) has shown excellent performance in many computer vision and machine learning problems [163]. CNN take advantage of the fact that the input consists of images and they constrain the architecture in a more sensible way. In particular, unlike a regular Neural Network, the layers of a CNN have neurons arranged in 3 dimensions: width, height, depth (i.e., number of channels). CNN has one or more convolutional layers, often followed by one or more fully connected layers [189]. Conventionally, a full CNN

architecture consists of Convolutional Layer, Pooling Layer, and Fully-Connected Layer [189]. CNNs have become a popular algorithm in the satellite remote sensing community [190]. Chen et al., 2014 [23] applied autoencoders to learn representations (i.e. features) of hyper-spectral image data in an unsupervised manner. Wu et al., 2017 [184] used a convolutional recurrent neural network (CRNN) to learn more discriminative features for hyper-spectral data classification. Zhang et al., 2017 [191] built a deep CNN with limited satellite image samples, using a transfer learning approach by sharing the common image features of the natural images. However, most of these approaches are built upon coarse and small datasets, such as Indian Pines and Kennedy Space Center. Additionally, these methods are solely built upon a particular dataset and don't seek multi-sensor fusion.

Supervised CNN models were used throughout the paper, which maps the input image (x_i) over a series of layers to a probability vector ($\hat{y}_i$) over the different classes. The typical use of CNN is on classification tasks, where the output to an image is a single class label, such as the ImageNet competition [88]. However it is important to evaluate pixel-wise labeling using CNNs. Two CNN approaches were implemented using the TensorFlow [1] and Keras framework [24] in Python: 1) first approach uses patches of images as inputs into a CNN architecture, where the entire patch is predicted as a single vegetation class; and 2) the use of semantic segmentation, where a class label is assigned to each pixel. We refer to the first and second approach as the patch-level and pixel-level approach, respectively.

Both CNNs training processes start with the weights of all networks randomly initialized, and the initial learning rate is set to 10^{-4}. A batch size of 150 was used in all experiments, which defines the number of samples that is going to be propagated through the network. The `sparse_categorical_accuracy` metric was used in Keras using 10% of the data for validation while rest for training. `sparse_categorical_accuracy` metric calculates the mean accuracy rate across all predictions for the multi-class classification problem. Categorical accuracy metric was selected in Keras because of the sparse and categorical nature of the objective function. The accuracy score was computed by taking the number of correctly predicted samples and dividing by the total number of samples.

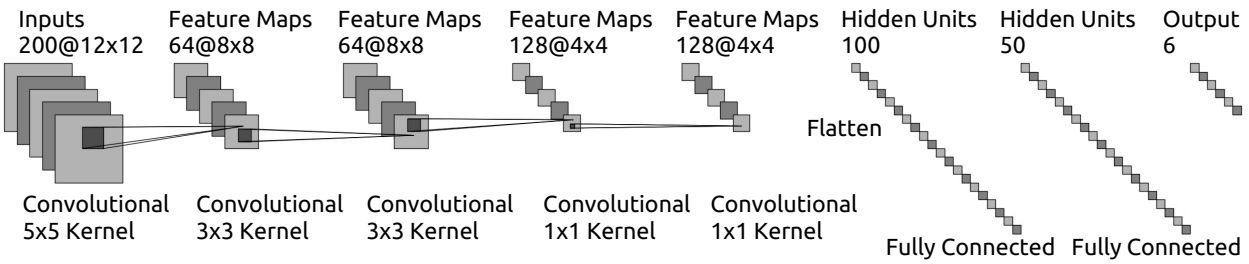


Figure 3.3: Example architecture of a seven layer patch-based CNN model. A 12 by 12 crop of an image (with 200 bands) is presented as the input. This is convolved with 64 different 1^{st} layer filters, with a kernel size of 5×5, using pooling with stride 2. Similar operations are repeated in the following layers. The last two layers are fully connected, taking features from the top convolutional layer as inputs. The final layer is a softmax function, corresponding to the number of classes.

Patch-Level CNN Architecture

Three different patch sizes of 3×3, 6×6, and 12×12, where each patch contains 9, 36, and 144 pixels, respectively, were evaluated. Each layer of the CNN consists of the convolution of the previous layer output with a set of learned filters, the passing the responses through a rectified linear function ($relu(x)$ = max(x,0)), pooling over local neighborhoods, and local contrast operation that normalizes the responses across feature maps [88, 189]. The top few layers of the network are conventional fully-connected networks and the final layer is a softmax classifier [189]. Figure 3.3 shows the first CNN architecture used in this study.

Pixel-Level CNN Architecture

Semantic segmentation for images can be defined as the process of partitioning and classifying the image into meaningful parts, and classify each part at the pixel level into one of the pre-defined classes. Previous studies on segmentation break up the images into patches in order to increase the number of training images [139]. Larger patches require more max-pooling layers that reduce the localization accuracy, while small patches allow the network to see only little context [139]. More recent approaches [58] proposed a classifier output that takes into account the features from multiple layers.

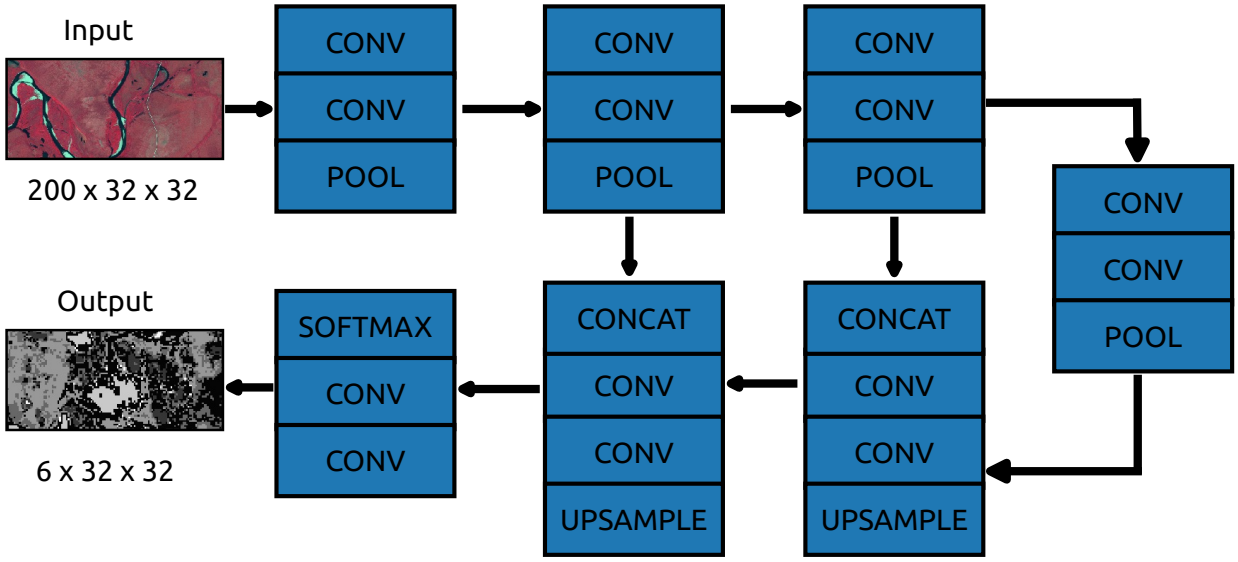


Figure 3.4: An example of the u-net pixel-based architecture from taking a 32×32 pixel patch with 200 bands. The architecture has a series of convolutional and max pooling layers when downsampling. Upsampling and feature concatenating, which means this process uses information from the previous layers, was performed. There is a constant number of 64 filters throughout the network. The final output feature maps are fed to a softmax classifier for pixel-wise classification.

The semantic segmentation CNN model was inspired by the family of u-net architectures, where low-level feature maps are combined with higher-level ones, which enables precise localization [139]. This type of network architecture was especially designed to effectively solve image segmentation problems. This architecture allowed for more detail in the segmentation by using shortcut connections from each layer [139]. The contracting path consists of the repeated application of two 3×3 convolutions, each followed by a Rectified Linear Unit (ReLU) and a 2×2 max pooling operation with stride 2 for downsampling [139]. Every step in the expansive path consists of an upsampling of the feature map followed by a 2×2 convolution (up-convolution), a concatenation with the correspondingly feature map from the contracting path, and two 3×3 convolutions, each followed by a ReLU [139]. The number of feature channels during the downsampling and upsampling stayed the same at 64. At the final layer a 1×1 convolution is used to map each 64-component feature vector to the vegetation classes using the softmax function. Figure 3.4 shows the network architecture for the pixel-level CNN approach.

3.5 Results and Discussion

Unsupervised Classification based Vegetation Map (*UCVM*)

Unsupervised k-means clustering algorithm was used to identify patterns of vegetation using remote sensing data set. Top three dominant principal components from remote sensing data set (Table 3.1) were classified at varying levels of division (k = 10, 25, 50). While classifying data among fewer number of clusters (k) tends to lump vegetation classes together, using larger number of cluster may define clusters with small differences in remote sensing signatures across vegetation types. For that reason, we conducted our unsupervised classification at varying levels of division from small to large. *Mapcurves* however is capable of identifying small difference between categories and eliminating them by reclassifying the similar categories as one.

We applied *Mapcurves* to add labels to the unsupervised classifications, identify unique vegetation classes while collapsing similar ones. While the *Mapcurves* classification method was able to identify unique vegetation types, it also identified where outliers or noisy data could exist within the AKEVT map. Figure 3.5 shows an example of using the *Mapcurves* method to generate vegetation map using unsupervised k-means clustering. Figure 3.5(c) shows the re-labeled vegetation map (UCVM) generated from k=25 clustering map (Figure 3.5(a))using data set D14 (EO-1, Landsat 8 OLI, ALOS-1 PALSAR, SPOT-5, IfSAR), showing large differences from the original AKEVT map (i.e., accuracy of 0.51) (Figure 3.5(b)). Table 3.4 shows the accuracy of unsupervised clustering based vegetation map using *Mapcurves*.resolution datasets.

We performed the analysis at both 5 m and 12.5 m resolutions. Increasing the spatial resolution from 5 m to 12.5 m did not increase the accuracy substantially. This could be due to the fact that the AKEVT map was only available at 30 m resolution. Cases using the hyper-spectral datasets displayed the best accuracies (D1–D7 and D14), with unsupervised classification at k = 25 and k = 50 levels of division performing the best. After assessing the accuracy scores, we used the D4 and D14 for 5 m and 12.5 m datasets, respectively. These datasets were used in addition to AKEVT maps to train our CNN models.

Table 3.4: Accuracy values for the vegetation maps (UCVM) produced by the *Mapcurves* method using unsupervised classification at different levels (k) at 5 m and 12.5 m resolution, with cases with best scores indicated by bold font.

	k=10		k=25		k=50	
Case	5 m	12.5 m	5 m	12.5 m	5 m	12.5 m
D1	0.47	0.46	0.50	0.51	0.54	0.53
D2	0.47	0.46	0.50	0.51	0.54	0.54
D3	0.47	0.46	0.50	0.51	0.54	0.53
D4	0.47	0.46	0.52	0.52	**0.55**	0.54
D5	0.46	0.46	0.50	0.51	0.54	0.54
D6	0.47	0.45	0.49	0.52	0.53	0.54
D7	0.47	0.46	0.51	0.51	0.54	0.54
D8	0.44	0.45	0.47	0.47	0.48	0.48
D9	0.44	0.44	0.46	0.46	0.47	0.46
D10	0.45	0.45	0.47	0.47	0.48	0.50
D11	0.44	0.44	0.44	0.44	0.45	0.45
D12	0.45	0.44	0.48	0.46	0.50	0.47
D13	0.44	0.44	0.48	0.48	0.49	0.50
D14	0.47	0.46	0.50	0.51	0.54	**0.55**

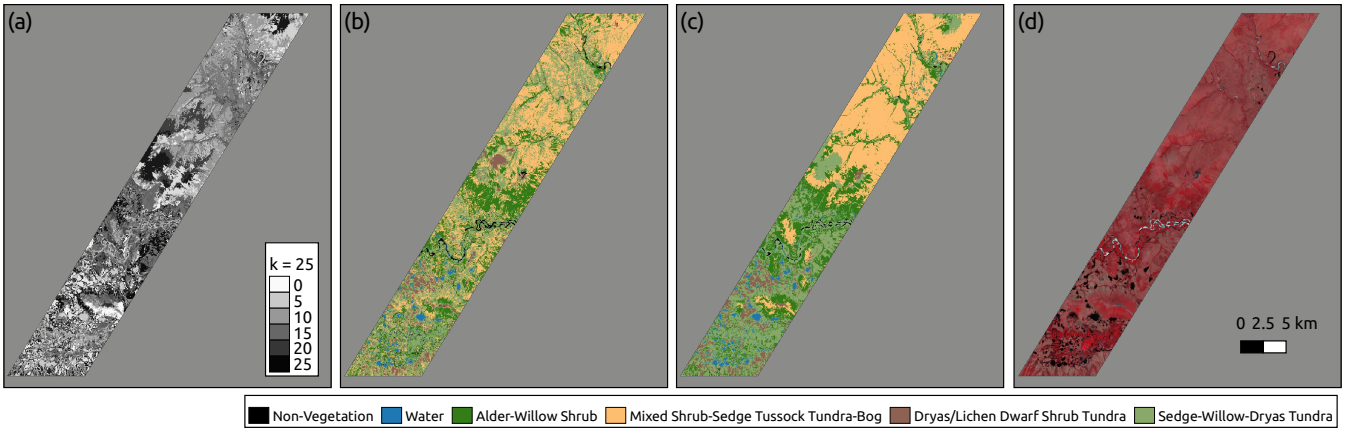


Figure 3.5: (a) Unsupervised classification map (k=25) from using D14 (EO-1, Landsat 8 OLI, ALOS-1 PALSAR, SPOT-5, IfSAR); (b) The original AKEVT vegetation maps; (c) UCVM vegetation map generated using *Mapcurves* method; (d) and EO-1 Hyperion false color image.

3.5.1 Patch-Level CNN Approach

We developed patch-level CNN models for patch sizes of 6×6, 12×12, and 16×16. Models were trained using AKEVT and UCVM data sets. Table 3.5 shows the accuracy values for our patch-level CNN models corresponding to the image patch (width and height), resolution, and training data set used (i.e., AKEVT and UCVM). The CNN models trained using AKEVT had accuracies ranging from 52% to 68%. The hyper-spectral datasets performed the best with the AKEVT labels, ranging from 59% to 68% accurate, with patch size of 6×6 and 12×12 achieving the highest scores. Increasing the accuracy from 12.5 m to 5 m seems to increase the accuracy for certain datasets and patch size. For example, for D14 we saw an increase of 10% when increasing the spatial resolution to 5 m. D11 (ALOS-1 PALSAR, IfSAR) performed poorly the when using AKEVT for training, with accuracy values around 52%. This could be due to SAR datasets generally have high variations due to speckle or to different types of scattering mechanisms [35]. However, several multi-sensor sets that included SAR didn't see drop in performance. For example, D12 (ALOS-1 PALSAR, SPOT-5, IfSAR) and D13 (SPOT-5, IfSAR) performed the same using the AKEVT or UCVM data sets for training.

The UCVM vegetation map increased the accuracy for all datasets by a large margin (Table 3.5) when used for training. The highest scores were achieved for the hyper-spectral datasets, having 96% accuracy for D3 (EO-1, ALOS-1 PALSAR, IfSAR) for the 12.5 m dataset. The highest score from the 5 m datasets was achieved using D14 dataset with a 96% accuracy. The Landsat 8, SPOT-5, and SAR datasets (D8, D9, D10, D11, D12, and D13) perform better when trained using the AKEVT map with an accuracy range of 66% to 83%, however this is 10% lower than models developed using the hyper-spectral datasets.

Figure 3.6 shows the accuracy scores for D14 at 5 m resolution when increasing the epoch to 100 when using AKEVT and UCVM vegetation maps for training. When trained using AKEVT, each case showed overfitting after certain epochs. Figure 3.6(a) shows the model overfitting after epoch 45, indicating that the training dataset was getting substantially higher accuracies than the test dataset. However, when trained using UCVM (Figure 3.6(b)) the accuracy of the test dataset (i.e., 10% of the data) was always higher than

Table 3.5: Accuracy of the patch-level CNNs using varying patch sizes (i.e., 6×6, 12×12, and 16×16) at 5 m and 12.5 m resolution using AKEVT and UCVM maps for training.

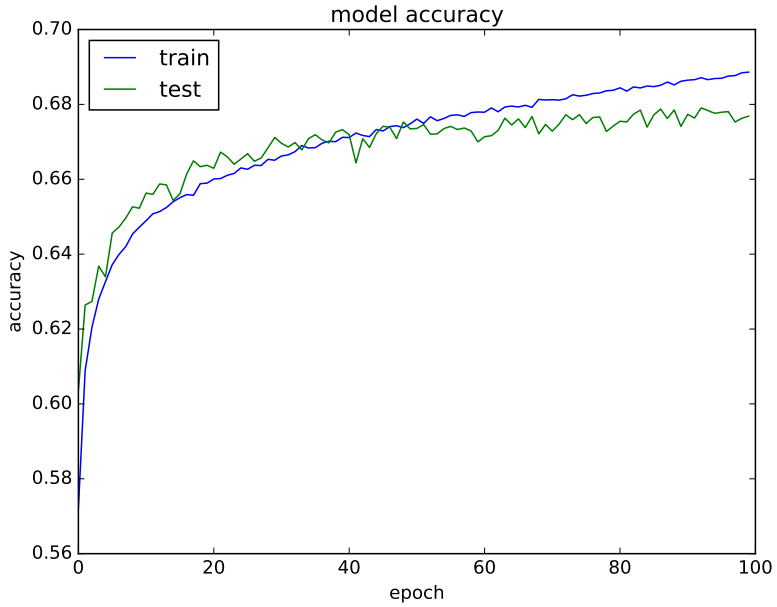
		AKEVT			UCVM		
		6×6	12×12	16×16	6×6	12×12	16×16
D1	5 m	0.64	0.65	0.63	0.94	0.93	0.91
	12.5 m	0.63	0.63	0.59	0.95	0.93	0.87
D2	5 m	0.66	0.66	0.66	0.94	0.92	0.91
	12.5 m	0.65	0.64	0.59	0.95	0.92	0.85
D3	5 m	0.64	0.64	0.64	0.94	0.93	0.90
	12.5 m	0.64	0.62	0.61	**0.96**	0.92	0.88
D4	5 m	0.66	0.67	0.66	0.95	0.93	0.91
	12.5 m	0.66	0.64	0.61	0.95	0.92	0.87
D5	5 m	0.67	0.67	0.66	0.95	0.93	0.91
	12.5 m	0.67	0.64	0.63	0.95	0.92	0.88
D6	5 m	0.66	0.67	0.66	0.94	0.92	0.90
	12.5 m	0.66	0.64	0.61	0.95	0.92	0.87
D7	5 m	0.67	0.68	0.67	0.95	0.93	0.91
	12.5 m	0.67	0.66	0.59	0.95	0.93	0.86
D8	5 m	0.63	0.64	0.65	0.78	0.77	0.78
	12.5 m	0.64	0.62	0.59	0.82	0.80	0.80
D9	5 m	0.63	0.64	0.63	0.78	0.77	0.77
	12.5 m	0.65	0.63	0.59	0.83	0.82	0.80
D10	5 m	0.66	0.67	0.67	0.80	0.79	0.78
	12.5 m	0.67	0.67	0.62	0.83	0.81	0.81
D11	5 m	0.52	0.53	0.53	0.67	0.66	0.67
	12.5 m	0.53	0.52	0.52	0.72	0.74	0.73
D12	5 m	0.62	0.63	0.63	0.76	0.76	0.76
	12.5 m	0.64	0.64	0.56	0.81	0.80	0.78
D13	5 m	0.62	0.63	0.64	0.76	0.75	0.76
	12.5 m	0.64	0.64	0.56	0.81	0.80	0.78
D14	5 m	0.67	0.68	0.67	**0.96**	0.93	0.91
	12.5 m	0.67	0.65	0.57	0.95	0.93	0.86

the training dataset, meaning that model overfitting was not happening and the CNN architecture was performing well.

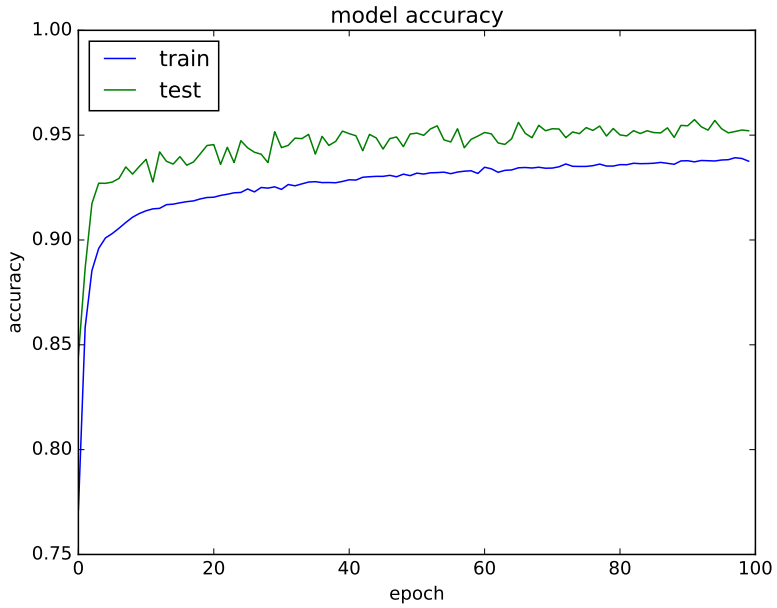
Patch size 6×6 performed the best for the UCVM training data set, however the drop in performance was lower when increasing the resolution to 5 m. We believe that small patch sizes work better since a 6×6 patch may contain many vegetation classes, but the number of samples used in the model training is higher. However, in the patch-level CNN approach, each image patch is input to the model independently, which means that only the "intra-patch" context information is considered [44]. The correlations between patches are not taken into account, which might lead to gaps between patches [44]. However, this may only apply to objects with strong continuity, such as urban features, which is not present in our imagery. Additionally, other patch-level CNN architectures may perform better with large patch sizes (i.e., 32×32) [8].

3.5.2 Pixel-Level CNN Approach

Table 3.6 shows the accuracy values for our pixel-level CNN models corresponding to the image patch width and height, resolution, and training vegetation map used (i.e., AKEVT and UCVM) . The CNN models developed using the AKEVT labels had accuracies ranging from 54% to 68%. D11 (ALOS-1 PALSAR, IfSAR) performed the worst with the AKEVT labels, similar to the patch-level CNN architecture. D7 (EO-1, SPOT-5, Landsat 8 OLI, IfSAR), D10 (Landsat 8 OLI, SPOT-5, IfSAR), and D14 (EO-1, Landsat 8 OLI, ALOS-1 PALSAR, SPOT-5, IfSAR) performed the best with the AKEVT at 5 m and 16×16 patch size. Increasing the resolution and having a patch size of 16×16 worked best for our segmentation architecture. The smaller patch size worked best, due to the increase number of samples used for training the network. However, larger patch sizes may work best for features with strong continuity [44].



(a) The model accuracy for D14 by varying the epoch to 100 using the AKEVT for training and patch size of 6×6.



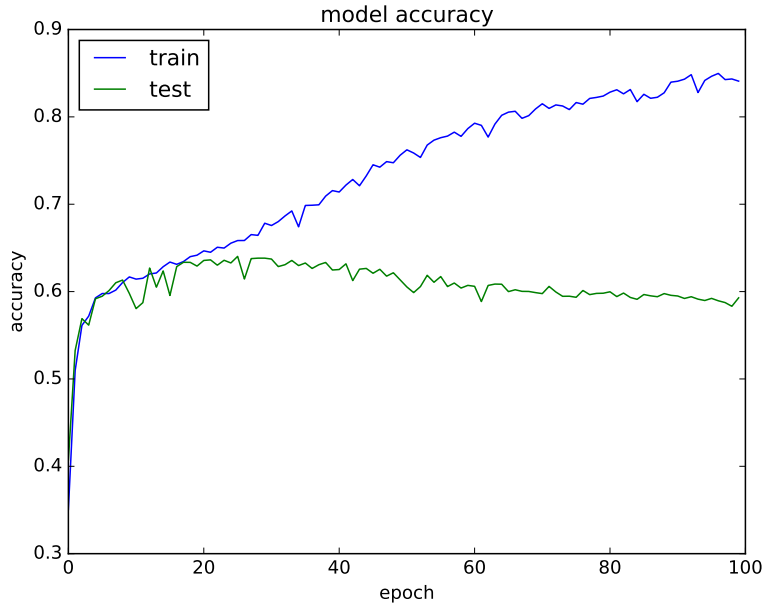
(b) The model accuracy for D14 using the UCVM for training and varying the epoch to 100 for patch size of 6×6.

Figure 3.6: CNN Model accuracies for D14. The green line represents the validation set (10% of data) and the blue line represents the training dataset (90% of data).

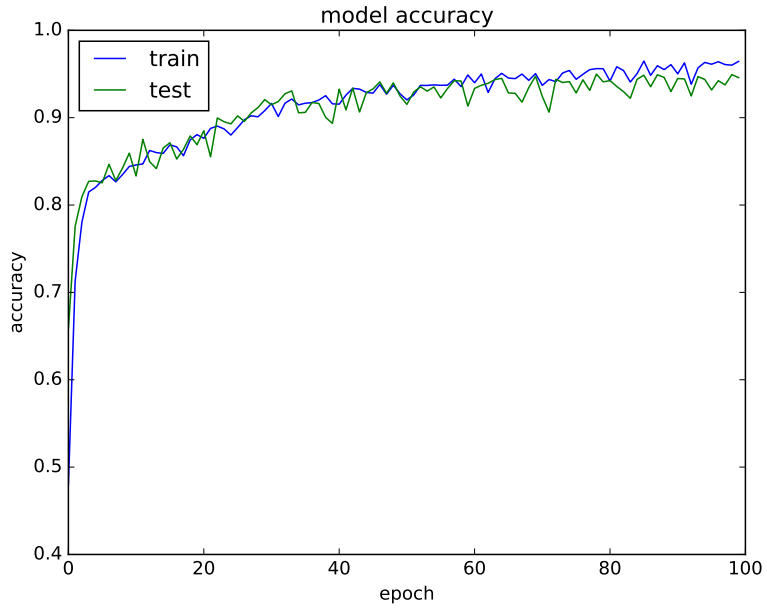
Table 3.6: Accuracy values for the AKEVT and Mapcurves vegetation maps produced by U-Net varying by patch size (i.e., 16, 32, 64) at 5 m and 12.5 m resolution.

		AKEVT			Mapcurves		
		16	32	64	16	32	64
D1	5 m	0.64	0.62	0.61	0.95	0.92	0.89
	12.5 m	0.61	0.59	0.61	0.94	0.90	0.86
D2	5 m	0.66	0.64	0.61	0.94	0.92	0.91
	12.5 m	0.62	0.60	0.61	0.94	0.92	0.87
D3	5 m	0.64	0.63	0.62	0.94	0.93	0.89
	12.5 m	0.62	0.60	0.60	0.94	0.90	0.86
D4	5 m	0.67	0.65	0.63	**0.97**	0.93	0.89
	12.5 m	0.64	0.60	0.62	0.94	0.89	0.86
D5	5 m	0.67	0.65	0.62	**0.97**	0.94	0.89
	12.5 m	0.64	0.62	0.62	**0.95**	0.90	0.86
D6	5 m	0.66	0.65	0.63	0.94	0.92	0.90
	12.5 m	0.64	0.60	0.63	0.94	0.91	0.87
D7	5 m	0.68	0.65	0.62	0.95	0.93	0.91
	12.5 m	0.64	0.62	0.62	0.94	0.91	0.86
D8	5 m	0.64	0.62	0.61	0.76	0.74	0.74
	12.5 m	0.61	0.60	0.56	0.80	0.79	0.80
D9	5 m	0.65	0.65	0.65	0.76	0.75	0.75
	12.5 m	0.65	0.62	0.63	0.82	0.79	0.80
D10	5 m	0.68	0.66	0.66	0.78	0.76	0.76
	12.5 m	0.65	0.64	0.65	0.83	0.80	0.82
D11	5 m	0.55	0.55	0.56	0.67	0.66	0.68
	12.5 m	0.55	0.54	0.55	0.74	0.71	0.74
D12	5 m	0.66	0.65	0.63	0.76	0.75	0.74
	12.5 m	0.64	0.63	0.63	0.81	0.79	0.81
D13	5 m	0.65	0.65	0.64	0.76	0.73	0.75
	12.5 m	0.65	0.62	0.63	0.81	0.78	0.81
D14	5 m	0.68	0.66	0.64	0.96	0.93	0.91
	12.5 m	0.64	0.62	0.63	0.94	0.90	0.87

The UCVM vegetation map increased the accuracy for all datasets by a large margin (Table 3.6), similar to the patch-level CNN model. The highest scores were achieved from the hyper-spectral datasets, having 97% accuracy for D4 (EO-1, SPOT-5, IfSAR) and D5 (EO-1, ALOS-1 PALSAR, SPOT-5, IfSAR) for the 5 m dataset. The highest score from the 12.5 m datasets were the hyper-spectral datasets (D1 – D7 and D14) with a 94%-95% accuracy. The SAR dataset (D11) performed the worst with 66%-67% accuracy. The



(a) The model accuracy for D5 by varying the epoch to 100 using the AKEVT for training and patch size of 16×16.



(b) The model accuracy for D5 using the UCVM method for training and varying the epoch to 100 for patch size of 16×16.

Figure 3.7: Model accuracies for D5. The green line represents the validation set (10% of data) and the blue line represents the training dataset (90% of data).

Landsat, SAR, and SPOT datasets (D8, D9, D10, D12, and D13) had accuracies from 0.77% to 0.83%.

3.5.3 CNN Architectures

Increasing the accuracy from 12.5 m to 5 m didn't have a significant impact on the accuracies. This is probably due to the nearest-neighbor re-sampling method used in this study. Sophisticated re-sampling methods could be performed for a more rigorous analysis. For example, deep learning methods can perform image super-resolution [34]. Additionally, other image enhancement methods could be performed that is specific to hyper-spectral imagery [46].

The pixel-level segmentation architecture consists of a contracting path and a symmetric expanding path that capture context and localization. This architecture performs well with very little training data available, by applying elastic deformations to the available training images [139]. This allows the network to learn invariance to such deformations, without the need to see these transformations in the annotated image corpus [139]. However, other segmentation algorithms could be looked into for comparisons. For example, a segmentation framework specifically tailored to remote sensing images could be applied [124]. Looking into other activation functions, such as the exponential linear units (ELUs), could provide performance increase [124]. Additionally, looking more closely into the hyperparameters, (e.g., learning rate, loss function, weight initialization) could help optimize our CNN approaches.

Smaller patch sizes helped for both CNN models, most likely due to the structure and shape of the vegetation classes. We believe that the number of training examples didn't significantly impact our model accuracies, since we didn't see a high performance gain when increasing the resolution to 5 m. Better image enhancement methods may be necessary (e.g., super-resolution) in order to verify that small patch sizes work better for satellite remote sensing, especially in the case of Arctic vegetation mapping. Patch aggregation approaches could also be looked into that better utilize the interactions of

patch features, such as constructing multiple, shared columns in the neural network and feeding multiple patches to each of the columns [106].

3.6 Conclusion

We implemented an CNN approach to develop Arctic vegetation map using remote sensing data sets for a range of sensors and platforms. We evaluated two CNN architectures, in one approach we break up the images into small patches (e.g., 6×6) and estimate the vegetation class for entire patch and the other approach uses semantic segmentation and pixel-wise labeling. Both model approaches had similar accuracy metrics for all cases. Unsupervised clustering and the *Mapcurves* method based vegetation map (UCVM) helped improve the accuracy scores compared to using the AKEVT map alone. We believe the unsupervised clustering and the *Mapcurves* method help initially reduce the noise associated with the AKEVT map, since all the *Mapcurves* scores were generally low (45-50%).

We explored and demonstrated the potential of multi-sensor remote sensing fusion for mapping vegetation in data sparse region of Arctic. Among data sets considered in the study, hyper-spectral remote sensing datasets provided highest data content to our CNN models, indicating that the spectral signatures of vegetation with high bandwidths are important for predictability of vegetation. SAR datasets performed the worst, however further evaluation of SAR datasets is needed. The Landsat and SPOT-5 datasets demonstrated improved predictability when using the UCVM for training and were important data set for our analysis. We believe the CNN architectures performed in this study provides an accurate method for Arctic vegetation mapping. However, we identified several different approaches that could improve our vegetation maps. Methods developed in this study helps enhance and reduce noise in publicly available vegetation maps, utilizing high-resolution datasets and open-source toolkits (e.g., Keras and Tensorflow). Approaches like these are needed for to provide accurate and high-resolution datasets needed for current modeling projects in the Arctic.

Chapter 4

Integrating Optical and SAR Datasets for Field-Scale Arctic Vegetation Mapping in the Seward Peninsula, Alaska

Langford, Z. L., Kumar, J., Hoffman, F. M., Breen, A., and Iversen, C. M. (2017). Integrating Optical and SAR Datasets for Field-Scale Arctic Vegetation Mapping in the Seward Peninsula, Alaska. *Remote Sensing*, submitted.

4.1 Abstract

Land cover datasets are essential for modeling Arctic ecosystem structure and function and for understanding land–atmosphere interactions at high spatial resolutions. However, most Arctic land cover products are generated at a coarse resolution, and finding quality satellite remote sensing datasets to produce such maps is difficult due to cloud cover, polar darkness, and poor availability of high-resolution imagery. Publicly available datasets at various spatial resolutions over the Arctic must be evaluated to develop accurate high-resolution land cover maps. In this study, we demonstrated a multi-sensor remote sensing-based deep learning approach for developing high-resolution (5 m) vegetation maps for the western Alaskan Arctic on the Seward Peninsula, Alaska. We focused our detailed analysis around a watershed near the Kougarok River contained within this Seward Peninsula imagery. We evaluated the integration of hyper-spectral, multi-spectral, synthetic aperture radar (SAR), and terrain datasets using unsupervised and supervised classification techniques over a $\sim$343 km^2 area and generated high-resolution (5 m) vegetation classification maps. We used the Alaska Existing Vegetation Type (AKEVT) map to train our models. Our study focused on six dominant vegetation or land cover types present within the study region: (1) Alder-Willow Shrubs, (2) Dryas/Lichen Dwarf Shrub Tundra, (3) Sedge-Willow-Dryas Tundra, (4) Mixed Shrub-Sedge Tussock Tundra-Bog, (5) Non-Vegetated, and (6) Water. We developed an unsupervised technique to classify high-dimensional remote sensing datasets into cohesive clusters and employed a quantitative Mapcurves technique to add supervision to the unlabeled clusters, producing a fully labeled vegetation map. We also developed supervised machine learning approaches (i.e., convolutional neural networks (CNNs)) using remote sensing datasets to map vegetation distributions. Fourteen different combinations of remote sensing imagery were analyzed

to explore the optimization of multi-sensor remote sensing fusion. To validate the resulting maps, we collected vegetation observations at 30 plots in the field during the summer of 2016 and evaluated our vegetation products against them for accuracy. Our analysis showed that the CNN models based on EO-1 Hyperion, integrated with the other remote sensing data, provided the most accurate mapping of vegetation types. This study demonstrated the potential of multi-sensor remote sensing data fusion and machine learning techniques for developing high-resolution vegetation maps in Arctic ecosystems.

4.2 Introduction

The Arctic has emerged as an important focal point for the study of climate change due to the greatest regional warming on Earth in recent decades, which was twice the rate of global mean warming [160]. Predicted increases in warming in the Arctic will have potential climate feedbacks [107, 122, 148, 109] and consequently influence ecosystems [62, 119]. Current climate models in the Arctic project an ongoing temperature increase for the next decades [122]. Many studies suggest that environmental variations associated with a warmer climate could have considerable consequences for terrestrial ecosystems, such as Arctic plant communities [192]. Continued greening over the next century will produce multiple climate feedbacks. Arctic vegetation changes will have potential implications for carbon cycling [168], rates of evapotranspiration [127], permafrost dynamics [97, 109], and fire regimes [143, 60]. Model experiments in the Arctic demonstrate that the associated feedbacks with vegetation are positive (i.e., amplification of warming), and failing to account for them in future climate studies will likely result in inaccurate projections [112].

Future climate studies show a poleward advance of the forest–tundra boundary, an expansion of tall shrub tundra, and a dominance shift from deciduous to evergreen boreal conifer forests [192, 158]. Therefore, an accurate accounting of Arctic vegetation is important for parameterization of models that incorporate feedbacks to climate change. Accurate baseline maps of Arctic plant communities would facilitate the understanding and monitoring of land surface changes [51]. In particular, methods are needed that can

accurately quantify Arctic plant communities at fine spatial scales (<30 m) to allow for running high-resolution land surface models. For example, Langford et al. 2016 [93] used WorldView-2 and LiDAR datasets to create ~0.25 m spatial resolution plant functional type (PFT) datasets for driving land-surface models in Barrow, AK. Kumar et al. [89] utilized similar remote sensing datasets for paramterizing the open-source PFLOTRAN (massively parallel subsurface flow and reactive transport) code to simulate variability in subsurface thermal regimes of ice-wedge polygons at the field-scale (spatial size of $\sim 1 \times 1$ m) in Barrow, AK.

High-resolution vegetation datasets are needed for current modeling projects in the Arctic, such as the Next-Generation Ecosystem Experiments (NGEE Arctic) (http://ngee-arctic.ornl.gov/). NGEE Arctic plans to couple PFLOTRAN with the Community Land Model (CLM) [165, 10] for modeling Arctic climate change at a variety of scales. High-resolution spatial datasets are needed to drive these models (e.g., vegetation, topographic, and hydrologic data). It is important to evaluate remote sensing imagery that can provide datasets to drive high-resolution models and guide field sampling campaigns.

Environmental monitoring in Arctic and Boreal ecosystems is primarily conducted at local scales, employing aerial photography and field level sampling [84, 43]. Satellite remote sensing is a complementary tool for monitoring natural and anthropogenic changes in these environments; however, cloud cover, polar darkness, and a sparse number of high-resolution datasets are limiting factors [104]. Synthetic aperture radar (SAR) is a promising remote sensing technology for land cover classifications, enabling imaging in all weather conditions at any time of day or night. Most studies have used SAR for monitoring of forests and wetlands [6, 25, 26], due to its sensitivity to vegetation structure and moisture content [140]. However, SAR data are rarely used for other Arctic land cover types (shrubs, herbaceous, etc.). The Advanced Land Observing Satellite-1 (ALOS-1) Phased Arrayed L-band Synthetic Aperture Radar (PALSAR) is an active microwave sensor using L-band frequency to achieve cloud-free and day-and-night land observation. There are currently around ~3000 freely available ALOS-1 PALSAR images for the Seward

Peninsula, Alaska (https://vertex.daac.asf.alaska.edu/), making this an extensive resource for vegetation mapping.

High-resolution (∼0.3 m – 10 m) multi-spectral datasets (e.g., IKONOS, QuickBird, SPOT, and WorldView) are becoming more available in Arctic and Boreal ecosystems. One project for producing free high-resolution images in Alaska is the "Statewide Ortho Imagery", which provides 2.5 m multi-spectral SPOT-5 images for most of the state (http://gis.dnr.alaska.gov/). The project also provides some SPOT 6 & 7 1.5 m multi-spectral imagery; however, none was available for our study region. Analysis based on hyper-spectral imagery, also named imaging spectroscopy, has shown to be effective for identification of a wide range of vegetation types [166], including Arctic vegetation types [15, 29]. However, this has mostly been shown through hand-held or airborne hyper-spectral sensors [29]. EO-1 Hyperion was a hyper-spectral satellite that operated across the full solar-reflective spectrum with nominal spectral coverage from 0.4–2.5 μm at 30 m spatial resolution [40]. EO-1 Hyperion has proven effective for mineral mapping [99, 110], detecting canopy structure [30], estimating carbon fluxes [188], and processes that are widely applied in many aspects of ecology.

Evaluating satellite hyper-spectral sensors for Arctic vegetation mapping will be beneficial when future data become available (e.g., HyspIRI). The integration of SAR and optical data has the potential to improve land cover classifications [5, 26, 27]. Given the differences between SAR and optical data, it is imperative to find quantitative ways to integrate and compare datasets. Additionally, it may be useful to find optimal machine learning algorithms (i.e., supervised and unsupervised classifications) that can make use of multi-sensor fusion datasets.

Unsupervised classification approaches are efficient for segmentation of multi-variate datasets; however, they are unlabeled and thus are often hard to analyze and validate. The Mapcurves method [55] calculates a goodness-of-fit (GOF) score that quantifies the degree of spatial correspondence between polygons in two different spatial maps. Bond-Lamberty et al. [13] used Mapcurves and k-means clustering to compare clusters with global International Geosphere–Biosphere Programme (IGBP) Land Cover Classification

for creating Decomposition Functional Type maps. The Mapcurves method can be used to add supervision (and thus labels) to unsupervised classification-based maps at a variety of resolutions, but it is dependent on labeled expert-derived maps to find the best spatial overlap, which are often at coarse resolutions and can be inaccurate at the field scale.

Deep learning neural networks, which learn the representative and discriminative features in a hierarchical manner from the provided data, are becoming increasingly adopted for image classification in the remote sensing community [190]. Convolutional Neural Networks (CNN) have shown excellent performance in many computer vision and machine learning problems [163]. However, most approaches using CNNs on multi-/hyper-spectral imagery use coarse datasets at small spatial scales. Additionally, there often is a lack of ground-truth data collected in the field for validation.

In this study, we evaluated optical and SAR datasets for high-resolution land cover mapping on the Seward Peninsula in the State of Alaska, USA. We focus on unsupervised classification (k-means clustering and Mapcurves) and supervised (i.e., CNN) approaches for improving vegetation classification. Specifically, the Mapcurves method is used to improve resolution and reduce noise in a publicly available vegetation dataset over the region. Then we built a CNN model using updated vegetation maps for training to classify the datasets. The paper is structured as follows: (1) we describe the remote sensing datasets used in the study and data processing performed; (2) we describe the unsupervised classification of remote sensing datasets and the Mapcurves-based method for assigning vegetation class labels; (3) we describe CNN-based supervised classifications; (4) and we validated our vegetation maps using vegetation plot datasets collected in the field at our study sites. The discussion and conclusion provide an overview of the derived classifications, highlighting the benefits and limitations of SAR and optical datasets for high-resolution vegetation mapping at the field scale.

4.3 Study Area

The study area selected for this research is located on the Seward Peninsula on the western coast of Alaska. The Seward Peninsula experiences a semi-maritime climate that is controlled by the Bering Sea and sea surface conditions (especially sea-ice extent) [72]. The Seward Peninsula hosts vegetation transitions from boreal forest to tundra [152], making this part of Alaska an important region for characterizing vegetation distribution. We focused our analysis at a watershed on the middle of the Seward Peninsula (Figure 4.1), where intensive field campaigns to study hydrology, biogeochemistry, and vegetation are being conducted by the NGEE Arctic project. The bounding region of the study area was determined by the overlapping raster boundaries from the SPOT-5 and EO-1 Hyperion imagery. Additional details are contained in Section 4.4.1.

The selection of the Seward Peninsula by the NGEE Arctic project was based on an analysis indicating that western Alaska is a proxy for the future ecological and climatic regime of the North Slope of Alaska toward the end of the century [67]. The Kougarok watershed (65° 09′ 44″ N, 164° 49′ 07″ W) has an area of 1.75 km^2 and consists of low Arctic tundra dominated by open low mixed shrub-sedge tussock tundra communities [177]. The mean annual temperature around Kougarok is -2.4°C and the mean annual temperature in July is 11.0°C, while the mean annual precipitation is 102.1 mm [118]. The Kougarok area is a zone of nearly continuous permafrost with an active layer that has a mean thickness of 56 cm [64].

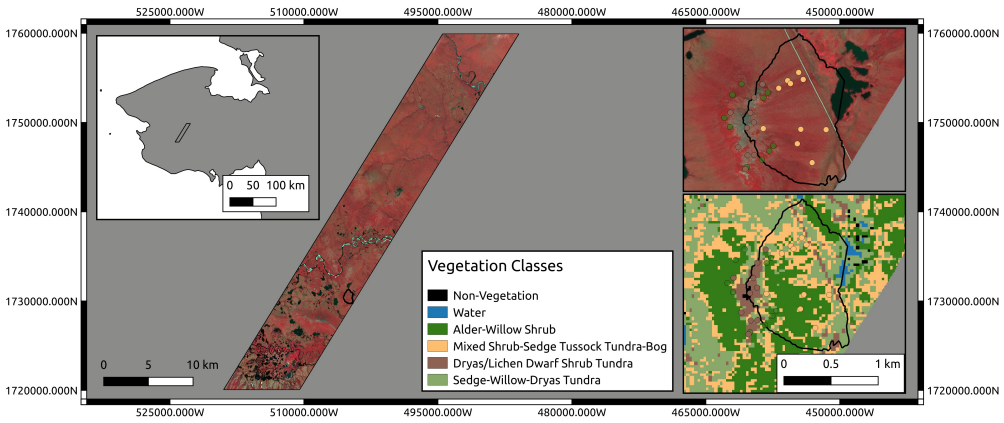


Figure 4.1: The study area located on the Seward Peninsula, showing the 2.5 m SPOT 5 false-color image. The Kougarok watershed is located in the lower section of the SPOT 5 image, zoomed in images on the right show the vegetation plot localities and a publicly available 30 m Alaska Existing Vegetation Type (AKVET) (http://akevt.gina.alaska.edu/) map used in the study.

4.4 Methodology

The methodology section follows the structure shown in Figure 4.2. Section 4.4.1 discusses the geospatial datasets used in this study and how they were acquired and processed. Section 4.4.2 discusses the pre-processing of the remote sensing datasets. Section 4.4.3 discusses the stratification of landscape using unsupervised clustering and how vegetation labels were assigned to the clusters. Section 4.4.4 discusses our CNN based supervised classification approach using the unsupervised classification based vegetation map for training. Section 4.4.5 discusses the validation statistics across the whole study region and using the field data.

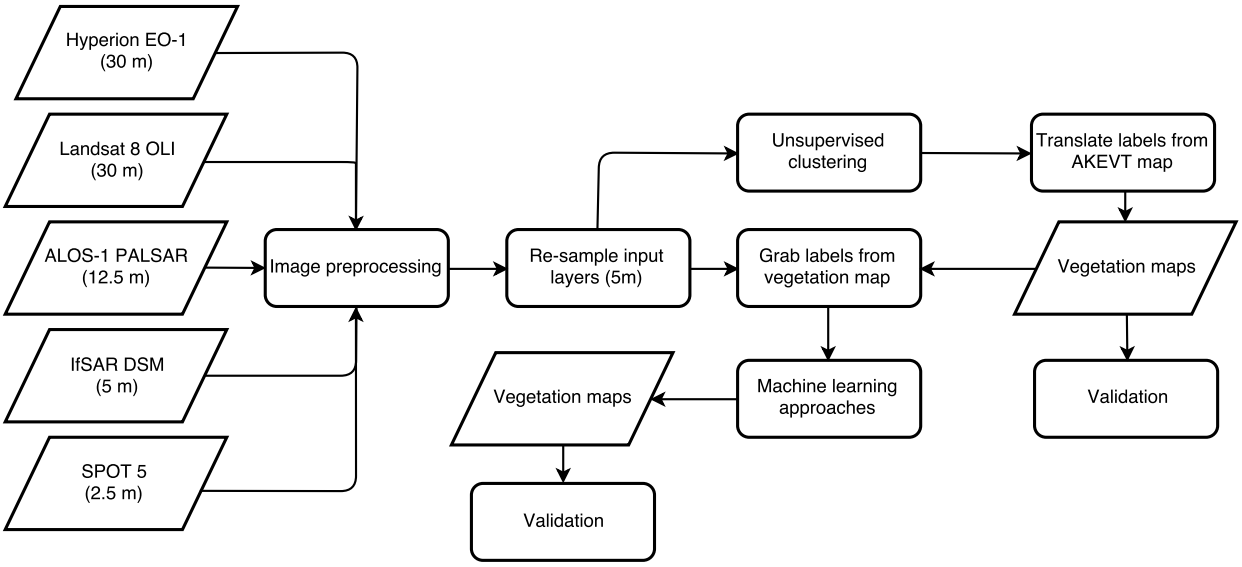


Figure 4.2: Steps applied for the processing of the remote sensing datasets to develop vegetation classifications.

4.4.1 Geospatial and *in situ* datasets

This section will describe how we collected our data sources. We used datasets derived from ALOS-1 PALSAR, Satellite for Observation of Earth (SPOT-5), and Interferometric Synthetic Aperture Radar (IfSAR) for vegetation mapping in the Seward Peninsula. ALOS-1 PALSAR datasets were collected from the Alaska Satellite Facility (https://www.asf.alaska.edu/sar-data/palsar/). Digital Elevation Model (DEM) IfSAR and SPOT-5 data were collected from the Geographic Information Network of Alaska (http://gina.alaska.edu/). We acquired the 30 m Alaska Existing Vegetation Type (AKEVT; http://akevt.gina.alaska.edu/) vegetation map and clipped the dataset to our study region. The AKEVT map consisted of six main vegetation classes for our study region based on Alaska vegetation classification [177]. Table 4.1 shows the area distribution of the vegetation classes present in the study region.

Some vegetation classes were very small and merged into other classes of similar strata. This was also done based on the Alaska vegetation classification system [177]. For example, the willow shrubs classification covered only 0.38% of the study region and

was merged into the Alder-Willow Shrub class. We mapped six vegetation types in our study region: (1) Alder-Willow Shrub, (2) Mixed Shrub-Sedge Tussock Tundra-Bog, (3) Dryas/Lichen Dwarf Shrub Tundra, (4) Sedge-Willow-Dryas Tundra, (5) Non-Vegetated (i.e., snow-ice, rock, sand, gravel), and (6) Water.

Sampling of vegetation plots in the field utilized methods recommended for the Arctic region by the authors of the Arctic Vegetation Archive prototype for northern Alaska [179]. Vegetation plots were selected subjectively in areas of homogenous vegetation and field sampling included: 1) complete vascular plant, bryophyte, and lichen species lists and their percent cover, 2) percent cover and mean height of each plant functional group, 3) site description, and 4) permanent marking and geo-referencing of plots. All plots were classified with respect to the Alaska Arctic Tundra Vegetation Map (AATVM) [133] for the following vegetation types: Willow-Birch Tundra, Alder Shrubland, Tussock Tundra, Shrubby Tussock Tundra or Alder Savanna, Dwarf Shrub Lichen Tundra, and Acidic Mountain Complex. These vegetation types were crosswalked to the AKEVT map resulting in three main classes of vegetation including Mixed Shrub-Sedge Tussock Tundra-Bog, Dryas/Lichen Dwarf Shrub Tundra, and Alder-Willow Shrub. Table 4.1 shows the crosswalk, number of plots, and the size of field plots by vegetation type.

Table 4.1: Area (km^2) of the AKEVT vegetation classes for the study region (SR) and the Kougarok watershed (KW). The crosswalk, number of plots, and the size of field plots by vegetation type are also presented. The gray columns indicate no data.

AKEVT Class	SR Area	KW Area	AATVM Class	Samples	Plot
Alder-Willow Shrub	72.38	0.57	Alder Shrubland	5	5×5 m
			Willow-Birch Tundra	5	2.5×2.5 m
Mixed Shrub-Sedge Tussock Tundra-Bog	117.61	0.45	Tussock Tundra	5	2.5×2.5 m
			Shrubby Tussock Tundra	5	2.5×2.5 m
Dryas/Lichen Dwarf Shrub Tundra	20.02	0.15	Dwarf Shrub Lichen Tundra	5	2.5×2.5 m
			Acidic Mountain Complex	5	2.5×2.5 m
Sedge-Willow-Dryas Tundra	113.34	0.54			
Non-Vegetated	5.53	0.007			
Water	6.00	0.02			

4.4.2 Data Processing

All datasets were processed in Alaska Albers Equal Area Conic (EPSG:3338), NAD83 horizontal datum and NAVD88 vertical datum. The ALOS PALSAR L-band SAR image has dual polarization (FBD) of HH (horizontal transmitting, horizontal receiving) and HV (horizontal transmitting, vertical receiving). The ALOS-1 PALSAR product was radiometric and terrain corrected, more information can be found at https://www.asf.alaska.edu/sar-data/palsar/. The ALOS-1 PALSAR image was in the form of the normalized radar cross section of gamma-naught (γ^0), and the backscatter is normalized by the realistic illumination area under an assumption of scattering uniformity (i.e., Lambertian) [155, 151]. This can be expressed as:

$$\gamma^0 = \frac{\sigma^0}{\cos\theta} \tag{4.1}$$

where σ^0 is the backscattering coefficient and θ is the local incidence angle. The Lee filtering algorithm (7×7 window) was applied in the Sentinel Application Platform (SNAP) to reduce the speckle [98]. Such filters preserves feature edges that can influence a classification [26]. The speckle filtered mosaics over the study region were created of γ^0 values for HH and HV polarization modes.

The SPOT-5 satellite images used in this study were gathered by the "Alaska Statewide Digital Mapping Initiative", which produced a new statewide orthomosaic that provides complete multispectral coverage of the state at 2.5 m spatial resolution. This satellite image mosaic is the first consistent, high-resolution, high-accuracy, digital orthoimagery base layer ever produced across the entire state of Alaska. The SPOT-5 orthoimage used to create the digital orthoimages were acquired between 2009 and 2013. The SPOT-5 orthoimage was produced to 1:24,000 National Map Accuracy Standards (NMAS) with a CE90 of 12.2-meters. Three statewide mosaics are available: color infrared (CIR), psuedo-natural color, and panchromatic (grayscale). We used the CIR SPOT-5 orthoimage over our study area, which consists of the green (0.50–0.59 μm), red (0.61–0.68 μm), and near infrared (0.78–0.89 μm) bands. Quantum Spatial and Fugro Geospatial, Inc. performed the image processing, orthorectification, and mosaicing of the datasets. The SPOT-5 orthoimage was radiometrically corrected for tone, balance, and geometry quality control along tile edges for terrain and linear features. The Alaska Statewide Digital Mapping Initiative (http://www.alaskamapped.org/ortho) has more details on the image processing for the SPOT-5 orthoimage.

The EO-1 Hyperion and Landsat 8 OLI images were collected from USGS (https://earthexplorer.usgs.gov/), with EO-1 Hyperion consisting of 198 calibrated bands (0.4–2.5 μm) and Landsat 8 OLI consisting of 11 bands, with 9 bands (0.4–2.29 μm) used in this study. The terrain corrected versions for EO-1 Hyperion (L1T) and Landsat 8 OLI (Level-1) were processed. The EO-1 Hyperion and Landsat 8 OLI datasets were converted to Top Of Atmosphere (TOA) reflectance according to the USGS documentation.

Table 4.2: Multi-sensor vegetation classification cases

Case	Remote Sensing Datasets
D1	EO-1, IfSAR
D2	EO-1, Landsat 8 OLI, IfSAR
D3	EO-1, ALOS-1 PALSAR, IfSAR
D4	EO-1, SPOT-5, IfSAR
D5	EO-1, ALOS-1 PALSAR, SPOT-5, IfSAR
D6	EO-1, ALOS-1 PALSAR, Landsat 8 OLI, IfSAR
D7	EO-1, SPOT-5, Landsat 8 OLI, IfSAR
D8	Landsat 8 OLI, IfSAR
D9	Landsat 8 OLI, ALOS-1 PALSAR, IfSAR
D10	Landsat 8 OLI, SPOT-5, IfSAR
D11	ALOS-1 PALSAR, IfSAR
D12	ALOS-1 PALSAR, SPOT-5, IfSAR
D13	SPOT-5, IfSAR
D14	EO-1, Landsat 8 OLI, ALOS-1 PALSAR, SPOT-5, IfSAR

All of the remote sensing datasets were re-sampled by nearest-neighbor interpolation to pixel aggregation to 5 m. The SPOT-5, PALSAR, and IfSAR datasets were normalized to between 0 and 1 for consistency among the TOA datasets. This was performed by:

$$z_i = \frac{x_i - min(x)}{max(x) - min(x)} \tag{4.2}$$

where x = (x_1,...,x_n) are the DN values of the datasets and z_i is the the normalized data. We decided to test fourteen sets of classifications using the variables described in 4.2. For the remaining of the paper we may refer to each specific dataset as D by number (e.g., D14 refers to merging all the datasets together).

Table 4.3: Spectral and topographic variables used in the optical- and SAR-derived classifications

Sensor Group	Predictor Variable	Unit	Date
ALOS-1 PALSAR	HH HV	γ^0 γ^0	29 August 2007
SPOT-5	Green, Red, NIR (0.5–0.9 μm)	DN	June-September 2009 – 2012
IfSAR	Elevation	m	July 2012
EO-1	198 spectral bands (0.4 to 2.5 μm)	DN	24 June 2015
Landsat 8	9 spectral bands (0.4 - 2.29 μm)	DN	17 August 2016

4.4.3 Unsupervised Classification based Vegetation Mapping

We used a k-means algorithm for stratification of the remote sensing datasets (Table 4.3). The k-means algorithm clusters a dataset ($\vec{X}_1$, $\vec{X}_2$, …, $\vec{X}_n$) with n records into a desired number of clusters, k, equalizing the full multi-dimensional variance across clusters [59]. The number of clusters, k, is supplied as an input and remains fixed. The k-means algorithm starts with initial centroid vectors ($\vec{C}_1$, $\vec{C}_2$, …, $\vec{C}_k$) and calculates the Euclidean distance of each pixel ($\vec{X}_i$, $1 \leq i \leq n$) to every centroid ($\vec{C}_j$, $1 \leq j \leq k$), classifying it to the closest existing centroid. The centroid vector is recalculated as the vector mean of all dimensions of each pixel assigned to that centroid. This classification and re-calculation process is iteratively repeated until fewer than some fixed proportion of observations changes their cluster assignment between iterations. For this study, convergence was assumed once fewer than 0.05% of the observations changed cluster assignments between two iterations. Hoffman et al. [66] developed a parallel version of the k-means algorithm to accelerate convergence, handle empty cluster cases, and obtain initial centroids through a scalable implementation of the Bradley and Fayyad [14] method. Kumar et al. [90] extended this to a fully distributed and highly scalable parallel version of the k-means algorithm for analysis of very large datasets, we used these same methods in this study.

Prior to performing the unsupervised classification (k-means), we also performed principal component analysis (PCA) on the remote sensing data set for feature reduction and to account for correlations among data from various sensors. Top three components that explained ~99% variance in the data were then used as inputs to k-means clustering.

The k-means algorithm is unsupervised and while each cluster is described by unique combination of multi-variate data set, they lack an ecologically understandable label. To add automated supervision to this unsupervised process, we applied the Mapcurves method to compare unsupervised k-means based clusters to labeled expert-derived maps of biomes, vegetation, and ecoregions [55]. Utilizing spatial overlays with available expert-derived maps, this technique exploits the knowledge contained in a collection of maps to identify biome characteristics. Generalized vegetation maps were produced by combining clusters according to their degree of spatial coincidence with the AKEVT vegetation labels. Goodness of fit (GOF) scores were calculated for each vegetation class. GOF is a unitless measure of spatial overlap between map categories:

$$GOF = \sum_{\text{class}} \frac{C}{B+C} \times \frac{C}{A+C} \tag{4.3}$$

where A is the map that is being compared, B is the reference map, and C is the proportion of the reference category (B) that overlaps with the tested category (A). GOF algorithm computes a score between each intersecting categories pairs between maps A and B, and accounts for matching and well as mismatching areas. Each category in map A is assigned the category in map B it intersected with highest GOF score. In our case, a high GOF score represents high spatial overlap between the clusters (k) from the unsupervised clustering classifications and the AKEVT map. Each cluster is then assigned a vegetation class from the AKEVT map it intersected with the highest GOF score, producing a fully labeled vegetation map based on unsupervised classification. We will refer to this method as the Unsupervised Classification based Vegetation Map (UCVM) approach for the rest of the paper.

4.4.4 Convolutional Neural Network Models for Vegetation Mapping

We developed supervised CNN models which maps the input image (x_i) over a series of layers, to a probability vector ($\hat{y}_i$), over the different classes. Our approach uses patches of images as inputs into a simplified CNN architecture, where the entire patch is predicted to be a single vegetation class. We chose to test three different patch sizes of 3×3, 6×6, and 12×12, where each patch contains 9, 36, and 144 pixels (5 m resolution), respectively. Langford et al. [92] used a similar architecture and compared it to a semantic segmentation architecture, which classifies every pixel. Each layer of the CNN consists of the convolution of the previous layer output with a set of learned filters, passing the responses through a rectified linear function ($relu(x)$ = max(x,0)), pooling over local neighborhoods, and local contrast operation that normalizes the responses across feature maps [88, 189]. The top few layers of the network are conventional fully-connected networks and the final layer is a softmax classifier [189]. We set the epoch size, one forward pass and one backward pass of all the training examples, to 100 for all of the models. Figure 4.3 shows our first CNN architecture used in this study. We implemented our CNN approach using the TensorFlow [1] and Keras framework [24] in Python. The `sparse_categorical_accuracy` metric was used in Keras using 10% of the data for validation while the remainder were used for training. The `sparse_categorical_accuracy` metric calculates the mean accuracy rate across all predictions for our multi-class classification problem.

We used two sets of training data to develop CNN models for all the cases (D#): 1) AKEVT map cropped to our study region, and 2) remote sensing based UCVM map developed using unsupervised classification approach (Section 4.4.3).

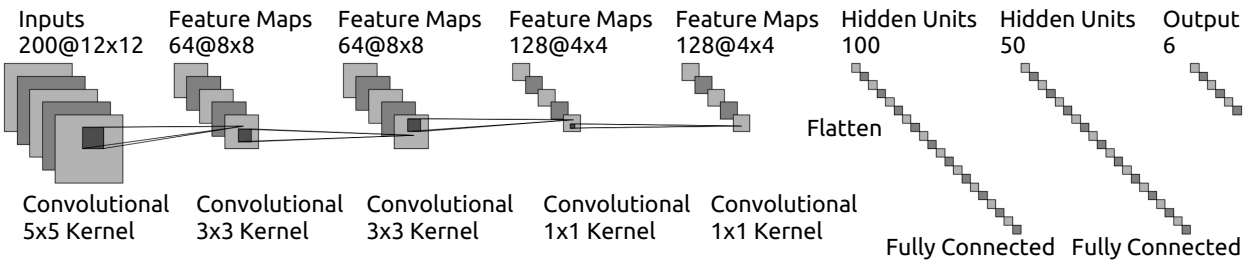


Figure 4.3: Example architecture of a seven layer CNN model. A 12 by 12 crop of an image (with 200 bands) is presented as the input. This is convolved with 64 different 1^{st} layer filters, with a kernel size of 5 x 5, using pooling with stride 2. Similar operations are repeated in the following layers. The last two layers are fully connected, taking features from the top convolutional layer as inputs. The final layer is a softmax function, corresponding to the number of classes.

4.4.5 Validation of vegetation maps

We used the precision-recall metric to evaluate our vegetation classifications, which is a useful measure of success of prediction when the classes are very imbalanced.

Precision (P) is defined as:

$$P = \frac{T_p}{T_p + F_p} \tag{4.4}$$

and Recall (R) is defined as:

$$R = \frac{T_p}{T_p + F_n} \tag{4.5}$$

where T_p = number of true positives, F_p = number of false positives and F_n = number of false negatives. A high recall, but low precision returns many results, yet most of the predicted labels are incorrect when compared to the training labels [128]. A system with high precision but low recall is just the opposite, returning very few results, but most of its predicted labels are correct when compared to the training labels [128]. An ideal system will have a high precision and high recall [128]. We also calculated the F1-score, which is defined as the harmonic mean of precision and recall [128].

$$F1 = 2\,\frac{P \times R}{P + R} \tag{4.6}$$

Vegetation maps were validated using two sets of data. 10% of the training map (AKEVT) that were held back during training were used for validation at the watershed scale. In addition, observations collected at 30 field vegetation plots were used for field scale validation of vegetation maps.

4.5 Results

4.5.1 Analysis of Remote Sensing Datasets

After the re-sampling of datasets to 5 m (Figure 4.2), all datasets were analyzed to understand the best attributes compared against the vegetation classes in the AKEVT dataset. We analyzed the patterns and distributions of each dataset in order to get a better understanding of the similarities and differences among their values for each vegetation class. Figure 4.4 shows the patterns in the EO-1 Hyperion dataset for each vegetation class. The water and non-vegetated classes had lower reflectance values through most bands (600–2500 nm) compared to the other classes. The Sedge-Willows-Dryas Tundra and Alder-Willow Shrub class had similar reflectance values for the majority of the bands with separation around 1500–1800 nm. There was a similar trend for the Mixed Shrub-Sedge Tussock Tundra-Bog and Dryas/Lichen Dwarf Shrub Tundra with separation around 1500–1800 nm.

Figure 4.5 presents the distribution, central value, and variability of the SPOT-5, PALSAR, IfSAR, and Landsat 8 values for the vegetation classes. The box-plot shows some sensors/bands may be better suited than the others for classifying certain vegetation types. The non-vegetated class shows the greatest range between the minimum and maximum values, indicating potential lumping of different vegetation types and thus potential sources of error in the AKEVT map. The Sedge-Willow-Dryas Tundra, Alder-Willow Shrub, Dryas/Lichen Dwarf Shrub Tundra, and Mixed Shrub-Sedge Tussock Tundra-Bog vegetation classes show little differences in values for most of the datasets.

Landsat 8 bands 5, 6, and 7, representing the near infrared (NIR) and shortwave infrared parts of the spectrum, provided the best distinction between vegetation classes.

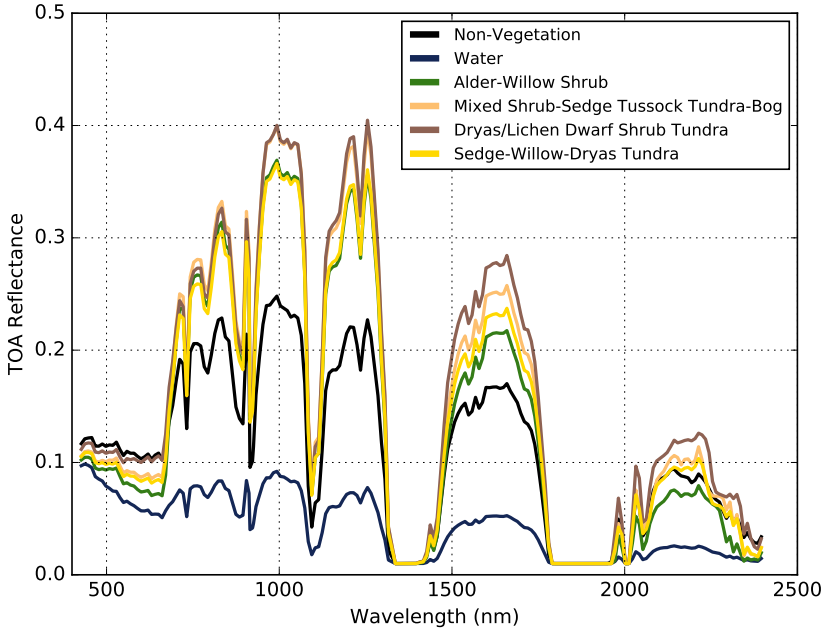


Figure 4.4: Spectral characteristics of the EO-1 Hyperion dataset (400-2500 nm) for each vegetation class.

Most of the vegetation classes showed sensitivity in the multi-spectral green, red, and NIR bands of SPOT-5; however, they also showed a large range of variability in their responses (Figure 4.5). The PALSAR HH polarizations distinguished the vegetation classes compared to HV polarization. All vegetation classes show well-distinguished topographic characteristics using IfSAR DSM. The DSM topographic properties of the vegetation classes had distinguishable differences. However, similar to SPOT-5, DSM showed a large range of variability. This variability was potentially caused by the resolution mismatch between high resolution of DSM and SPOT-5 (5 m and 2.5 m, respectively), compared to the 30 m resolution of AKEVT map.

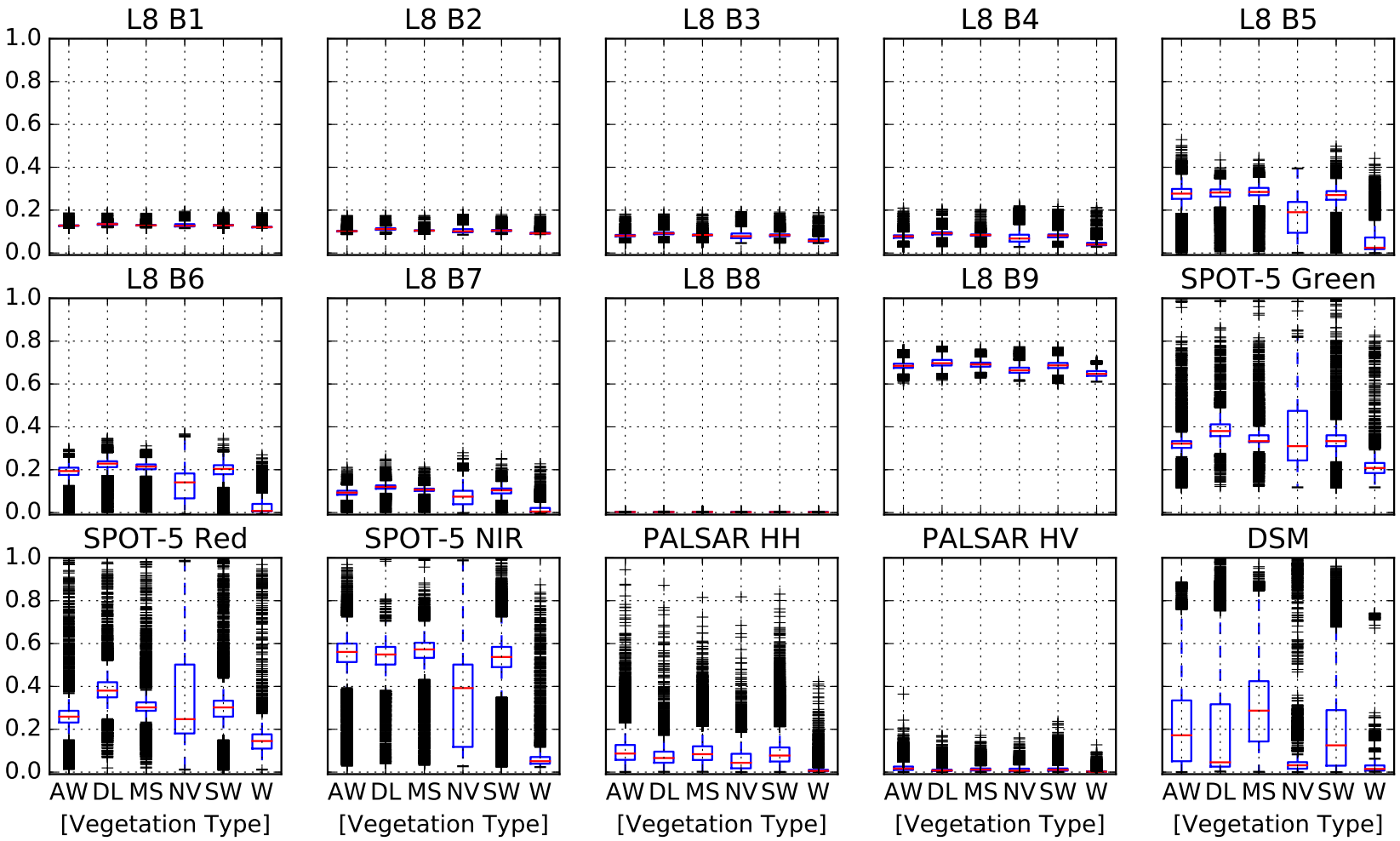


Figure 4.5: Box-plots representing variation in the DNs of Landsat 8 (L8 B1-B9), SPOT-5 data (green, red, NIR), ALOS-1 PALSAR (HH and HV), and IfSAR elevation values. The values were segregated by vegetation type, where AW, DL, MS, NV, SW, and W stand for Alder-Willow Shrub, Dryas/Lichen Dwarf Shrub Tundra, Mixed Shrub-Sedge Tussock Tundra-Bog, Non-Vegetation, Sedge-Willow-Dryas Tundra, and Water, respectively.

4.5.2 Vegetation Classifications

Unsupervised Classification based Vegetation Map (UCVM)

The k-means algorithm classifies the multi-variate dataset among specified number (k) of clusters while maximizing the inter-cluster variances and minimizing the intra-cluster variance in the data space. While classifying data among fewer clusters (k) tends to lump the multi-variate clusters (i.e. vegetation classes) together, using a larger number of clusters may define clusters with insignificant differences in remote sensing signatures across vegetation types. However, the Mapcurves [55] algorithm is very efficient at lumping similar classes in the reference map (i.e, unsupervised clusters) when comparing them to expert training maps (i.e, AKEVT). For that reason, we conducted our unsupervised classification at varying levels of division from small to large (k =10, 25, 50) and applied Mapcurves to each case (D1–14) and evaluated them for accuracy. Mapcurves assigns each cluster to a single vegetation class having the best fit in terms of GOF (Equation 4.3) calculated using spatial overlay, thus adding supervision to the unsupervised cluster maps resulting in fully labeled unsupervised clustering based vegetation map (UCVM).

Figure 4.6 shows the UCVM produced for the study region and the Kougarok watershed for Case D7 when clustered at k =50 level of division.

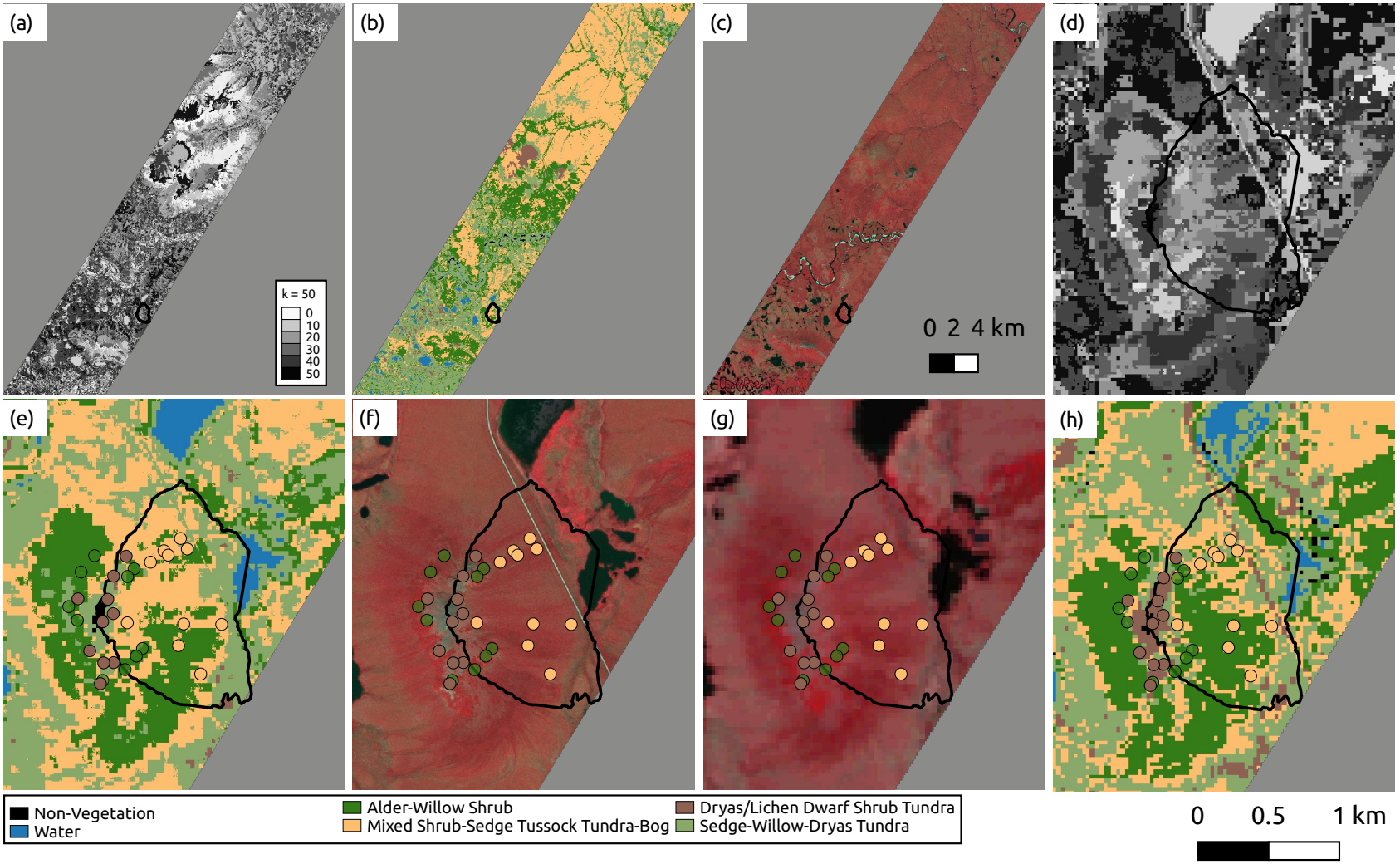


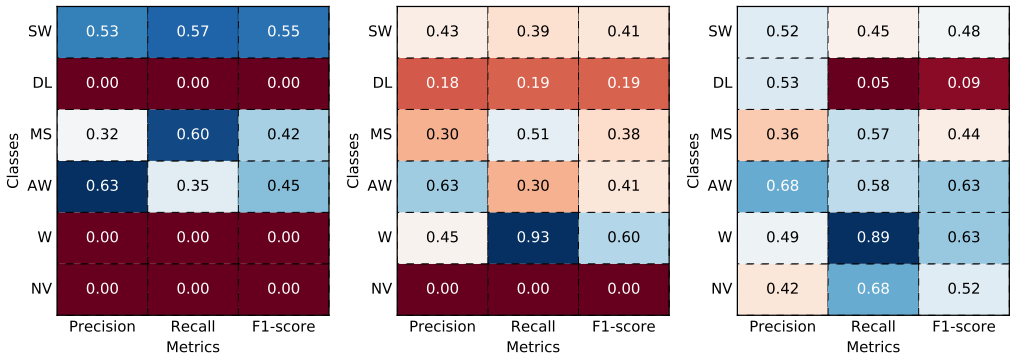
Figure 4.6: (a) Cluster value of 50 for D7 for the study region. (b) The reclassed map of D7 k=50 when performing UCVM for the study region. (c) SPOT-5 false color image for the study region. (d) Kougarok watershed of k=50 for D7. (e) The reclassed map of D7 k=50 when performing UCVM for the Kougarok watershed. (f) SPOT-5 false color image for the Kougarok watershed. (g) EO-1 Hyperion false color image for the Kougarok watershed. (h) The AKEVT map for the Kougarok watershed.

We calculated the precision, recall and F1 scores for UCVM maps for all $14 \times 3 = 42$ cases when compared to AKEVT for entire study region. Figure 4.7 shows the statistics for highest scoring cases when unsupervised clustering were conducted at k =10, 25, 50 levels of division.

All cased performed with low validation scores for when unsupervised clustering was done a low level of division (k=10), with D3 (Figure 4.7 (a)) achieving the best scores. The hyperspectral datasets (D1–D7 and D14) had the best overall scores, for all levels of divisions of unsupervised clustring. D6 (EO-1, ALOS-1 PALSAR, Landsat 8 OLI, IfSAR) performed the best for k=25 unsupervised clustering, with high validation scores for non-vegetated and water, but lower scores for Alder-Willow Shrub, Mixed Shrub-Sedge Tussock Tundra-Bog, and Sedge-Willow-Dryas Tundra; Dryas/Lichen Dwarf Shrub Tundra had the lowest scores (0.18, 0.19, 0.19 for precision, recall, and F1-score, respectively). However, this was the highest scoring case for Dryas/Lichen Dwarf Shrub Tundra; the low scores is most likely due to the smaller area presence in the region and thus low number of training samples (Table 4.1).

When clustering at the k =50 level of division, D7 (EO-1, SPOT-5, Landsat 8 OLI, IfSAR) had the highest score (also highest overall among all 42 cases) with the best scores for the Alder-Willow Shrub vegetation class, but low scores for Dryas/Lichen Dwarf Shrub Tundra. The Landsat 8 OLI and PALSAR datasets (D8, D9, and D11) were the best for mapping Mixed Shrub-Sedge Tussock Tundra-Bog, but were not successful at mapping the other vegetation classes. The SPOT-5 datasets (D10, D12, and D13) were better at mapping Alder-Willow Shrub compared to the Landsat 8 OLI and PALSAR datasets, but combining the EO-1 dataset had the best overall performance for all vegetation classes.

We also validated the UCVM maps within the Kougarok watershed against the 30 vegetation observations collected in the field (Table 4.1). Figure 4.8 shows the best scoring cases when unsupervised clustering were performed at k =10, 25 and 50 levels of division. Unsupervised clustering at higher levels of division (k =25, and 50) led to better scores than at fewer clusters (k =10). Similar to the findings in study region wide validation,



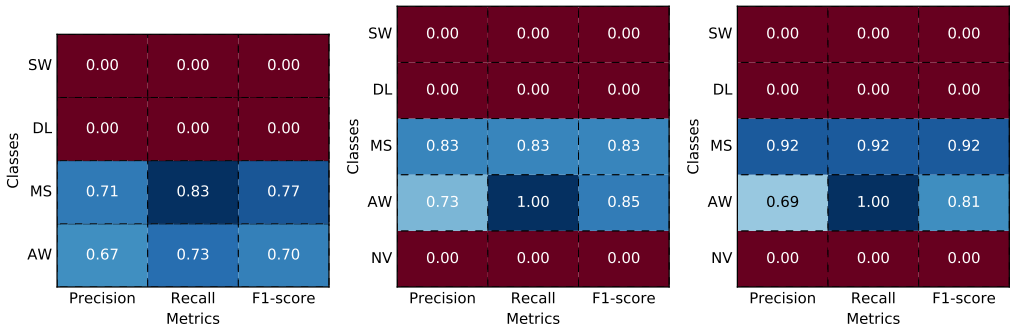
(a) D3 at k=10 **(b)** D6 at k=25 **(c)** D7 at k=50

Figure 4.7: Study region wide validation statistics for Cases D3 (EO-1, ALOS-1 PALSAR, IfSAR), D6 (EO-1, ALOS-1 PALSAR, Landsat 8 OLI, IfSAR), and D7 (EO-1, SPOT-5, Landsat 8 OLI, IfSAR) that performed best using k =10, 25, and 50 unsupervised clustering respectively. (AW: Alder-Willow Shrub; DL: Dryas/Lichen Dwarf Shrub Tundra; MS: Mixed Shrub-Sedge Tussock Tundra-Bog;, NV: Non-Vegetated; SW: Sedge-Willow-Dryas Tundra, and W: Water)

the cases using hyperspectral datasets (D1–D7 and D14) performed the best. D4 (EO-1, SPOT-5, IfSAR) performed the best for unsupervised clustering at k=10 and 25 levels of division, with high scores for Alder-Willow Shrub and Mixed Shrub-Sedge Tussock Tundra-Bog, but didn't map any Dryas/Lichen Dwarf Shrub Tundra classes. Case D7 using clustering at k=50 had the overall best scores for Alder-Willow Shrub and Mixed Shrub-Sedge Tussock Tundra-Bog. However, none of the UCVM maps were able to correctly map any of the 10 Dryas/Lichen Dwarf Shrub Tundra vegetation plots.

This is most likely due to noise in the UCVM re-labeling method, because While Dryas/Lichen Dwarf Shrub Tundra demonstrated distinguishing spectral characteristics, especially in the EO-1 dataset, compared to other vegetation classes (Figure 4.4), UCVM mis-clasified the field vegetation plots as Sedge-Willow-Dryas Tundra and Non-Vegetated. The Landsat 8 OLI and PALSAR datasets (D8, D9, and D11) performed better for mapping Mixed Shrub-Sedge Tussock Tundra-Bog, while the SPOT-5 datasets (D10, D12, and D13) demonstrated better performance mapping Alder-Willow Shrub for the entire study region.

UCVM maps produced using Case D7 with unsupervised classification at k =50 level of division (D7–K50) showed overall best accuracy and consistent validation statistics for both validation datasets for all vegetation classes. Thus, we selected D7–K50 as training dataset for developing CNN models in our study. Table 4.4 shows the area distribution of all vegetation classes using UCVM based on Case D7 and k =50 unsupervised clustering, which matches area distribution trends for the AKEVT map fiarly well (Table 4.1) except for lower area for the Dryas/Lichen Dwarf Shrub Tundra class.



(a) D4 at k=10 **(b)** D4 at k=25 **(c)** D7 at k=50

Figure 4.8: Validation statistics using field vegetation observations in the Kougarok watershed for Cases D4 (EO-1, SPOT-5, IfSAR), D4, and D7 (EO-1, SPOT-5, Landsat 8 OLI, IfSAR) that performed best using k = 10, 25, and 50 unsupervised clustering respectively. (AW: Alder-Willow Shrub; DL: Dryas/Lichen Dwarf Shrub Tundra; MS: Mixed Shrub-Sedge Tussock Tundra-Bogr;, NV: Non-Vegetated; SW: Sedge-Willow-Dryas Tundra, and W: Water)

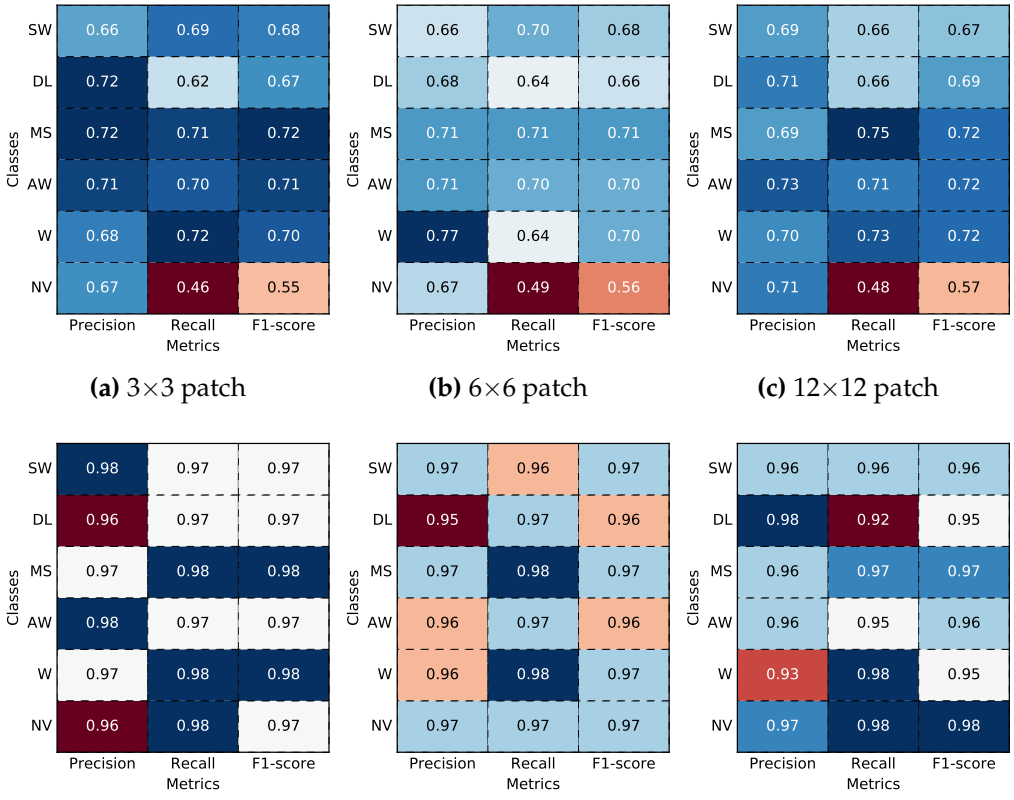
Table 4.4: Area of the D7 vegetation classes for the study region and the Kougarok watershed.

AKEVT Land Cover	Area (km^2)	Kougarok Area (km^2)
Alder-Willow Shrub	73.33	0.55
Mixed Shrub-Sedge Tussock Tundra-Bog	135.27	0.58
Dryas/Lichen Dwarf Shrub Tundra	14.88	0.07
Sedge-Willow-Dryas Tundra	102.14	0.50
Non-Vegetation	2.24	0.02
Water	7.04	0.04
Total	334.89	1.75

Classification by CNNs

We developed CNN models for Case D7 trained using AKEVT and UCVM (developed by Case D7–K50). A series of CNN models were developed using patch sizes of 3×3, 6×6, and 12×12 for Case D7. Figure 4.9 shows the validation statistics for developed CNN models using 10% of data not used in training for validation. While the CNN models developed with different patch sizes demonstrated comparable performance, 3×3 patch size showed the best validation scores. CNN models trained using UCVM dataset outperformed the CNN models trained using AKEVT demonstrating the value added by the unsupervised classification of remote sensing data. 3×3 patch size CNN models trained using Case D7 and AKEVT (D7-CNN-AKEVT) achieved an average 0.82, 0.70, and 0.73 for precision, recall, and F1-score, respectively. Similar CNN models training using UCVM dataset (D7-CNN-UCVM) scored on average 0.58, 0.65, and 0.61 for precision, recall, and F1-score, respectively Figure 4.10 shows how the CNN models convergence behavior when using the two training dataset for 100 epoch. While CNN model trained using AKEVT dataset converged with ∼70% accuracy, the CNN models trained using UCVM dataset achieved ∼97% accuracy. We believe that the lower training scores using the AKEVT can be attributed to the noise within the dataset.

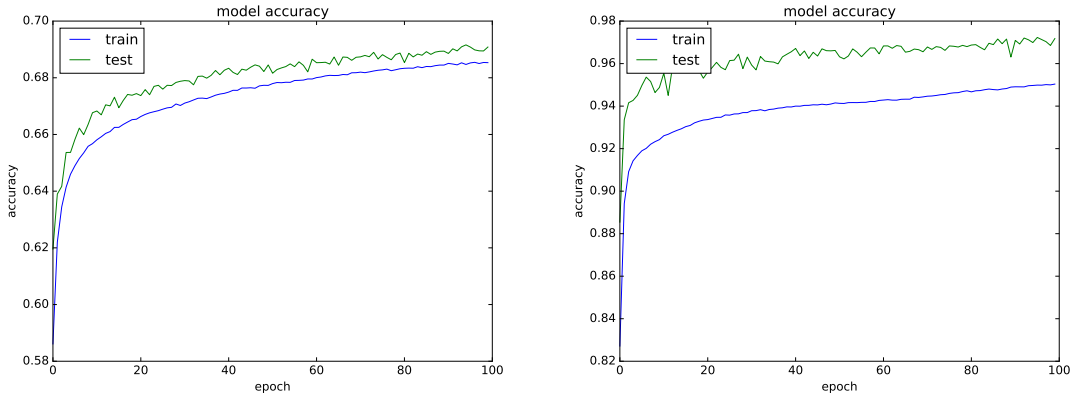
Alder-Willow Shrubs and Mixed Shrub-Sedge Tussock Tundra-Bog were accurately mapped by all the CNN models. Both were dominant vegetation classes in the region and thus were represented in the traning dataset (Table 4.4) used to develop the CNN models. Additionally, these vegetation types demonstrate distinguishing spectral characteristics, especially in the EO-1, SPOT-5, LANDSAT 8 OLI and IfSAR datasets (Figure 4.4 and 4.5). The Dryas/Lichen Dwarf Shrub Tundra class was mapped with lowest scores, perhaps due to the low number of training samples and spectral properties similar to the other vegetation classes as observed in Section 4.4.3. The mapping accuracy for Non-Vegetated class was worst for all CNN models, primarily due to the initial noise within the AKEVT dataset.



(a) 3×3 patch **(b)** 6×6 patch **(c)** 12×12 patch

(d) 3×3 patch **(e)** 6×6 patch **(f)** 12×12 patch

Figure 4.9: Validation of the CNN models trained using AKEVT dataset (a–c) and UCVM dataset (d–f) within the study region. (AW: Alder-Willow Shrub; DL: Dryas/Lichen Dwarf Shrub Tundra; MS: Mixed Shrub-Sedge Tussock Tundra-Bogr;, NV: Non-Vegetated; SW: Sedge-Willow-Dryas Tundra, and W: Water)



(a) D7 CNN with AKEVT labels **(b)** D7 CNN with UCVM labels

Figure 4.10: CNN model model convergence through 100 epochs for patch size of 3×3.

CNN model based vegetation maps outperformed UCVM maps in our validations against the field vegetation observations. Figure 4.12 shows the validation statistics for CNN models developed using 3×3, 6×6, and 12×12 patche sizes for Case D7 trained using AKEVT (D7-CNN-AKEVT) and UCVM data (D7-CNN-UCVM). Based of field based validation, 3×3 path based CNN model trained using AKEVT (D7-CNN-AKEVT) performed the best with average precision, recall and F1 score of 0.79, 0.71, and 0.73, respectively. This was primarily driven by the high validation scores for the Alder-Willow Shrubs class, with precision, recall, and F1-score of 0.71, 0.91, and 0.80, respectively. Figure 4.11 shows the 3×3 path based CNN model trained using AKEVT (D7-CNN-AKEVT) for the vegetation plots. When trained using UCVM map, CNN models developed using 6×6 patch performed the best with average scores of 0.52, 0.65, and 0.58 for precision, recall, and F1-score, respectively. CNN models trained using UCVM map performed overall best for the Alder-Willow Shrub and Mixed Shrub-Sedge Tussock Tundra-Bog class, however, were unable to classify the Dryas/Lichen Dwarf Shrub Tundra class.

Table 4.5 shows the comparison of various vegetation maps developed in our study against the 30 field vegetation plots. Instances where the developed vegetation maps failed to match field based observation of vegetation class are highlighted in the table. Vegetation maps developed using various methods in this study show improved accuracy

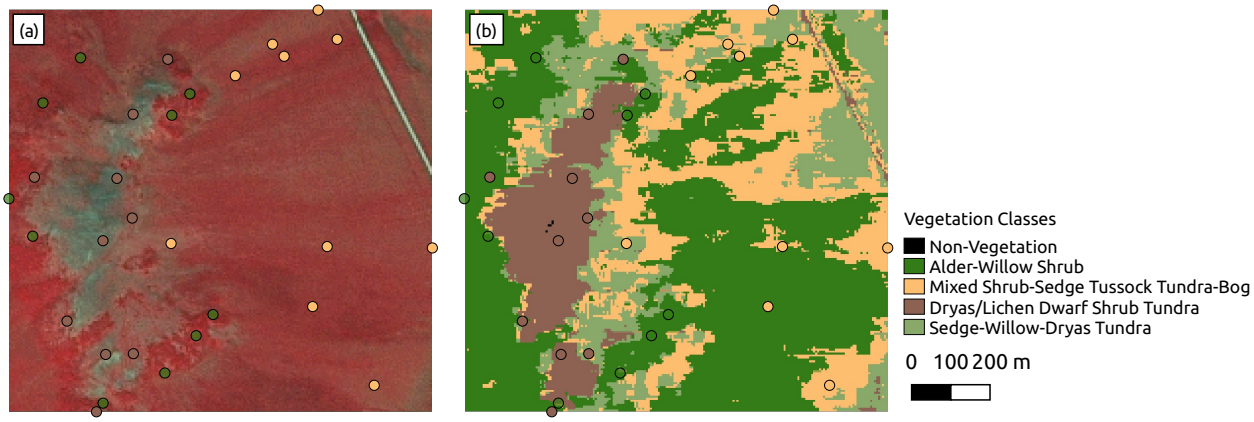


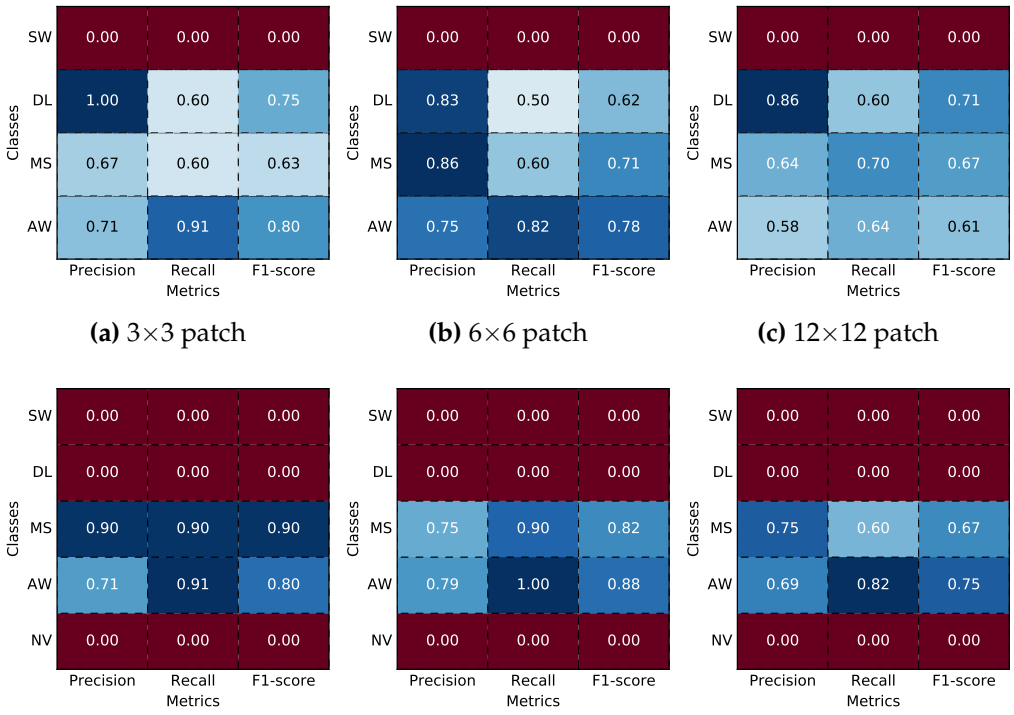
Figure 4.11: SPOT-5 false color image (a) and CNN vegetation map (b) surrounding the vegetation plots.

in mapping vegetation classes on the ground, compared to AKEVT map which the models were trained on. Rich and high resolution remote sensing data underlying quantitative methods developed in this study help ensure consistency across and within vegetation classes and add value upon original datasets to develop high resolution vegetation maps.

4.6 Discussion

4.6.1 Importance of high-resolution datasets

High-resolution (∼0.3 m – 10 m) datasets (e.g., IKONOS, QuickBird, SPOT, and WorldView) are becoming increasingly available in Arctic and boreal ecosystems. These datasets provide opportunities to evaluate and improve upon existing vegetation and landcover maps in the Arctic such as AKEVT, or at national scale like National Land Cover Database (NLCD) maps. One of the main goals of this study was to develop high-resolution vegetation datasets for the Seward Peninsula of Alaska, to aid ecological and modeling research in Arctic. This study was a first step towards development of machine learning approaches to fuse high-resolution datasets from a range of remote sensing to develop a accurate and high resolution mapping of vegetation and land cover in Arctic ecosystems. One of the goals our study was to explore available satellite remote sensing products and develop techniques to combine them for vegetation studies in Arctic.



(a) 3×3 patch **(b)** 6×6 patch **(c)** 12×12 patch

(d) 3×3 patch **(e)** 6×6 patch **(f)** 12×12 patch

Figure 4.12: Validation statistics using field based vegetation observations for the CNN models trained using AKEVT dataset (a–c) and UCVM dataset (d–f) within the study region. (AW: Alder-Willow Shrub; DL: Dryas/Lichen Dwarf Shrub Tundra; MS: Mixed Shrub-Sedge Tussock Tundra-Bog;, NV: Non-Vegetated; SW: Sedge-Willow-Dryas Tundra, and W: Water)

We identified the EO-1, SPOT-5, Landsat 8 OLI, IfSAR datasets (D7) to perform best for the models developed. EO-1 hyperspectral dataset was most valuable to distinguish between the main vegetation classes (Figure 4.4), while the SPOT-5 and Landsat 8 OLI datasets provided additional spectral information to improve the vegetation mapping (Figure 4.5). In addition, the SPOT-5 provided the high spatial resolution commensurate with the scales field vegetation studies are conducted.

While models developed using ALOS-1 PALSAR did not perform as well as well as other cases, they able to classify the Alder-Willow Shrub and Mixed Shrub-Sedge Tussock Tundra-Bog accurately. SAR-based classifications have been shown to be accurate for mapping forests and water in Arctic ecosystems [25, 144]. However, few studies have used SAR for Arctic vegetation mapping [36, 37], with most of these studies using C and

X bands. Limited classification accuracy using ALOS-1 PALSAR in our models may have been due to the choice of particular datasets used in this study and need to be further explored.

While we focused our study at the Seward Peninsula, where the NGEE Arctic project is conducting extensive research, the datasets used in this study exist for the entire state of Alaska and thus our study can be extended for state-wide mapping. We focused on freely available datasets but other high-resolution commercial satellites platform (like WorldView-2, 3 [181, 93]) may be well suited to improve land cover mapping at high resolution. The remote sensing data used represents, like in many other remote sensing studies, a snapshot in time that reflects specific environmental conditions on the ground. There exists a huge database of freely available optical and SAR images that could used for understanding vegetation dynamics across Alaska. The recent increases in shrub cover is an important area of interest in terrestrial Arctic research, due to increases in local evapotranspiration, soil active layer depth, and permafrost degradation [61]. Using spatio-temporal time series of high spectral and spatial resolutions data, methods developed in this study can applied to map and study vegetation dynamics in Arctic.

4.6.2 Vegetation classification

Vegetation maps developed using UCVM as well as CNN approaches demonstrated good accuracy during our validation exercise. The low precision, recall, and F1-score for the UCVM (Figure 4.7) could be due to noise in the AKEVT map which was developed using limited and spatially sparse field observations. Unsupervised classification step in the UCVM creates classes that are spectrally similar and thus remove some of the noise and confounding effects. Thus, CNN models trained using UCVM leads to better accuracy as compared to those trained using AKEVT (Figure 4.10). Compared to AKEVT, UCVM map provides a higher resolution mapping of vegetation classes (Figure 4.6). When validated against the 30 field vegetation plot, UCVM exhibited high accuracy for the Alder-Willow Shrub and Mixed Shrub-Sedge Tussock Tundra-Bog vegetation classes, however, was unable to map the Dryas/Lichen Dwarf Shrub Tundra class (Figure 4.8). Inability

of the approach to map Dryas/Lichen Dwarf Shrub Tundra class was perhaps due to its small area presence in the region thus smaller training sample size to train the model (Table 4.1). Moreover, the differences in resolution between the 30 m AKEVT map and our classifications at 5 m might be adding nuances in a direct comparison.

We trained two CNN models using varying image patch sizes where a single vegetation class is predicted for the entire patch. The first set CNN models were trained using the original AKEVT labels and we saw improved accuracies compared to UCVM for the study region (Figure 4.9 a–c). The second set of CNN models were trained using the UCVM map (Table 4.4) and showed higher accuracies and validation scores (Figure 4.9 d–f) for the study region.

Validation using field based observations show that the CNN models trained using both AKEVT and UCVM map achieved high accuracies for the Alder-Willow Shrub and Mixed Shrub-Sedge Tussock Tundra-Bog classes but could not classify the Dryas/Lichen Dwarf Shrub Tundra class well (Figure 4.12). Overall, the CNN based models performed better for field-scale mapping compared to the UCVM method (Table 4.5).

The patch size used for developing the CNN models plays important role in the classification. Each image patch is input to the model independently, which means that only the "intra-patch" context information is considered [44] when building the CNN models. The correlations between patches are not taken into account, which might lead to gaps between patches [44]. However, this may only apply to objects with strong continuity, such as urban features, which was not present in our imagery. Use of right patch sizes that can differentiate vegetation classes on landscape would lead to improved classification, and thus we explored a range of path sizes in our study to identify the best patch size parameters. In future studies, we would like to explore CNN architectures that leverage semantic segmentation for images and classifies each pixel into one of the pre-defined classes, which may results in better mappings at field-scale. One approach could be based on the u-net architectures, where low-level feature maps are combined with higher-level ones, which enables precise localization [139].

We believe that noise exists in the AKEVT dataset and our UCVM approach was to help reduce the noise and provide improved labeled data for training the CNN models. The UCVM approach did help provide a dataset that was substantially different and produced accurate CNN models trained using the data (Figure 4.10). The low accuracy scores for the Dryas/Lichen Dwarf Shrub Tundra could be due to the way UCVM method merged the vegetation classes (Figure 4.6). High quality training data are critically important for training machine learning methods like CNN. We used the best available vegetation maps to train our CNN models. However, within the NGEE Arctic project, we are undertaking efforts to collect more field-based observations, which can be used as training data set for developing CNN models and allow for development of highly accurate maps. Understanding the distribution of vegetation in Arctic tundra is critically important to understand the ecological processes in Arctic ecosystems, which is undergoing changes due to climate change. This study provides a machine learning framework to exploit data from a range of remote sensing platforms becoming available in the region to improve our understanding of patterns and distribution of diverse Arctic vegetation.

4.7 Conclusions

Accurate vegetation maps are important for understanding terrestrial biosphere processes in Arctic ecosystems. Given the importance of vegetation dynamics in Alaska and the associated impacts of climate change, there is a need for up-to-date and high-resolution mapping. We evaluated the use of SAR and optical imagery for vegetation mapping in the southern Seward Peninsula, Alaska at 5 m resolution. We developed a multi-sensor data fusion approach to exploit data available for a variety of different remote sensing platforms at a range of spatial resolutions to characterize and map vegetation in Arctic ecosystem. We also developed unsupervised classification and Convolution Neural Network models using remote sensing datasets for accurate and high resolution mapping of vegetation. We collected vegetation observations across key vegetation types at our field sites in the Kougarok watershed and validated our vegetation products against

them. Vegetation maps developed in our study demonstrated high accuracy through our validation exercises. Our analysis shows that CNN models are capable of accurately mapping vegetation based on multi-sensor remote sensing data sets. The EO-1, SPOT-5, Landsat 8 OLI, IfSAR datasets were found to provide the best predictive ability in our CNN models, specifically for Alder-Willow Shrub and Mixed Shrub-Sedge Tussock Tundra-Bog. Additionally, high spectral resolution datasets were demonstrated to provide distinguishing features among vegetation communities in the Arctic. Thus, the fusion of high spatial and spectral datasets are ideal for mapping vegetation at the field to regional scale in Arctic ecosystems. Our study provides one of the most accurate, high resolution, field validated vegetation map for the Seward Peninsula of Alaska.

Table 4.5: Comparison of the various vegetation maps developed for Case D7 against the 30 field vegetation plots. (AW: Alder-Willow Shrub; DL: Dryas/Lichen Dwarf Shrub Tundra; MS: Mixed Shrub-Sedge Tussock Tundra-Bog; NV: Non-Vegetated; SW: Sedge-Willow-Dryas Tundra, and W: Water). The highlighted areas indicate were the vegetation class identified by vegetation maps developed in our did not match observations from vegetation plots.

Plot Number	Field Obs.	D7 CNN UCVM	D7 CNN AKEVT	D7 UCVM	AKEVT
1	MS	MS	MS	MS	MS
2	MS	MS	AW	MS	MS
3	AW	AW	AW	AW	AW
4	DL	SW	DL	SW	DL
5	AW	AW	AW	AW	AW
6	MS	MS	MS	MS	MS
7	MS	MS	SW	MS	SW
8	AW	AW	AW	AW	SW
9	DL	AW	AW	AW	SW
10	AW	AW	AW	MS	SW
11	AW	AW	AW	AW	AW
12	DL	AW	MS	AW	DL
13	DL	AW	AW	AW	AW
14	MS	MS	MS	MS	MS
15	MS	MS	MS	MS	SW
16	MS	MS	MS	SW	MS
17	MS	MS	MS	MS	MS
18	MS	AW	AW	AW	AW
19	MS	MS	SW	MS	MS
20	AW	AW	AW	AW	SW
21	AW	AW	AW	AW	SW
22	AW	AW	AW	AW	AW
23	DL	MS	MS	MS	SW
24	DL	MS	MS	MS	SW
25	DL	MS	DL	SW	DL
26	AW	AW	AW	SW	AW
27	AW	AW	AW	AW	MS
28	DL	SW	DL	NV	DL
29	DL	SW	DL	SW	DL
30	DL	SW	DL	SW	AW
Percent Accuracy		0.63	0.70	0.53	0.53

Chapter 5

Wildfire Mapping in Interior Alaska Based on MODIS and Daymet Products

5.1 Abstract

Amplified warming in the Arctic has likely increased the rate of landscape change and disturbances in northern high latitude regions. Wildfire activity has also increased in the past decade across Alaska due to natural and anthropogenic changes. Satellite remote sensing is a valuable tool for monitoring occurring in remote, northern environments over multiple time scales. The Moderate-Resolution Imaging Spectroradiometer (MODIS) sensor has been proven effective at mapping fires using observed middle–infrared and thermal infrared brightness temperatures. Meteorological datasets are also important for understanding wildfire attribution. Daymet provides gridded estimates of daily weather parameters for North America derived from selected meteorological station data and various supporting data sources, and has 1 km $\times$ 1 km spatial resolution and uses a daily time step. Training data selection and specific input variables (e.g., image channels) have a large impact on the overall accuracy of the image classification. High-dimension datasets should be reduced so that only uncorrelated important variables are used in classifications. Random Forest (RF) is a widely used algorithm for classification of remotely sensed data and has shown to provide key insights into variable selection. Additionally, it can hard to process large amounts of data needed for wildfire mapping over large areas. Google Earth Engine (GEE) provides a large catalog of satellite imagery and geospatial datasets with planetary-scale analysis capabilities using cloud computing. This chapter seeks to utilize GEE for processing MODIS and Daymet products for wildfire mapping and the use of RF for understanding which features are the most significant.

5.2 Introduction

The Arctic is changing at unprecedented rates due to climate change, natural disturbances, and anthropogenic development [43]. The Arctic is also projected to warm at a rate twice that of the global average in the coming century [159]. These changes are expected to impact sea ice, snowpack, permafrost, and other components of the Arctic system in the coming century [95]. Arctic tundra, boreal forests, and peatlands are already undergoing

major changes, and can be seen by the thawing of permafrost [12, 102], increasing disturbances (e.g., wildfires) [157], thermokarst development (physical depression of ground surface) [94, 48], and drying of lakes [19].

Alaska ecosystems are shaped by large scale (glacial retreat, fire, flooding, etc.) or small scale (thermokarst, fallen trees, etc.) disturbances and have evolved specific responses to each kind of disturbance. These changes can lead to feedback effects on patterns and trends of carbon and nutrient cycling [187]. For example, fire disturbance could play a major role in carbon release from boreal ecosystems [171]. However, the recovery of CO_2 fluxes following a fire disturbance is extremely variable and difficult to model [75]. Disturbances in Arctic and boreal ecosystems can occur at a variety of spatial and temporal scales, with nearly all natural disturbances are either directly or indirectly climatically driven [33].

Wildfires are the dominant disturbance impacting the Boreal forest [43]. Differences in fire regimes can occur between Alaska's ecoregions [67] and can have an impact on fire frequency and size [76]. Fire events in the boreal zone can be at a high frequency (105 year fire return interval for 1920–2009 [82]) and very large size (>1,000 km^2) [83]. Tundra fire events are generally rare and small in size (average of 30-55 km^2) [82]. However, evidence shows that climate change has led to an increase in fire occurrence and size in tundra regions [68]. One example is the 2007 Anaktuvuk River Fire on the North Slope of Alaska, which is the largest fire on record (1039 km^2 burned) for the Tundra biome. Another example is the 2004 wildfire season when extreme drought conditions caused a record wildfire year [129].

Remotely sensed data have been widely used to characterize disturbances in northern latitude ecosystems [161, 47, 82, 78]. An example of derived dataset of disturbances is the National Monitoring Trends in Burn Severity (MTBS) Burned Area Boundaries Dataset, which is generated by multi-temporal Normalized Burned Ratio (NBR) Landsat data. The MTBS utilizes the near and short-wave infrared parts of the spectrum. However, in the western continental United States, Alaska, and Hawaii, MTBS only maps fires greater or equal to 1,000 acres [38].

Another popular method for wildfire mapping uses the Normalized Difference Vegetation Index (NDVI), a remotely sensed indicator of photosynthetic capacity [141, 169]. NDVI provides the means to monitor changes in land surface phenology (LSP), the annual temporal patterns of variation in vegetation greenness. NDVI is one of the most commonly used vegetation indices and is widely available from satellite sensors, such as the Moderate-Resolution Imaging Spectroradiometer (MODIS), a sensor on board NASA's Terra and Aqua satellites that has a spatial resolution of 250 m^2 and daily temporal resolution. The spatial and temporal resolution makes MODIS a valuable tool for mapping disturbances over large areas.

Furthermore, band ratios between near and mid IR promote the minimization of illumination effects. Deviations from expected LSP development can be seen as the first indications of important changes in forest health [57, 113, 175]. Additionally, other MODIS products (i.e., land surface temperature (LST)) have been shown to be beneficial for wildfire mapping [164].

The Daymet data product provides daily mosaicked gridded estimates of weather parameters for North America calculated from meteorological station observations via extrapolation and interpolation algorithms [167]. Daymet variables have been used in remote sensing studies for monitoring surface trends spanning multiple years. For example, Daymet and MODIS LST were compared for monitoring thermal time in urban areas over long periods for assessing seasonal dynamics; showing that Daymet values were closer to the observations made by Global Historical Climatology Network (GHCN) [87]. Daymet and Landsat were used for mapping crop yields from multiple states and years in the Midwestern United States [105].

Earth science data are now accessible for free, and can be rapidly processed within Google's Earth Engine (GEE) Platform (Gorelick et al. [49]). The data warehouse includes satellite imagery, meteorological data, elevation data, and atmospheric data, with many of the datasets are updated on a daily basis, and users have the ability to upload their own data for analysis. Analyses run over these data are automatically parallelized to run across many CPUs in the Google cloud (Gorelick et al. [49]). These capabilities have been used

for crop yield estimation (Lobell et al. [105]), generate forest loss and gain maps globally over 12 years using 654,000 Landsat scenes (Hansen et al. [54]), and compute phenology-based synthesis land cover classifications using Landsat 8 imagery (Simonetti et al. [153]). Daymet dataset has recently been updated to cover the entire state of Alaska, thus an innovative framework for understanding if the variables are important for disturbance mapping is needed.

While most studies focus on singular wildfire events, this study seeks to understand which remote sensing variables are important for mapping wildfires for the 2004 wildfire season (70 fires). When applying data mining and machine learning algorithms on high-dimensional data, a critical issue is known as the curse of dimensionality [100]. Feature selection, as a type of dimension reduction technique, has been proven to be effective and efficient in handling high-dimensional data [101]. For this study, the feature selection will be analyzed using varying subsets of the remote sensing datasets. Random Forest (RF) is a widely used algorithm for remote sensing image classification and has been shown to be effective at variable importance [111]. RF will provide insights into identifying the most important features for wildfire mapping based on public datasets.

This chapter focuses on using the random forests algorithm, because it has been shown to identify important predictor variables and model the relationship between the predicted variables for fire events [150, 121]. This approach will be used to identify significant drivers from MODIS and Daymet datasets. This chapter seeks to identify the best features for wildfire mapping using MODIS and Daymet remote sensing products for Interior Alaska. The specific objectives of this study are to: (1) develop a RF model based on known wildfires and the remote sensing datasets, (2) evaluate the feature's potential for estimating wildfires based on the MTBS dataset, and (3) identify optimal remote sensing (e.g., NDVI, LST) for wildfire mapping.

5.3 Study Area

Because of Alaska's large geographical extent, complex terrain, and proximity to oceans and sea ice, its climate is highly regionalized [9]. Across the Arctic and boreal regions, the length of growing season period is an important factor for determining the spatial and temporal distribution of NDVI, which can vary significantly in Alaska from day of year (DOY) 92–300 for the boreal ecosystems and DOY 130–273 for the Tundra[171]. The study area (Figure 5.1) covered the interior regions of Alaska and was based on the climate division boundaries by [9]. The interior region was chosen primarily due to high number of wildfires. The study area is bounded to the north by the Brooks Range and to the south by the Yukon–Tanana uplands and Alaska Range [9]. It is relatively far from ocean influences and has a continental climate with relatively low precipitation [9].

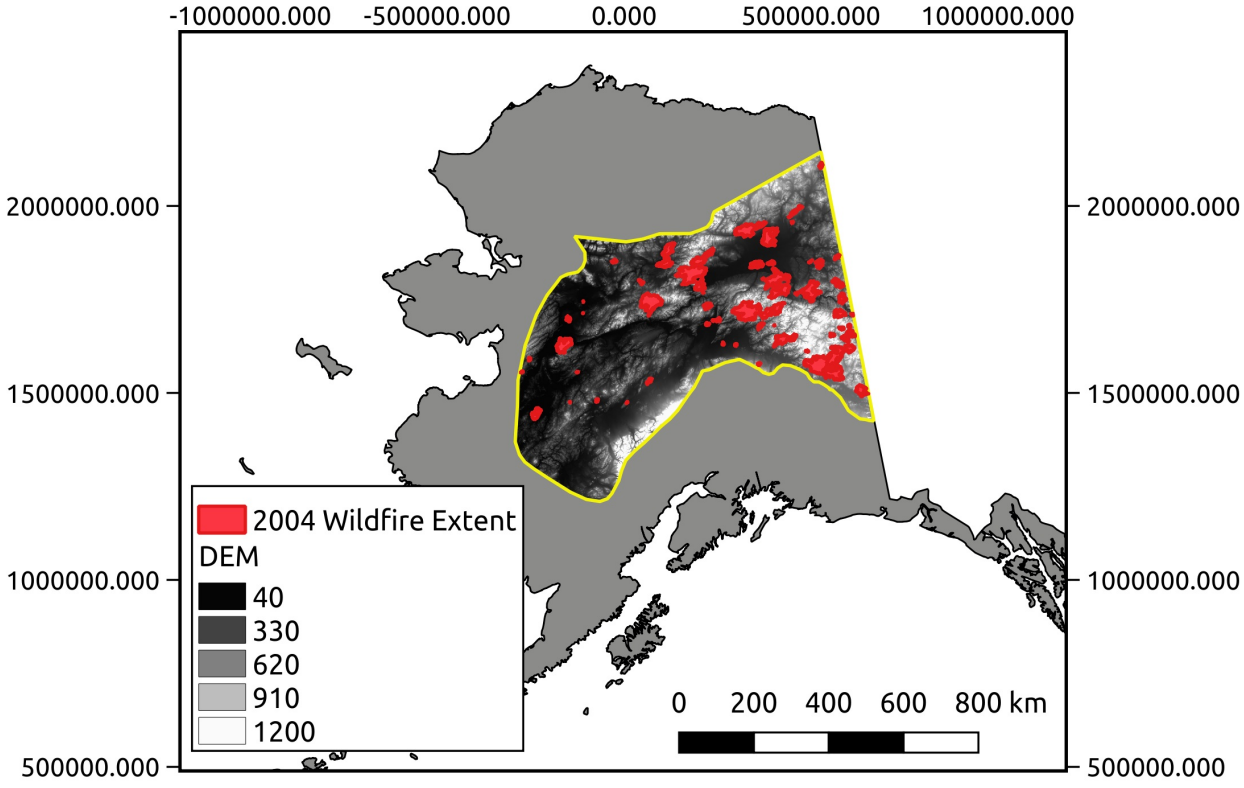


Figure 5.1: Study area for this study (yellow lines) and the 2004 wildfire boundaries (red polygons).

5.4 Methodology

The methodology section follows the structure shown in Figure 5.2. Section 5.4.1 discusses the geospatial datasets used in this study and how they were acquired. Section 5.4.2 discusses the image processing for the MODIS and Daymet products. Section 5.4.3 discusses our approach for identifying the best features and classification approach for wildfire mapping.

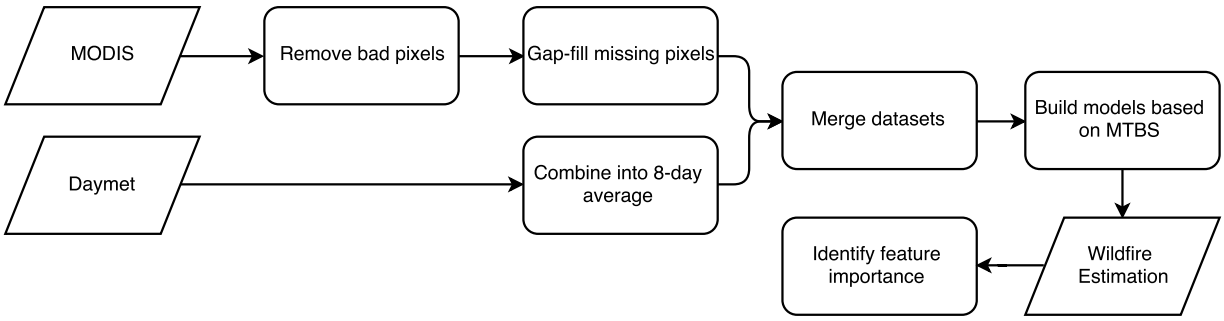


Figure 5.2: Flowchart for the proposed study.

5.4.1 Geospatial Datasets

This section describes the datasets used in this study and how they were gathered for processing. The vector layers included the Monitoring Trends and Burn Severity (MTBS) dataset, collected from https://www.mtbs.gov/. The MTBS burned areas boundaries dataset was used for the analysis. The wildfire year of 2004 was analyzed due to large amount of wildfires (Figure 5.3), with the intention that the work-flow could be replicated for other years. The vector layer was converted into a raster, where 0 represents no fire and 1 represents fire.

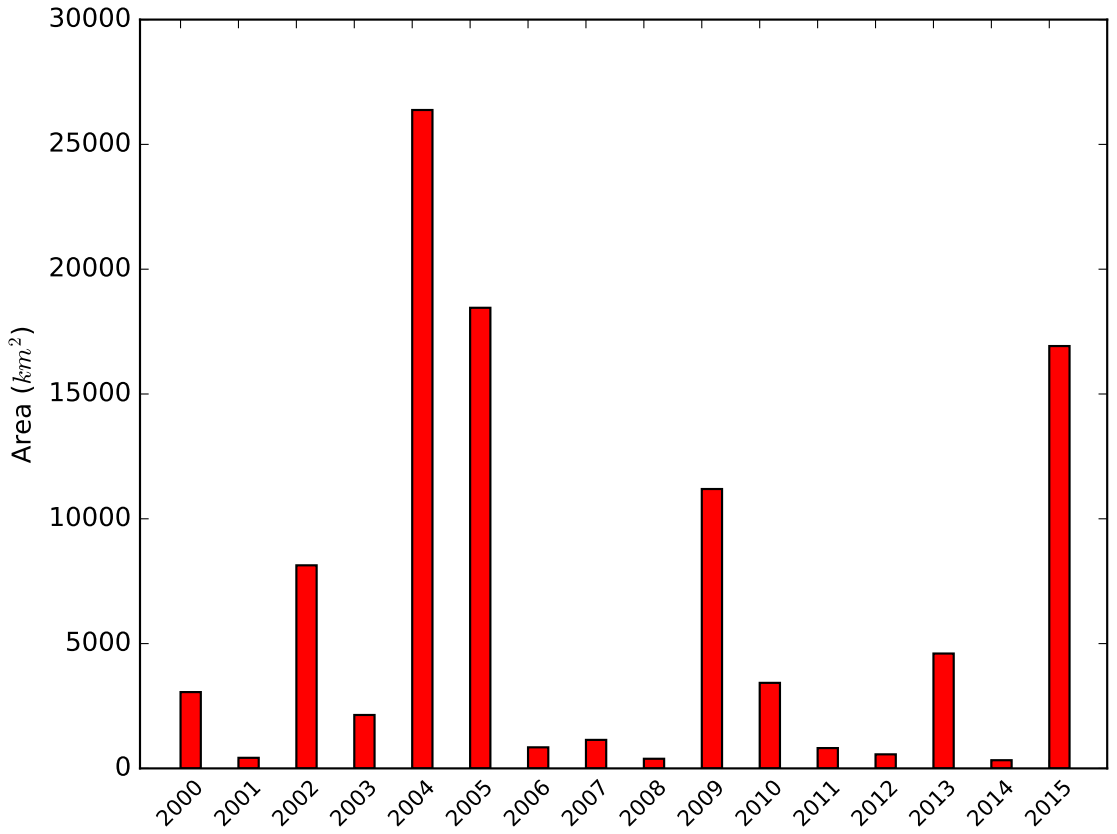


Figure 5.3: Area of wildfires across the study region from 2000 to 2015.

Table 5.1 lists the raster datasets used in this study. The Global Multi-resolution Terrain Elevation Data 2010 (GMTED2010) dataset was also processed in GEE. The GMTED2010 dataset contains elevation data for the globe collected from various sources. The MODIS and Daymet products from 2000–2015 were processed in Google Earth Engine's (GEE) platform (https://earthengine.google.com/datasets/). The MOD11A2 level-3 MODIS global Land Surface Temperature (LST) and Emissivity 8-day data are composed from the daily 1-kilometer LST product (MOD11A1) and stored on a 1-km Sinusoidal grid as the average values of clear-sky LSTs during an 8-day period. The MOD11A2 products are comprised of daytime and nighttime LSTs, quality assessment, observation times, view angles, bits of clear sky days and nights, and emissivities. The MODIS Surface-Reflectance

Product (MOD09A1) provides an estimate of the surface spectral reflectance values at 500 m resolution in a gridded format. Each pixel for both datasets contain the best possible observation during an 8-day period, selected as the one with large observation coverage, a low viewing angle, an absence of clouds or cloud shadow, and aerosol loading [106].

Table 5.1: Raster predictor variables used for the study.

Description	Resolution	Variable
GMTED2010	225 m	elevation (m)
	225 m	slope (%)
MOD09A1	500 m at 8 days	NDVI
	500 m at 8 days	EVI
	500 m at 8 days	SAVI
	500 m at 8 days	Bands 1–7 (459–2155 nm)
MOD11A2	1 km at 8 days	Daytime LST (Kelvin)
Daymet	1 km at daily	Daylight period (seconds)
	1 km at daily	Precipitation (mm)
	1 km at daily	Snow water equivalent (kg/m^2)
	1 km at daily	Maximum temperature ($^\circ C$)
	1 km at daily	Minimum temperature ($^\circ C$)
	1 km at daily	Shortwave Radiation (W/m^2)
	1 km at daily	Vapor Pressure (Pa)

5.4.2 Data processing

All MODIS products were processed from early-April through late-October in 2004. Contaminated pixels can often lead to false disturbance signatures when analyzing MODIS satellite time series datasets [176]. Thus, it's important to remove such data before

performing your analysis. The MODIS products include several files, including a quality control (QC) file. Per-pixel QC information in MODIS products allows for removal of most contamination of the NDVI signal related to clouds, aerosol and snow [106]. For all MODIS products, only the good data quality information from the QC file was kept and the rest was removed. For the MOD11A2, all pixels that have averaged LST errors less than 1K (i.e., QC = 0, 1, 5, 17, 21) were kept, while pixels with other QC values were removed.

Noise reduction and gap filling in time series of MODIS is an active area of research and needed for time series analysis [115]. The Savitzky-Golay algorithm was applied on the filtered MODIS products fill in the missing pixels. It has been shown that the Savitzky-Golay smoothing algorithm is a popular choice based on MODIS datasets [136]. Savitzky-Golay applies a moving-window quadratic polynomial function to the original time-series data and estimates new values for the center point of each moving-window [136].

GEE was used to aggregate the Daymet data over time. Specifically, the datasets were combined into 8-day averages to match the MODIS datasets. The GMTED2010, MODIS, and Daymet datasets were merged into two types of datasets for 2004, one using only the MODIS dataset and another using both MODIS and Daymet. The datasets were ordered in sequence, which consisted of one raster each with many channels starting from early-April through late-October. This was done in order to capture the abrupt changes in land surface characteristics that would be expected from a large wildfire season. Table 5.2 displays the two datasets used for identifying the best features for wildfire mapping.

Table 5.2: List of the number of variables used in the study.

Dataset	Variables
MODIS	288
MODIS & Daymet	456

5.4.3 Wildfire Mapping Algorithms

The RF machine learning algorithm was used for identifying the best features for wildfire mapping. RF has been shown to model a large number of explanatory variables

from satellite sensors [123]. Specifically, RF has been proven effective for land cover classification and burned area mapping using MODIS sensors [18, 42]. RF consists of a combination of tree classifiers where each classifier is generated using a random vector sampled independently from the input vector, and each tree casts a unit vote for the most popular class to classify an input vector [16]. RF consists of using randomly selected features or a combination of features at each node to grow a tree [16]. Bagging, a method to generate random subset of independent variables, is used for each decision tree to create the best split between the classes (fire or no-fire) [16]. RF provide an improvement over bagged trees using methods that decorrelates the trees. As in bagging, RF builds a number of decision trees on bootstrapped training samples.

The classification is performed by taking the most popular voted class from all the tree predictors in the forest [16, 123]. This classifier also provides the relative importance of different features during the classification process, which can be useful in feature selection [123]. For classification trees, we can add up the total amount that the Gini index decreases by splits over a given predictor averaged over all trees. We used variable importance to understand the relationships between the MODIS and Daymet datasets (Table 5.1). With RF, the Gini importance index is defined as the averaged Gini decrease in node impurities over all trees in the forest. The Gini importance index was calculated for each variable and will sum to 1. Scikit-learn, a Python API for machine learning, was used for building the random forest classification [128].

The MODIS, Daymet, and MTBS datasets were split into train and test categories for building the model. The datasets were split into 50 % for training and 50 % for validation. Table 5.3 shows the amount of data used for the training and testing for all datasets used. The MTBS No-Fire and Fire labels are unbalanced, thus a "balanced" mode that uses the values of y (i.e., MTBS values) to automatically adjust weights inversely proportional to class frequencies in the input data.

The precision-recall metric was used to evaluate the wildfire classifications, which is a useful measure of success of prediction when the classes are very imbalanced. A high recall but low precision returns many results, but most of the predicted labels are incorrect

when compared to the training labels [128]. A system with high precision but low recall is just the opposite, returning very few results, but most of its predicted labels are correct when compared to the training labels [128]. An ideal system will have a high precision and high recall [128]. The F1-score was also provided, which is defined as the harmonic mean of precision and recall [128].

Table 5.3: Number of pixels (500×500) used for training and testing the RF algorithm.

	MODIS	MODIS/Daymet	MTBS No-Fire	MTBS Fire
Train	895,822	895,822	843,688	52,134
Test	895,822	895,822	843,272	52,550

5.5 Results

5.5.1 Analyzing Spectral Variations

The Boundary fire was analyzed for this study area (Figure 5.4), which was the largest wildfire during the 2004 season. The Boundary wildfire consisted of 538,167 acres burned and started on 13 June, 2004 (DOY 165). Time series of MODIS variables extracted from the burn perimeter are shown in Figure 5.5. This shows the averaged pixels for the entire boundary starting for the entire year. Bands 1–4 (centered at 648 nm, 858 nm, 470 nm, 555 nm, respectively) shows high reflectance properties for the start of the year (DOY 0–100), which could be due to snow cover. Bands 5–7 (centered at 1240 nm, 1640 nm, and 2130 nm) show lower reflectance properties for the same period. NDVI, EVI, and SAVI show the low values during the DOY 0-100, however EVI showed slightly higher values.

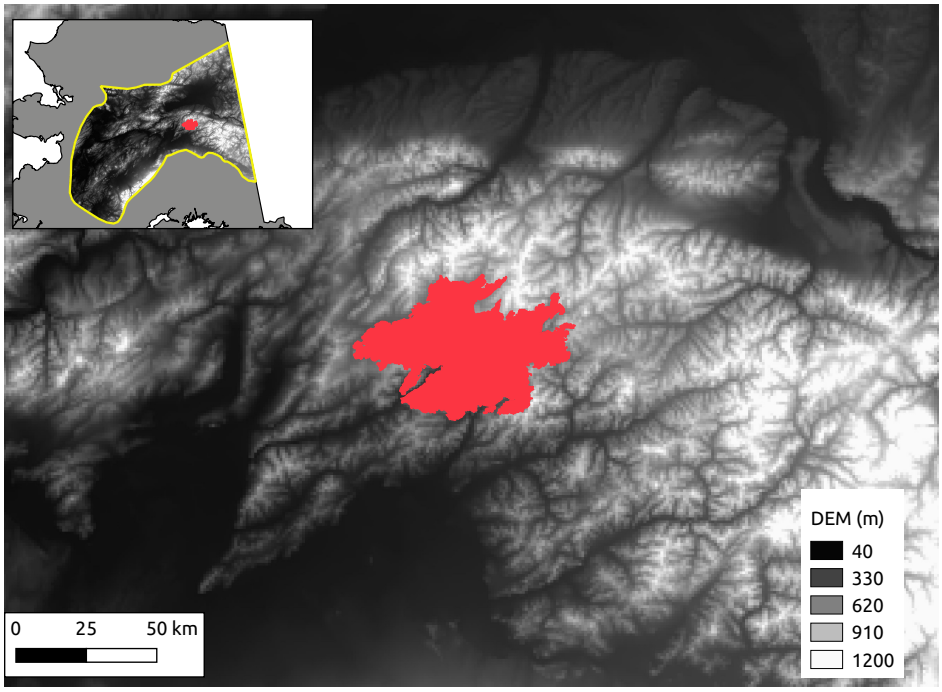
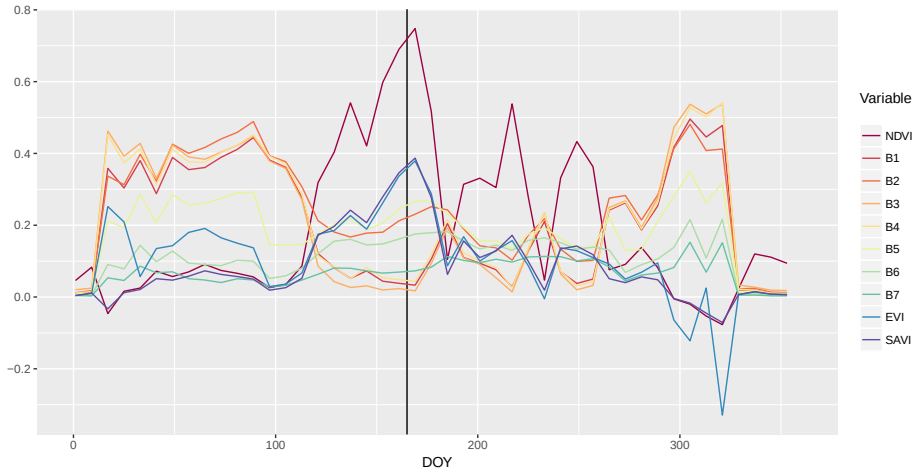
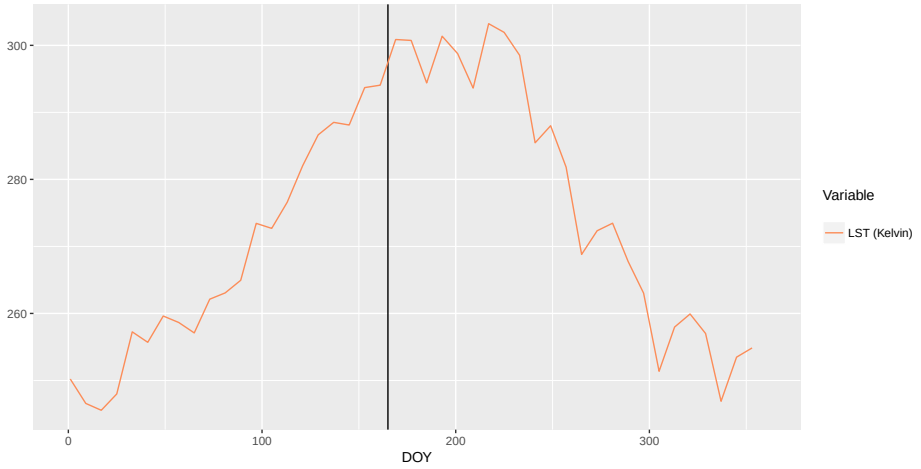


Figure 5.4: Boundary wildfire perimeter and location.

The time series values for NDVI, EVI, and SAVI increase starting from 100, as the vegetation growth increases. Once the wildfire starts (DOY 165) the NDVI, EVI, and SAVI abruptly drops in value. Additionally, Bands 1, 3, and 4 show an increase in values, primarily due to the high reflectance properties of the fire. Bands 2 and 5 shows a slight drop in values once the wildfire starts. Bands 6 and 7 show little to no variation from the wildfire. LST shows some fluctuations in the response after the wildfire but not as abrupt as other MODIS variables.



(a)

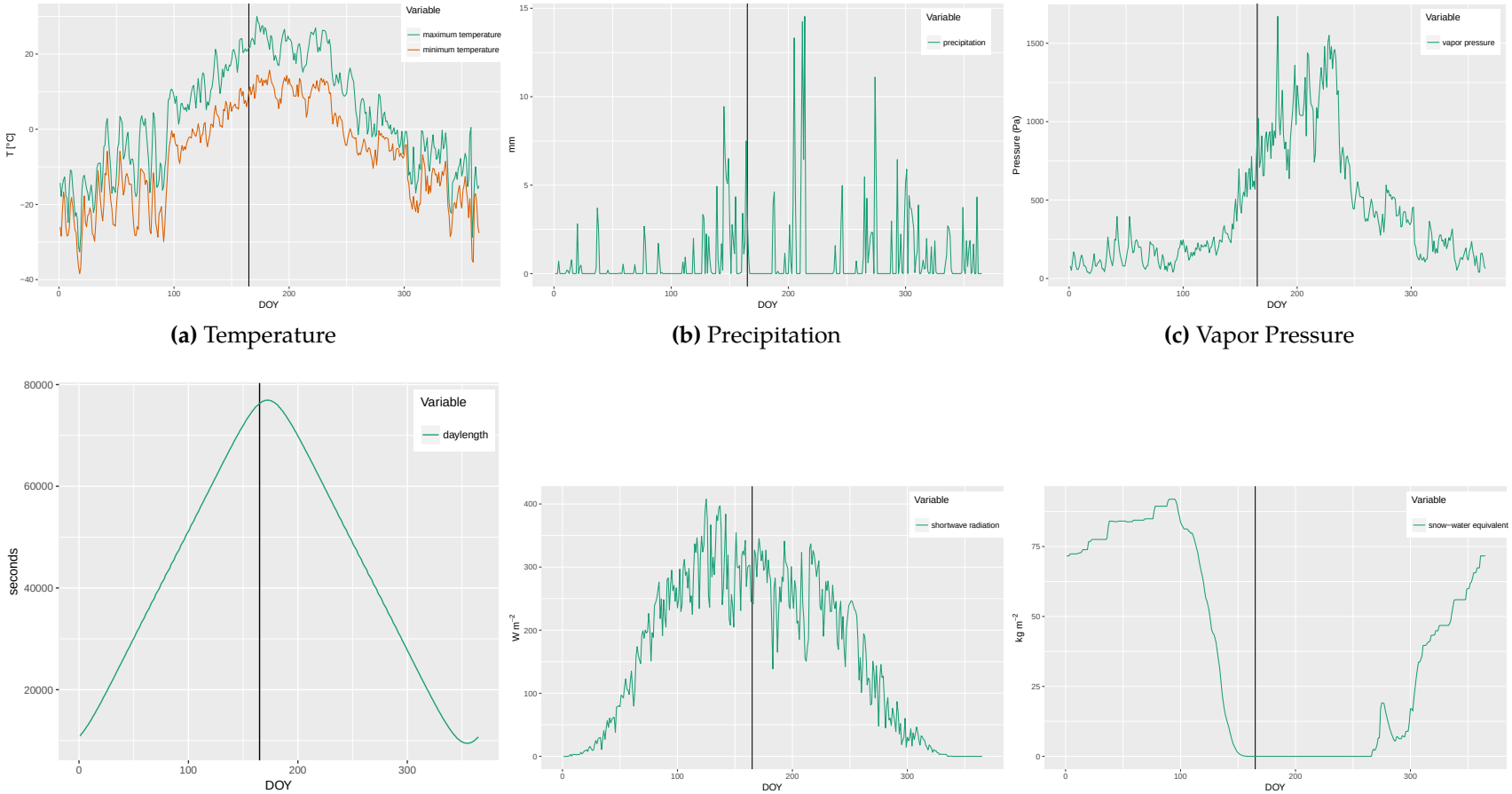


(b)

Figure 5.5: Time series of averaged MODIS surface reflectance (a) and LST (b) variables for the Boundary wildfire perimeter. The vertical line indicates the DOY (165) of the wildfire.

Time series of temperature, precipitation, vapor pressure, day length, shortwave radiation, and snow-water equivalent from Daymet variables extracted for the Boundary burn perimeter are shown in Figure 5.6. The maximum and minimum temperatures show some variation during DOY 0-100 and a increasing trend starting from DOY 100. The start of the wildfire (DOY 165) shows little variation (i.e., no abrupt changes) but the highest recorded temperatures happen right after the fire. Additionally, there is a sharp decrease in temperature around DOY 180, the cooling could be due to fire smoke affecting the temperatures. Precipitation shows relatively dry conditions from DOY 1–200, with wetter conditions happening towards the end of the year. Vapor pressure shows an increasing trend from DOY 100–250, with high variations happening after the wildfire. Vapor pressure has a sharp decrease in value around DOY 240.

Day length shows no impact from the wildfire, however the Boundary wildfire does happen around the highest value. There is a steady increase in shortwave radiation values from DOY 1–140, then there is a decrease in values up until the wildfire (DOY 165). Shortwave radiation has an abrupt decrease shortly after the wildfire (DOY 180), followed by large fluctuations and a steady decrease in values. Snow-water equivalent shows high values from DOY 1–100, followed by a sharp decrease most likely due to increase in temperatures. There is a steady increase in snow-water equivalent starting from DOY 260. The Daymet variables do no show the abrupt changes in values that we see in the MODIS variables, however certain trends may be important for wildfire mapping. For example, the trends mentioned above may be just as important as the abrupt changes in the MODIS variables.



(a) Temperature **(b)** Precipitation **(c)** Vapor Pressure

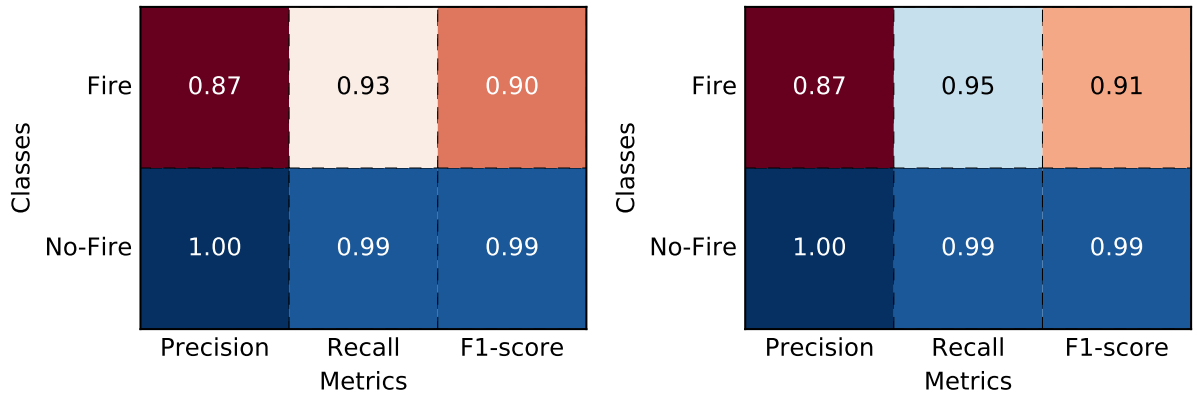
(d) Day Length **(e)** Shortwave Radiation **(f)** Snow-Water Equivalent

Figure 5.6: Daymet variables for the Boundary wildfire perimeter.

5.5.2 Estimated Wildfires

Figure 5.7 a shows the estimated wildfires using 50% of the data (Table 5.3) for the MODIS variables. The MODIS variables had high precision, recall, and F1-score values for the fire and no-fire pixels. The fire pixels achieved scores of 0.87, 0.93, and 0.90 for precision, recall, and F1-score, respectively. The no-fire pixels achieved scores of 1.00, 0.99, and 0.99 for precision, recall, and F1-score, respectively. The higher scores for the no-fire pixels could be due to the high number of training values used for modeling building (Table 5.3).

Figure 5.7 b shows the estimated wildfires using 50% of the data (Table 5.3) for the MODIS and Daymet variables. These variables had slightly higher precision, recall, and F1-score values for the fire pixels compared to using only the MODIS variables. The fire pixels achieved scores of 0.87, 0.95, and 0.91 for precision, recall, and F1-score, respectively. The no-fire pixels achieved scores of 1.00, 0.99, and 0.99 for precision, recall, and F1-score, respectively.



(a) MODIS **(b)** MODIS/Daymet

Figure 5.7: Precision, recall, and F1-score using the MODIS (a) and MODIS and Daymet (b) variables on the test dataset. The red boxes indicate the lowest scores and the blue boxes represents the highest scores. The color table is weighted to the values within each dataset.

5.5.3 Identifying Best Features

Figure 5.8 shows the feature importance for the MODIS variables. EVI showed to be the best at estimating wildfires, with a value of 0.48. SAVI was the second best variable, with a value 0.16, followed by the NIR band (0.1). LST and NDVI were close behind the NIR band with values of 0.8 and 0.75, respectively. The topographic variables (elevation and slope) showed to have the lowest feature importance.

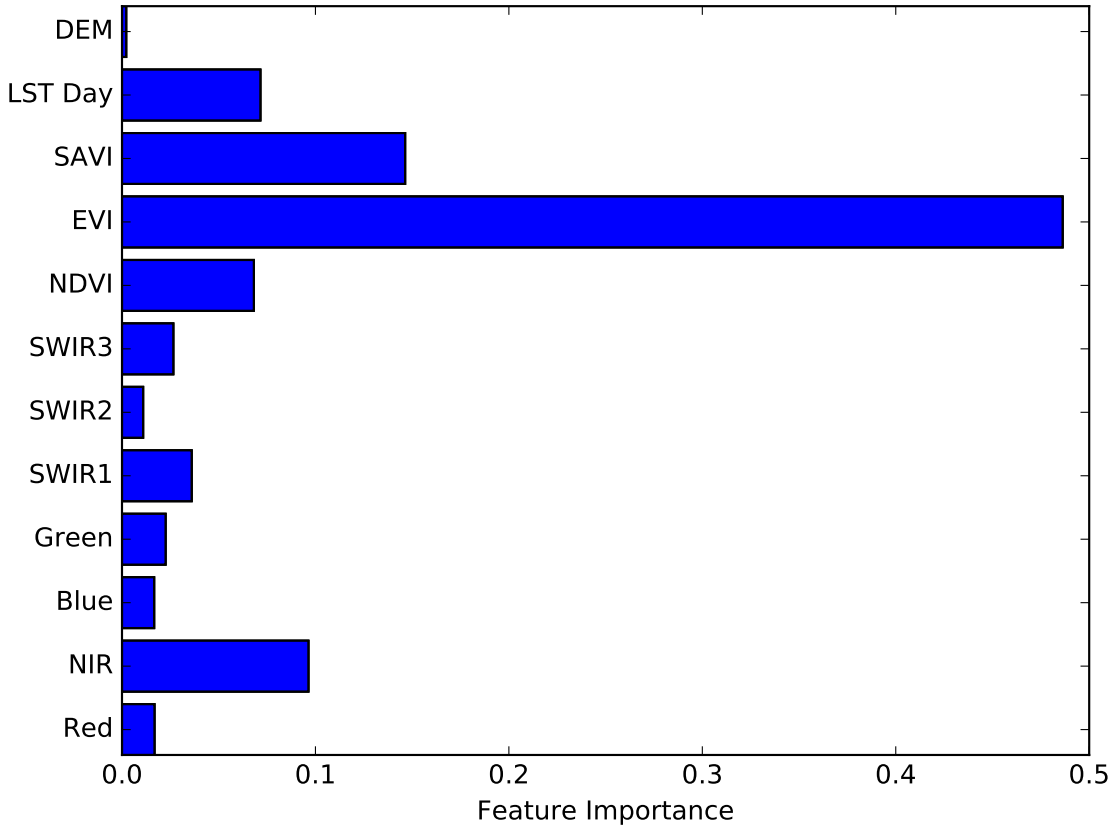


Figure 5.8: Feature importance for the MODIS variables.

Figure 5.9 shows the feature importance for the MODIS and Daymet variables. Similar to the MODIS variables, EVI showed to be the best at estimating wildfires, with a value of 0.23. Figure 5.10 shows the EVI signatures for the Boundary wildfire, showing clear value responses during and after the wildfire event. The first shortwave infrared band (SWIR 1)

showed to be the second best at estimating wildfires, with a value of 0.19. The NIR band was third best variable, with a value 0.12, followed by the SAVI index. The topographic variables (elevation and slope) showed to have the lowest feature importance. The Daymet variables showed to have little impact on the feature selection scores, but including the variables did show to increase the scores (Figure 5.7). The minimum and maximum temperatures had the highest feature importance scores (0.05 and 0.04, respectively), followed by vapor pressure (0.035), for the Daymet variables. Snow-water equivalent had the lowest feature importance score (0.01) for the Daymet variables.

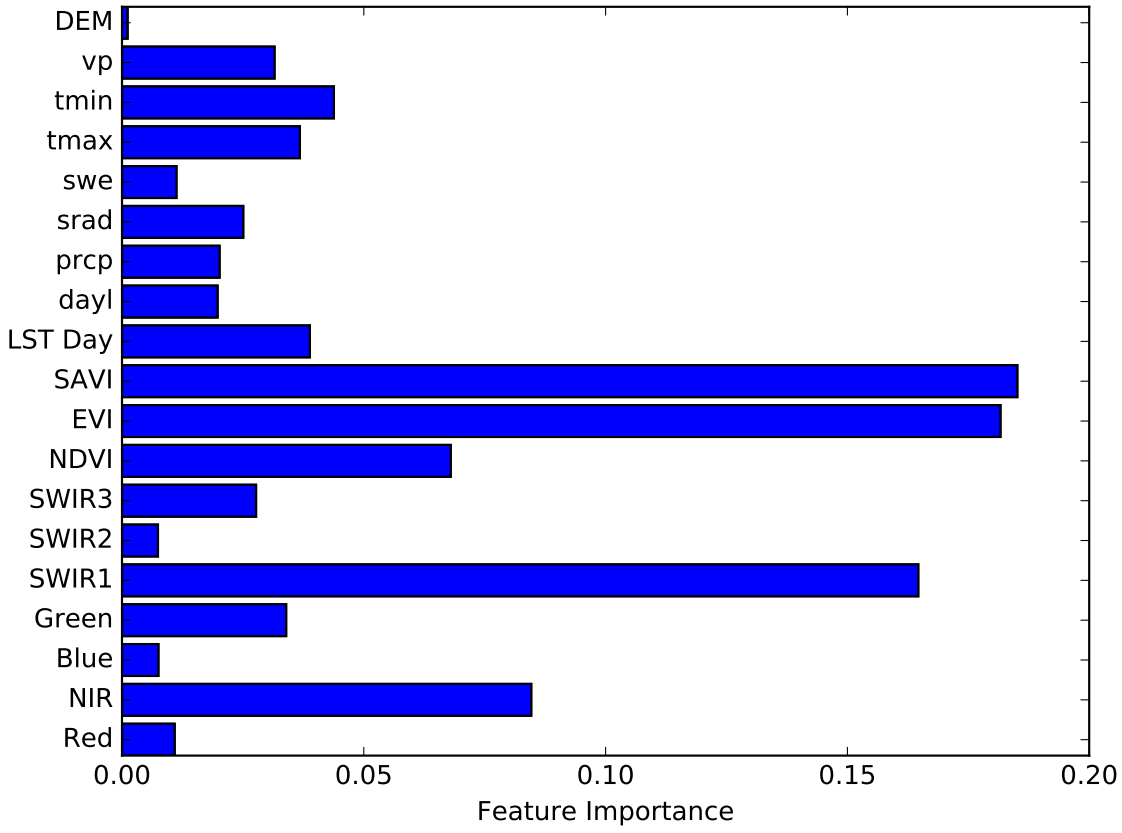


Figure 5.9: Feature importance for the MODIS and Daymet variables, with vp, tmin, tmax, swe, srad, prcp, and dayl indicating vapor pressure, minimum temperature, maximum temperature, snow-water equivalent, shortwave radiation, precipitation, and day length, respectively.

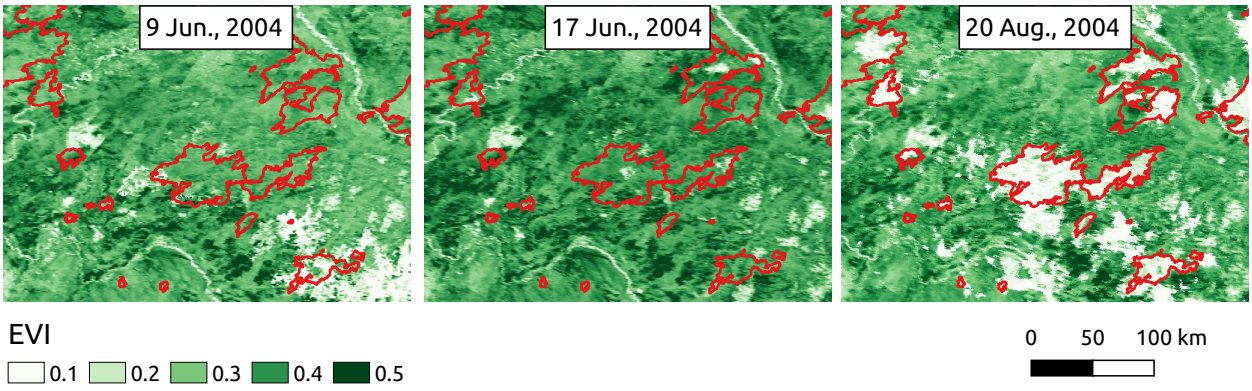


Figure 5.10: EVI responses for the Boundary wildfire. Three periods are shown: before the wildfire (9 June, 2004), 4 days after the wildfire (17 June, 2004), and 68 days after the wildfire (20 August, 2004).

5.6 Discussion

This chapter used a RF algorithm to estimate the wildfire locations based on MODIS and Daymet variables. The RF approach showed to effective at mapping wildfires for 2004 year, which is the highest recorded wildfire activity on record. This approached achieved high precision, recall, and F1-scores for the MODIS and MODIS/Daymet classifications. Including the Daymet variables did improve the scores but not significantly (Figure 5.7). This is most likely due to the sharp responses that MODIS variables show after a large wildfire.

EVI and SAVI was the most important feature based on this analysis for the MODIS and MODIS/Daymet classification, respectively. Both variables show a similar response in values when looking at the Boundary wildfire (Figure 5.5). This response shows a sharp decrease in values, followed by a gradual decrease as the year progresses. NDVI shows a similar response once the wildfire starts but there were fluctuations in high and low values as the year progressed. From this analysis, the response of EVI and SAVI after a wildfire is a significant component in algorithm development. The temperature and vapor pressure variables were the most important features for the MODIS/Daymet classification.

However, the MODIS variables clearly outweighed the Daymet variables for the feature importance calculation.

This analysis provided excellent validation scores when looking from early-April through late-October in 2004, however the metrics may have improved when looking at the entire year. Looking at the phenological signatures for the entire year might provide better insights, specifically for the Daymet variables. For example, perhaps a year that starts with low amount of precipitation and high amount of shortwave radiation may be a predecessor for wildfires. Additionally, including the previous and following year signatures may provide insights into wildfire patters. For example, NDVI signatures for the Boundary wildfire show that the yearly values after a large wildfire are much lower than the previous years.

Other types of remote sensing datasets could be useful for this type of analysis. Reiche et al. [135] used a Bayesian approach to combine SAR and optical time series for near real-time deforestation detection. That approach used the conditional probabilities for non-forest are estimated for each individual time series observation, using the corresponding sensor specific probability density functions for forest and non-forest. A similar approach could be applied for detecting disturbances over Alaska. Landsat data (15 m – 30 m resolution) incorporates over 40 years of Earth observation satellite imagery and can be used for detecting disturbances. Kennedy et al. [85] described LandTrendr (Landsat-based Detection of Trends in Disturbance and Recovery), a set of processing and analysis algorithms that captures both trends and events of disturbances. A similar approach will be looked into when assessing wildfire trends and recovery rates with Landsat data over Alaska.

The MTBS dataset provided a way to build machine learning algorithms for wildfire mapping. However, the MTBS only maps fires greater or equal to 1,000 acres [38]. This approach could identify fires around the pixel size of the datasets used for classification (500×500 m). Additionally, other datasets could be utilized for identifying disturbances, such as the Aerial Detection Survey (ADS) that reports extents on insect, disease, and other types of disturbances to forested ecosystems. Similar to the MTBS datasets, ADS

could miss areas that were not captured by the aerial flights. Making this approach using satellite remote sensing advantageous for disturbance mapping.

Accurate extents for wildfires and other disturbances are important for climate studies and ecosystem modeling. Species composition, stand age, carbon dynamics, permafrost condition, and performance are often modulated by fire in the boreal forest [186]. Climate change is also likely to influence future species dispersal, establishment, community structure, and ecosystem performance by increasing the area and frequency of fire [125, 186]. The climate projection suggests a 12.4% average increase in precipitation between the 2000–2008 average and 2040, and a 23.8% increase by 2070 [186]. Under the same scenario, mean annual temperature is expected to increase by an average of 2.2 ∘C by 2040 and 4.1 ∘C by 2070 compared to the 2000–2008 baseline [186]. Under these scenarios, the deciduous component of boreal forests will increase, leading to further carbon uptake and productivity [183]. The expected shift in fire frequency and severity could result in a novel ecosystem dominated by black spruce, aspen, and birch [7]. The increased deciduous forest cover in the future may also regionally serve as a negative feedback to a warming climate, since it has a higher albedo than conifer forests and an evaporative cooling effect [77].

5.7 Conclusions

This study produced two significant achievements. First, a data intensive RF model was robust to a wide range of input variables (combination of MODIS, Daymet, and topographic) and estimated wildfire locations with high validation statistics. Second, the RF algorithm showed that EVI, SAVI, NIR, and SWIR MODIS variables were the most significant for wildfire estimation. These variables showed large deviation in values for wildfires. Including the Daymet dataset slightly improved the validation statistics, with the temperature variables providing the best features for wildfire estimation. However, including the entire year and interannual variations related to weather conditions could lead to better wildfire mapping.

Future applications would also be facilitated by improved input data layers, such as improved weather, permafrost, and other remote sensing variables. This study advances knowledge and informs management and field studies by identifying areas at 500 m resolution that are likely to be impacted by wildfires. This information is also important to decision making related to climate implications, feedback, mitigation, and adaptation at global scales and can inform land managers and users making adaptive management decisions.

Chapter 6

Conclusion

6.1 Importance of Geospatial Analytics

The work presented here show methods for integrating remote sensing datasets at different spatial and temporal resolutions for extracting useful information from the Arctic landscape. By combining observations from LiDAR and WorldView-2 satellite imagery, I presented a method for upscaling plant functional types (PFTs) in a polygonal tundra landscape in Barrow, Alaska. The framework using k-means clustering algorithm for segregating the landscape and using the k clusters for bounding our upscaling algorithm provided a new approach in fragmented landscapes. We believe that the landscape characterization performed by k-means clustering leads to a better upscaling product when using the sampling points within each cluster. Multiple WorldView-2 images were used for testing the degree in which incorporating phenology, seasonal changes in plants. This approach increased for the validation metrics when performing multiple ground-truth campaigns.

The integration of hyper-spectral, multi-spectral, radar, and terrain datasets provided new approaches for vegetation mapping across the Seward Peninsula, Alaska. A convolutional neural network (CNN) approach was used for the integrated datasets. Two CNN approaches were developed: (1) breaking up the images into small patches (e.g., 6×6) and predict the vegetation class for entire patch and (2) semantic segmentation to predict the vegetation class for every pixel. Both architectures achieved excellent results indicating that CNNs should play a pivotal role in Arctic remote sensing applications. The fusion of hyper-spectral and high spatial resolution optical datasets performed the best, indicating that the integration of spectral and spatial sources increases the accuracies for Arctic vegetation mapping.

The fusion of the hyper-spectral, multi-spectral, radar, and terrain datasets were then applied for validating field-scale vegetation measurements. A quantitative goodness-of-fit (GOF) method was used between the reference map and classified (i.e., k-means clustering) data sources for relabeling the integrated datasets. This was done for reducing the noise in the source map and creating training datasets that were tailored to the

integrated datasets. I then applied supervised machine learning approaches (i.e., CNNs) by using the vegetation labels gathered from the GOF method. The analysis showed that the CNN models based on EO-1 Hyperion integrated with the other datasets had the best the overall scores at the field-scale level using 30 plots. The CNN models based on reference labels performed slightly better then using the labels from the GOF method. This indicated that CNN models developed on noisy datasets can still provide accurate datasets and the GOF processing step may not be needed. All classifications showed the same trends, with higher scores for alder-willow shrubs and mixed shrub-sedge tussock tundra-bog, indicating that high spatial and spectral datasets are useful for mapping these vegetation types in Arctic ecosystems.

The integration of the Moderate-Resolution Imaging Spectroradiometer (MODIS) sensor and Daymet dataset, gridded estimates of daily weather parameters, showed that certain variables may be more acceptable for wildfire mapping based on a random forest algorithm. The analysis showed that EVI, SAVI, and the shortwave infrared (SWIR) region are the most important variables for wildfire mapping across the Interior Alaska. The integration of Daymet and MODIS slightly improved the estimated wildfires but still showed that MODIS variables outperform Daymet variables. Additionally, the use of multiple seasons may lead to a better understanding of the fire regimes and what may cause a significant fire year. For example, low precipitation from the previous year may cause a large wildfire season for the nest year.

It's important to achieve a balance between the machine learning system and the task at hand. This work provides examples of characterizing Arctic landscapes using supervised and unsupervised methods. However, semi-supervised learning could provide new insights for Arctic remote sensing. Semi-supervised learning aims to improve learning accuracy when a large source of unlabeled data is available in addition to a small labeled dataset. For example, label spreading minimizes a loss function that has regularization properties, as such it is often more robust to noise. Additionally, other deep learning models could be used for analyzing the spatio-temporal trends. For example, the Long Short-Term Memory (LSTM) model can capture long-term sequences and provide new

insights into Arctic processes. It is important to find new machine learning and data mining frameworks for quantifying surface variables. Remote sensing provides a valuable tool and resource for developing such studies. These chapters lay out a framework for such development and contributes to the field of Arctic remote sensing.

6.2 Incorporation of Field Samples

This research provides model-inspired insights into optimal sampling strategies across space and through time. This is important in harsh and under-sampled environments like the Arctic. The representativeness metric employed provided a way to measure dissimilarity in pixels and provides an approach for optimal sampling design to reduce the uncertainties. The accuracy of the upscaled data were higher for areas well represented by the sampling sites and lower for areas that were under-represented. This leads to a quantitative approach for understanding ecosystem responses to climate change and informing model improvements. The same approach guided field studies for the NGEE Arctic project in the Seward Peninsula partially because current conditions on the Seward Peninsula are likely to be representative of conditions on the coastal North Slope in the future [67].

This research utilized 1 m $\times$ 1 m, 2.5 m $\times$ 2.5 m, and 5 m $\times$ 5 m field plots for algorithm development and validation. The field plot sizes were already chosen prior to algorithm development. However, the research presented here can lead to identifying the optimal plot sizes for landscape characterization. It is important to identify landscape characteristics (e.g., vegetation) for not only the entire pixel size (e.g., 5 m $\times$ 5 m) but also sub-pixel, because this often contains a mix of varying types of surface properties.

6.3 Implications for Climate Studies

Arctic landscapes are experiencing warming trends that have been accelerating. This is shown by increased temperatures, loss of summer sea ice, earlier snow melt, impacts

on ecosystems, and increased economic access [122]. At the same time, the scientific understanding on processes and feedbacks causing this rapid change in the Arctic remains a challenge. The Coupled Model Intercomparison Project (CMIP5) shows a loss of sea ice as greenhouse gas concentrations increase and a faster rate of temperature increase in the Arctic than at lower latitudes [122]. Additionally, CLM predicts that drier soil conditions will accelerate organic matter decomposition, with concomitant increases in carbon dioxide (CO_2) emissions [96]. However, soil drying strongly suppresses growth in methane (CH_4) emissions, which weakens the CLM projected GWP associated with carbon fluxes from the permafrost zone [96]. This highlights the the need for better understanding and modeling of landscape-scale changes Arctic ecosystems.

A crucial component of improving modeling and understanding of Arctic ecosystems is the development of coupled assimilation of satellite observations to ensure consistent initialization at the interface between the different sub-systems. The integration of satellite-derived observations into models can also help minimize uncertainties. The potential assimilation of remote sensing products is expected to benefit a wide range of applications important for Arctic studies, such as carbon feedbacks, climate prediction, and shifts in vegetation. The research presented here is be beneficial for future modeling studies in Arctic ecosystems, through a series of algorithms that describe surface parameters with high accuracies and identifying optimal spectral characteristics for important variables.

Bibliography

[1] Abadi, M., Barham, P., Chen, J., Chen, Z., Davis, A., Dean, J., Devin, M., Ghemawat, S., Irving, G., Isard, M., Kudlur, M., Levenberg, J., Monga, R., Moore, S., Murray, D. G., Steiner, B., Tucker, P., Vasudevan, V., Warden, P., Wicke, M., Yu, Y., and Zheng, X. (2016). Tensorflow: A system for large-scale machine learning. In *12th USENIX Symposium on Operating Systems Design and Implementation (OSDI 16)*, pages 265–283. 55, 83

[2] Anisimov, O. A., Vaughan, D. G., Callaghan, T. V., Furgal, C., Marchant, H., Prowse, T. D., Vilhjálmsson, H., and Walsh, J. E. (2007). Polar regions (Arctic and Antarctic). In Parry, M. L., Canziani, O. F., Palutikof, J. P., van der Linden, P. J., and Hanson, C. E., editors, *Climate Change 2007: Impacts, Adaptation and Vulnerability*, pages 653–685. Cambridge University Press, Cambridge. 10

[3] Atchley, A. L., Painter, S. L., Harp, D. R., Coon, E. T., Wilson, C. J., Liljedahl, A. K., and Romanovsky, V. E. (2015). Using field observations to inform thermal hydrology models of permafrost dynamics with ATS (v0.83). *Geoscientific Model Development*, 8(9):2701–2722. 11

[4] Atkinson, D. M. and Treitz, P. (2012). Arctic ecological classifications derived from vegetation community and satellite spectral data. *Remote Sensing*, 4(12):3948. 12

[5] Attarchi, S. and Gloaguen, R. (2014). Classifying Complex Mountainous Forests with L-Band SAR and Landsat Data Integration: A Comparison among Different Machine Learning Methods in the Hyrcanian Forest. *Remote Sensing*, 6(5):3624. 72

[6] Bagan, H., Kinoshita, T., and Yamagata, Y. (2012). Combination of AVNIR-2, PALSAR, and Polarimetric Parameters for Land Cover Classification. *IEEE Transactions on Geoscience and Remote Sensing*, 50(4):1318–1328. 71

[7] Barrett, K., Kasischke, E., McGuire, A., Turetsky, M., and Kane, E. (2010). Modeling fire severity in black spruce stands in the Alaskan boreal forest using spectral and non-spectral geospatial data. *Remote Sensing of Environment*, 114(7):1494 – 1503. 124

[8] Bianco, S., Cusano, C., and Schettini, R. (2017). Single and Multiple Illuminant Estimation Using Convolutional Neural Networks. *IEEE Transactions on Image Processing*, 26(9):4347–4362. 62

[9] Bieniek, P. A., Bhatt, U. S., Thoman, R. L., Angeloff, H., Partain, J., Papineau, J., Fritsch, F., Holloway, E., Walsh, J. E., Daly, C., Shulski, M., Hufford, G., Hill, D. F., Calos, S., and Gens, R. (2012). Climate Divisions for Alaska Based on Objective Methods. *Journal of Applied Meteorology and Climatology*, 51(7):1276–1289. 108

[10] Bisht, G., Huang, M., Zhou, T., Chen, X., Dai, H., Hammond, G., Riley, W., Downs, J., Liu, Y., and Zachara, J. (2017). Coupling a three-dimensional subsurface flow and transport model with a land surface model to simulate stream-aquifer-land interactions (PFLOTRAN_CLM v1.0). *Geoscientific Model Development Discussions*, 2017:1–45. 71

[11] Bockheim, J. G., Everett, L. R., Hinkel, K. M., Nelson, F. E., and Brown, J. (1999). Soil organic carbon storage and distribution in arctic tundra, Barrow, Alaska. *Soil Sci. Soc. Am. J.*, 63(4):934–940. 16

[12] Boike, J., Grau, T., Heim, B., Günther, F., Langer, M., Muster, S., Gouttevin, I., and Lange, S. (2016). Satellite-derived changes in the permafrost landscape of central Yakutia, 2000–2011: Wetting, drying, and fires. *Global and Planetary Change*, 139:116–127. 105

[13] Bond-Lamberty, B., Epron, D., Harden, J., Harmon, M. E., Hoffman, F. M., Kumar, J., McGuire, A. D., and Vargas, R. (2016). Estimating heterotrophic respiration at large scales: Challenges, approaches, and next steps. *Ecosphere*, 7(6). 72

[14] Bradley, P. S. and Fayyad, U. M. (1998). Refining initial points for k-means clustering. In *ICML '98: Proceedings of the Fifteenth International Conference on Machine Learning*, pages 91–99, San Francisco, CA, USA. Morgan Kaufmann Publishers Inc. 21, 81

[15] Bratsch, S. N., Epstein, H. E., Buchhorn, M., and Walker, D. A. (2016). Differentiating among Four Arctic Tundra Plant Communities at Ivotuk, Alaska Using Field Spectroscopy. *Remote Sensing*, 8(51). 47, 72

[16] Breiman, L. (2001). Random Forests. *Machine Learning*, 45(1):5–32. 113

[17] Brown, J. (1967). Tundra soils formed over ice wedges, northern Alaska. *Soil Science Society of America*, 31(5):686–691. 16

[18] Byer, S. and Jin, Y. (2017). Detecting Drought-Induced Tree Mortality in Sierra Nevada Forests with Time Series of Satellite Data. *Remote Sensing*, 9(9). 113

[19] Carroll, M. L., Townshend, J. R. G., DiMiceli, C. M., Loboda, T., and Sohlberg, R. A. (2011). Shrinking lakes of the arctic: Spatial relationships and trajectory of change. *Geophysical Research Letters*, 38(20):n/a–n/a. L20406. 105

[20] Chapin, F. S., Bret-Harte, M. S., Hobbie, S. E., and Zhong, H. (1996). Plant functional types as predictors of transient responses of arctic vegetation to global change. *Journal of Vegetation Science*, 7(3):347–358. 11, 17, 42

[21] Chapin, F. S., McGuire, A. D., Ruess, R. W., Hollingsworth, T. N., Mack, M. C., Johnstone, J. F., Kasischke, E. S., Euskirchen, E. S., Jones, J. B., Jorgenson, M. T., Kielland, K., Kofinas, G. P., Turetsky, M. R., Yarie, J., Lloyd, A. H., and Taylor, D. L. (2010). Resilience of Alaska's boreal forest to climatic change. *Can. J. Forest Res.*, 40(7):1360–1370. 11

[22] Chapin, F. S., Sturm, M., Serreze, M. C., McFadden, J. P., Key, J. R., Lloyd, A. H., McGuire, A. D., Rupp, T. S., Lynch, A. H., Schimel, J. P., Beringer, J., Chapman, W. L., Epstein, H. E., Euskirchen, E. S., Hinzman, L. D., Jia, G., Ping, C.-L., Tape, K. D., Thompson, C. D. C., Walker, D. A., and Welker, J. M. (2005). Role of land-surface changes in Arctic summer warming. *Science*, 310(5748):657–660. 2, 3

[23] Chen, Y., Lin, Z., Zhao, X., Wang, G., and Gu, Y. (2014). Deep Learning-Based Classification of Hyperspectral Data. *IEEE Journal of Selected Topics in Applied Earth Observations and Remote Sensing*, 7(6):2094–2107. 55

[24] Chollet, F. et al. (2015). Keras. https://github.com/fchollet/keras. 55, 83

[25] Clewley, D., Whitcomb, J., Moghaddam, M., McDonald, K., Chapman, B., and Bunting, P. (2015). Evaluation of ALOS PALSAR Data for High-Resolution Mapping of Vegetated Wetlands in Alaska. *Remote Sensing*, 7(6):7272. 4, 71, 97

[26] Cremon, E. H., de Fátima Rossetti, D., and Zani, H. (2014). Classification of Vegetation over a Residual Megafan Landform in the Amazonian Lowland Based on Optical and SAR Imagery. *Remote Sensing*, 6(11):10931. 71, 72, 79

[27] Dabrowska-Zielinska, K., Budzynska, M., Tomaszewska, M., Bartold, M., Gatkowska, M., Malek, I., Turlej, K., and Napiorkowska, M. (2014). Monitoring Wetlands Ecosystems Using ALOS PALSAR (L-Band, HV) Supplemented by Optical Data: A Case Study of Biebrza Wetlands in Northeast Poland. *Remote Sensing*, 6(2):1605. 72

[28] Dalmayne, J., Möckel, T., Prentice, H., Schmid, B., and Hall, K. (2013). Assessment of fine-scale plant species beta diversity using WorldView-2 satellite spectral dissimilarity. *Ecological Informatics*, 18(0):1–9. 12, 19

[29] Davidson, S. J., Santos, M. J., Sloan, V. L., Watts, J. D., Phoenix, G. K., Oechel, W. C., and Zona, D. (2016). Mapping Arctic Tundra Vegetation Communities Using Field Spectroscopy and Multispectral Satellite Data in North Alaska, USA. *Remote Sensing*, 8(12). 47, 72

[30] Defibaugh y Chávez, J. and Tullis, J. A. (2013). Deciduous forest structure estimated with lidar-optimized spectral remote sensing. *Remote Sensing*, 5(1):155–182. 72

[31] Dennis, J. G., Tieszen, L. L., and Vetter, M. A. (1978). Seasonal dynamics of above- and belowground production of vascular plants at barrow, alaska. In *Vegetation and*

Production Ecology of an Alaskan Arctic Tundra, volume 29 of *Ecological Studies*, pages 113–140. Springer New York. 26

[32] DOE (2012). Next-Generation Ecosystem Experiments (NGEE Arctic). 4

[33] Donald A. Walker, M. D. W. (1991). History and Pattern of Disturbance in Alaskan Arctic Terrestrial Ecosystems: A Hierarchical Approach to Analysing Landscape Change. *Journal of Applied Ecology*, 28(1):244–276. 105

[34] Dong, C., Loy, C. C., He, K., and Tang, X. (2016). Image Super-Resolution Using Deep Convolutional Networks. *IEEE Transactions on Pattern Analysis and Machine Intelligence*, 38(2):295–307. 66

[35] Duguay, Y., Bernier, M., Lévesque, E., and Domine, F. (2016). Land Cover Classification in SubArctic Regions Using Fully Polarimetric RADARSAT-2 Data. *Remote Sensing*, 8(9). 60

[36] Duguay, Y., Bernier, M., Lévesque, E., and Tremblay, B. (2014). Monitoring of subarctic shrub vegetation characteristics using TerraSAR-X and RADARSAT-2 data. In *2014 IEEE Geoscience and Remote Sensing Symposium*, pages 1194–1197. 97

[37] Duguay, Y., Bernier, M., Lévesque, E., and Tremblay, B. (2015). Potential of C and X Band SAR for Shrub Growth Monitoring in Sub-Arctic Environments. *Remote Sensing*, 7(7):9410. 97

[38] Eidenshink, J., Schwind, B., Brewer, K., Zhu, Z.-L., and Quayle, B. (2007). A project for monitoring trends in burn severity. *Fire Ecology*, 3(1):3–21. 105, 123

[39] Euskirchen, E. S., Edgar, C. W., Turetsky, M. R., Waldrop, M. P., and Harden, J. W. (2014). Differential response of carbon fluxes to climate in three peatland ecosystems that vary in the presence and stability of permafrost. *Journal of Geophysical Research: Biogeosciences*, 119(8):1576–1595. 10

[40] Folkman, M. A., Pearlman, J., Liao, L. B., and Jarecke, P. J. (2001). EO-1/Hyperion hyperspectral imager design, development, characterization, and calibration. volume 4151, pages 40–51. 72

[41] Forkel, M., Carvalhais, N., Verbesselt, J., Mahecha, M. D., Neigh, C. S., and Reichstein, M. (2013). Trend Change Detection in NDVI Time Series: Effects of Inter-Annual Variability and Methodology. *Remote Sensing*, 5(5):2113. 4

[42] Forkuor, G., Conrad, C., Thiel, M., Zoungrana, B. J.-B., and Tondoh, J. E. (2017). Multiscale Remote Sensing to Map the Spatial Distribution and Extent of Cropland in the Sudanian Savanna of West Africa. *Remote Sensing*, 9. 113

[43] Fraser, R. H., Olthof, I., Kokelj, S. V., Lantz, T. C., Lacelle, D., Brooker, A., Wolfe, S., and Schwarz, S. (2014). Detecting Landscape Changes in High Latitude Environments Using Landsat Trend Analysis: 1. Visualization. *Remote Sensing*, 6(11):11533. 71, 104, 105

[44] Fu, G., Liu, C., Zhou, R., Sun, T., and Zhang, Q. (2017). Classification for High Resolution Remote Sensing Imagery Using a Fully Convolutional Network. *Remote Sensing*, 9(5). 62, 99

[45] Gangodagamage, C., Rowland, J. C., Hubbard, S. S., Brumby, S. P., Liljedahl, A. K., Wainwright, H., Wilson, C. J., Altmann, G. L., Dafflon, B., Peterson, J., Ulrich, C., Tweedie, C. E., and Wullschleger, S. D. (2014). Extrapolating active layer thickness measurements across Arctic polygonal terrain using LiDAR and NDVI data sets. *Water Resour. Res.*, 50(8):6339–6357. 12, 41

[46] Ghasrodashti, E. K., Karami, A., Heylen, R., and Scheunders, P. (2017). Spatial Resolution Enhancement of Hyperspectral Images Using Spectral Unmixing and Bayesian Sparse Representation. *Remote Sensing*, 9(6). 66

[47] Goetz, S. J., Fiske, G. J., and Bunn, A. G. (2006). Using satellite time-series data sets to analyze fire disturbance and forest recovery across Canada. *Remote Sensing of Environment*, 101(3):352 – 365. 105

[48] Gooseff, M. N., Balser, A., Bowden, W. B., and Jones, J. B. (2009). Effects of hillslope thermokarst in northern alaska. *Eos, Transactions American Geophysical Union*, 90(4):29–30. 105

[49] Gorelick, N., Hancher, M., Dixon, M., Ilyushchenko, S., Thau, D., and Moore, R. (2017). Google Earth Engine: Planetary-scale geospatial analysis for everyone. *Remote Sensing of Environment*. 106

[50] Goswami, S., Gamon, J. A., and Tweedie, C. E. (2011). Surface hydrology of an arctic ecosystem: Multiscale analysis of a flooding and draining experiment using spectral reflectance. *Journal of Geophysical Research: Biogeosciences*, 116(G4):n/a–n/a. G00I07. 160

[51] Greaves, H. E., Vierling, L. A., Eitel, J. U., Boelman, N. T., Magney, T. S., Prager, C. M., and Griffin, K. L. (2015). Estimating aboveground biomass and leaf area of low-stature Arctic shrubs with terrestrial LiDAR. *Remote Sensing of Environment*, 164:26 – 35. 70

[Grosse et al.] Grosse, G., Goetz, S., McGuire, A. D., Romanovsky, V. E., and Schuur, E. A. G. Changing permafrost in a warming world and feedbacks to the Earth system, journal=Environmental Research Letters, volume=11, number=4, pages=040201, url=http://stacks.iop.org/1748-9326/11/i=4/a=040201, year=2016, abstract=The permafrost component of the cryosphere is changing dramatically, but the permafrost region is not well monitored and the consequences of change are not well understood. Changing permafrost interacts with ecosystems and climate on various spatial and temporal scales. The feedbacks resulting from these interactions range from local impacts on topography, hydrology, and biology to complex influences on global scale biogeochemical cycling. This review contributes to this focus issue by synthesizing its 28 multidisciplinary studies which provide field evidence, remote sensing observations,

and modeling results on various scales. We synthesize study results from a diverse range of permafrost landscapes and ecosystems by reporting key observations and modeling outcomes for permafrost thaw dynamics, identifying feedbacks between permafrost and ecosystem processes, and highlighting biogeochemical feedbacks from permafrost thaw. We complete our synthesis by discussing the progress made, stressing remaining challenges and knowledge gaps, and providing an outlook on future needs and research opportunities in the study of permafrost–ecosystem–climate interactions. 2

[53] Hachem, S., Duguay, C. R., and Allard, M. (2012). Comparison of MODIS-derived land surface temperatures with ground surface and air temperature measurements in continuous permafrost terrain. *The Cryosphere*, 6(1):51–69. 4

[54] Hansen, M. C., Potapov, P. V., Moore, R., Hancher, M., Turubanova, S. A., Tyukavina, A., Thau, D., Stehman, S. V., Goetz, S. J., Loveland, T. R., Kommareddy, A., Egorov, A., Chini, L., Justice, C. O., and Townshend, J. R. G. (2013). High-resolution global maps of 21st-century forest cover change. *Science*, 342(6160):850–853. 107

[55] Hargrove, W. W., Hoffman, F. M., and Hessburg, P. F. (2006). Mapcurves: A quantitative method for comparing categorical maps. *J. Geograph. Syst.*, 8(2):187–208. 53, 72, 82, 88

[56] Hargrove, W. W., Hoffman, F. M., and Law, B. E. (2003). New analysis reveals representativeness of the AmeriFlux Network. *Eos Trans. AGU*, 84(48):529, 535. 23, 39

[57] Hargrove, W. W., Spruce, J. P., Gasser, G. E., and Hoffman, F. M. (2009). Toward a national early warning system for forest disturbances using remotely sensed phenology. *Photogramm. Eng. Rem. Sens.*, 75(10):1150–1156. 106

[58] Hariharan, B., Arbeláez, P. A., Girshick, R. B., and Malik, J. (2014). Hypercolumns for Object Segmentation and Fine-grained Localization. *CoRR*, abs/1411.5752. 56

[59] Hartigan, J. A. (1975). *Clustering Algorithms*. John Wiley & Sons. 21, 53, 81

[60] Higuera, P., Peters, M., Brubaker, L., and Gavin, D. (2008). Frequent fires in ancient shrub tundra: implications of paleorecords for arctic environmental change. *PLoS ONE*, 3(3):e0001744. 70

[61] Hinkel, K. M. and Nelson, F. E. (2000). Summer differences among Arctic ecosystems in regional climate forcing. *Journal of Climate*, 13(12):2002–2010. 98

[62] Hinzman, L., Bettez, N., Bolton, W., Chapin, F., Dyurgerov, M., Fastie, C., Griffith, B., Hollister, R., Hope, A., Huntington, H., Jensen, A., Jia, G., Jorgenson, T., Kane, D., Klein, D., Kofinas, G., Lynch, A., Lloyd, A., McGuire, A., Nelson, F., Oechel, W., Osterkamp, T., Racine, C., Romanovsky, V., Stone, R., Stow, D., Sturm, M., Tweedie, C., Vourlitis, G., Walker, M., Walker, D., Webber, P., Welker, J., Winker, K., and Yoshikawa, j. (2005). Evidence and implications of recent climate change in Northern Alaska and other Arctic regions. *Clim. Change*, 72(3):251–298. 46, 70

[63] Hinzman, L., Deal, C. J., McGuire, A. D., Mernild, S. H., Polyakov, I. V., and Walsh, J. E. (2013). Trajectory of the Arctic as an integrated system. *Ecol. Appl.*, 23(8):1837–1868. 10

[64] Hinzman, L. D., Kane, D. L., Yoshikawa, K., Carr, A., Bolton, W. R., and Fraver, M. (2003). Hydrological variations among watersheds with varying degrees of permafrost. In *Proceedings of the 8th International Conference on Permafrost*, pages 407–411. A. A. Balkema. 49, 74

[65] Hoffman, F. M. and Hargrove, W. W. (1999). Multivariate geographic clustering using a Beowulf-style parallel computer. In Arabnia, H. R., editor, *Proceedings of the International Conference on Parallel and Distributed Processing Techniques and Applications (PDPTA '99)*, volume III, pages 1292–1298. CSREA Press. 53

[66] Hoffman, F. M., Hargrove, W. W., Mills, R. T., Mahajan, S., Erickson, D. J., and Oglesby, R. J. (2008). Multivariate Spatio-Temporal Clustering (MSTC) as a data

mining tool for environmental applications. In Sànchez-Marrè, M., Béjar, J., Comas, J., Rizzoli, A. E., and Guariso, G., editors, *Proceedings of the iEMSs Fourth Biennial Meeting: International Congress on Environmental Modelling and Software Society (iEMSs 2008)*, pages 1774–1781. 21, 81

[67] Hoffman, F. M., Kumar, J., Mills, R. T., and Hargrove, W. W. (2013). Representativeness-based sampling network design for the State of Alaska. *Landscape Ecol.*, 28(8):1567–1586. 5, 13, 23, 39, 41, 47, 74, 105, 129

[68] Hu, F. S., Higuera, P. E., Walsh, J. E., Chapman, W. L., Duffy, P. A., Brubaker, L. B., and Chipman, M. L. (2010). Tundra burning in Alaska: Linkages to climatic change and sea ice retreat. *Journal of Geophysical Research: Biogeosciences*, 115(G4):n/a–n/a. G04002. 105

[69] Hubbard, S., Gangodagamage, C., Dafflon, B., Wainwright, H., Peterson, J., Gusmeroli, A., Ulrich, C., Wu, Y., Wilson, C., Rowland, J., Tweedie, C., and Wullschleger, S. (2013). Quantifying and relating land-surface and subsurface variability in permafrost environments using LiDAR and surface geophysical datasets. *Hydrogeology Journal*, 21(1):149–169. 16

[70] Huemmrich, K., Gamon, J., Tweedie, C., Campbell, P., Landis, D., and Middleton, M. (2013). Arctic tundra vegetation functional types based on photosynthetic physiology and optical properties. *Selected Topics in Applied Earth Observations and Remote Sensing, IEEE Journal of*, 6(2):265–275. 11, 12

[71] Huemmrich, K., Gamon, J., Tweedie, C., Oberbauer, S., Kinoshita, G., Houston, S., Kuchy, A., Hollister, R., Kwon, H., Mano, M., Harazono, Y., Webber, P., and Oechel, W. (2010). Remote sensing of tundra gross ecosystem productivity and light use efficiency under varying temperature and moisture conditions. *Remote Sensing of Environment*, 114(3):481 – 489. 40

[72] Hunt, S., Yu, Z., and Jones, M. (2013). Lateglacial and Holocene climate, disturbance and permafrost peatland dynamics on the Seward Peninsula, western Alaska. *Quaternary Science Reviews*, 63:42 – 58. 48, 74

[73] IPCC (2013). Summary for Policymakers. In [159]. 2, 10

[74] Iversen, C. M., Sloan, V. L., Sullivan, P. F., Euskirchen, E. S., McGuire, A. D., Norby, R. J., Walker, A. P., Warren, J. M., and Wullschleger, S. D. (2015). The unseen iceberg: plant roots in arctic tundra. *New Phytol.*, 205(1):34–58. 42

[75] Iwata, H., Ueyama, M., Harazono, Y., Tsuyuzaki, S., Kondo, M., and Uchida, M. (2011). Quick Recovery of Carbon Dioxide Exchanges in a Burned Black Spruce Forest in Interior Alaska. *SOLA*, 7:105–108. 105

[76] Jenkins, L. K., Bourgeau-Chavez, L. L., French, N. H. F., Loboda, T. V., and Thelen, B. J. (2014). Development of Methods for Detection and Monitoring of Fire Disturbance in the Alaskan Tundra Using a Two-Decade Long Record of Synthetic Aperture Radar Satellite Images. *Remote Sensing*, 6(7):6347. 4, 105

[77] Jin, Y., Randerson, J. T., Goulden, M. L., and Goetz, S. J. (2012). Post-fire changes in net shortwave radiation along a latitudinal gradient in boreal North America. *Geophysical Research Letters*, 39(13):n/a–n/a. L13403. 124

[78] Jones, B. M., Breen, A. L., Gaglioti, B. V., Mann, D. H., Rocha, A. V., Grosse, G., Arp, C. D., Kunz, M. L., and Walker, D. A. (2013). Identification of unrecognized tundra fire events on the north slope of Alaska. *Journal of Geophysical Research: Biogeosciences*, 118(3):1334–1344. 2013JG002316. 105

[79] Jorgenson, M. T., Shur, Y. L., and Pullman, E. R. (2006). Abrupt increase in permafrost degradation in Arctic Alaska. *Geophys. Res. Lett.*, 33(Issue 2):L02503. 2, 10

[80] Justice, C., Giglio, L., Korontzi, S., Owens, J., Morisette, J., Roy, D., Descloitres, J., Alleaume, S., Petitcolin, F., and Kaufman, Y. (2002). The MODIS fire products.

Remote Sensing of Environment, 83(1–2):244 – 262. The Moderate Resolution Imaging Spectroradiometer (MODIS): a new generation of Land Surface Monitoring. 4

[81] Karna, Y. K., Hussin, Y. A., Gilani, H., Bronsveld, M., Murthy, M., Qamer, F. M., Karky, B. S., Bhattarai, T., Aigong, X., and Baniya, C. B. (2015). Integration of WorldView-2 and airborne LiDAR data for tree species level carbon stock mapping in Kayar Khola watershed, Nepal. *International Journal of Applied Earth Observation and Geoinformation*, 38:280 – 291. 12

[82] Kasischke, E., L.Verbyla, D., Rupp, T., McGuire, A., Murphy, K., Jandt, R., Barnes, J., Hoy, E., Duffy, P., Calef, M., and Turetsky, M. (2010). Alaska's changing fire regime – implications for the vulnerability of its boreal forests. *Canadian Journal of Forest Research*, 40(7):1313–1324. 105

[83] Kasischke, E. S. and Turetsky, M. R. (2006). Recent changes in the fire regime across the north american boreal region—spatial and temporal patterns of burning across canada and alaska. *Geophysical Research Letters*, 33(9):n/a–n/a. L09703. 4, 105

[84] Kennedy, R. E. (2012). New views on changing arctic vegetation. *Environmental Research Letters*, 7(1):011001. 71

[85] Kennedy, R. E., Yang, Z., and Cohen, W. B. (2010). Detecting trends in forest disturbance and recovery using yearly landsat time series: 1. landtrendr — temporal segmentation algorithms. *Remote Sensing of Environment*, 114(12):2897 – 2910. 123

[86] Koven, C. D., Schuur, E. A. G., Schädel, C., Bohn, T. J., Burke, E. J., Chen, G., Chen, X., Ciais, P., Grosse, G., Harden, J. W., Hayes, D. J., Hugelius, G., Jafarov, E. E., Krinner, G., Kuhry, P., Lawrence, D. M., MacDougall, A. H., Marchenko, S. S., McGuire, A. D., Natali, S. M., Nicolsky, D. J., Olefeldt, D., Peng, S., Romanovsky, V. E., Schaefer, K. M., Strauss, J., Treat, C. C., and Turetsky, M. (2015). A simplified, data-constrained approach to estimate the permafrost carbon–climate feedback. *Philosophical Transactions of the Royal Society of London A: Mathematical, Physical and Engineering Sciences*, 373(2054). 2

[87] Krehbiel, C. and Henebry, G. M. (2016). A Comparison of Multiple Datasets for Monitoring Thermal Time in Urban Areas over the U.S. Upper Midwest. *Remote Sensing*, 8(4). 106

[88] Krizhevsky, A., Sutskever, I., and Hinton, G. E. (2012). ImageNet Classification with Deep Convolutional Neural Networks. In Pereira, F., Burges, C. J. C., Bottou, L., and Weinberger, K. Q., editors, *Advances in Neural Information Processing Systems 25*, pages 1097–1105. Curran Associates, Inc. 55, 56, 83

[89] Kumar, J., Collier, N., Bishht, G., Mills, R. T., Thornton, P. E., Iversen, C. M., and Romanovsky, V. (2016). Modeling the spatio-temporal variablilty in subsurface thermal regimes across a low-relief polygonal tundra landscape. *The Cryoshpere Discussions*, 2016(9):1–32. 11, 46, 71

[90] Kumar, J., Mills, R. T., Hoffman, F. M., and Hargrove, W. W. (2011). Parallel k-means clustering for quantitative ecoregion delineation using large data sets. In Sato, M., Matsuoka, S., Sloot, P. M., van Albada, G. D., and Dongarra, J., editors, *Proceedings of the International Conference on Computational Science (ICCS 2011)*, volume 4 of *Procedia Comput. Sci.*, pages 1602–1611, Amsterdam. Elsevier. 21, 39, 81

[91] Kumar, J., Weiner, J., Hargrove, W. W., Norman, S. P., Hoffman, F. M., and Newcomb, D. (2015). Characterization and classification of vegetation canopy structure and distribution within the Great Smoky Mountains National Park using LiDAR. In Cui, P., Dy, J., Aggarwal, C., Zhou, Z.-H., Tuzhilin, A., Xiong, H., and Wu, X., editors, *Proceedings of the 15th IEEE International Conference on Data Mining Workshops (ICDMW 2015)*, pages 1478–1485. Institute of Electrical and Electronics Engineers (IEEE), Conference Publishing Services (CPS). 53

[92] Langford, Z. L., Kumar, J., and Hoffman, F. M. (2017). Convolutional Neural Network Approach for Mapping Arctic Vegetation using Multi-Sensor Remote Sensing. In *International Conference on Data Mining Workshops (ICDM 2017)*. Institute of Electrical and Electronics Engineers (IEEE). 83

[93] Langford, Z. L., Kumar, J., Hoffman, F. M., Norby, R. J., Wullschleger, S. D., Sloan, V. L., and Iversen, C. M. (2016). Mapping Arctic Plant Functional Type Distributions in the Barrow Environmental Observatory Using WorldView-2 and LiDAR Datasets. *Remote Sensing*, 8(9):733. 46, 71, 98

[94] Lara, M. J., Genet, H., McGuire, A. D., Euskirchen, E. S., Zhang, Y., Brown, D. R. N., Jorgenson, M. T., Romanovsky, V., Breen, A., and Bolton, W. R. (2016). Thermokarst rates intensify due to climate change and forest fragmentation in an alaskan boreal forest lowland. *Global Change Biology*, 22(2):816–829. 105

[95] Lawrence, D. M., Koven, C. D., Swenson, S. C., Riley, W. J., and Slater, A. G. (2015a). Permafrost thaw and resulting soil moisture changes regulate projected high-latitude co 2 and ch 4 emissions. *Environmental Research Letters*, 10(9):094011. 104

[96] Lawrence, D. M., Koven, C. D., Swenson, S. C., Riley, W. J., and Slater, A. G. (2015b). Permafrost thaw and resulting soil moisture changes regulate projected high-latitude CO_2 and CH_4 emissions. *Environmental Research Letters*, 10(9):094011. 2, 130

[97] Lawrence, D. M. and Swenson, S. C. (2011). Permafrost response to increasing Arctic shrub abundance depends on the relative influence of shrubs on local soil cooling versus large-scale climate warming. *Environmental Research Letters*, 6(4):045504. 70

[98] Lee, J.-S. and Pottier, E. (2009). *Polarimetric Radar Imaging: From Basics to Applications*. CRC Press, Taylor and Francis. 52, 79

[99] Leverington, D. W. and Schindler, M. (2016). Detection and Mapping of Black Rock Coatings Using Hyperion Images: Sudbury, Ontario, Canada. *Remote Sensing*, 8(4). 72

[100] Li, J., Cheng, K., Wang, S., Morstatter, F., Robert, T., Tang, J., and Liu, H. (2016). Feature selection: A data perspective. *arXiv:1601.07996*. 107

[101] Li, J. and Liu, H. (2017). Challenges of feature selection for big data analytics. *IEEE Intelligent Systems*, 32(2):9–15. 107

[102] Liljedahl, A. K., Boike, J., Daanen, R. P., Fedorov, A. N., Frost, G. V., Grosse, G., Hinzman, L. D., Iijma, Y., Jorgenson, J. C., Matveyeva, N., Necsoiu, M., Raynolds, M. K., Romanovsky, V. E., Schulla, J., Tape, K. D., Walker, D. A., Wilson, C. J., Yabuki, H., and Zona, D. (2016). Pan-arctic ice-wedge degradation in warming permafrost and its influence on tundra hydrology. *Nature Geoscience*. 105

[103] Liljedahl, A. K. and Hinzman, L. D. and Harazono, Y. and Zona, D. and Tweedie, C. E. and Hollister, R. D. and Engstrom, R. and Oechel, W. C. (2011). Nonlinear controls on evapotranspiration in arctic coastal wetlands. *Biogeosciences*, 8(11):3375–3389. 15

[104] Lindsay, C., Zhu, J., Miller, A. E., Kirchner, P., and Wilson, T. L. (2015). Deriving Snow Cover Metrics for Alaska from MODIS. *Remote Sensing*, 7(10):12961. 71

[105] Lobell, D. B., Thau, D., Seifert, C., Engle, E., and Little, B. (2015). A scalable satellite-based crop yield mapper. *Remote Sensing of Environment*, 164:324 – 333. 106, 107

[106] Lu, X., Lin, Z., Shen, X., Mech, R., and Wang, J. Z. (2015). Deep Multi-patch Aggregation Network for Image Style, Aesthetics, and Quality Estimation. In *2015 IEEE International Conference on Computer Vision (ICCV)*, pages 990–998. 67, 111, 112

[107] Mahlstein, I. and Knutti, R. (2012). September Arctic sea ice predicted to disappear near 2°C global warming above present. *Journal of Geophysical Research: Atmospheres*, 117(D6):n/a–n/a. D06104. 2, 46, 70

[108] Marland, G., Boden, T., and Andres, R. (2008). Global, Regional, and National Fossil Fuel CO_2 Emissions. Carbon Dioxide Information Analysis Center, Oak Ridge National Laboratory, U.S. Department of Energy, Oak Ridge, Tenn., USA. In Trends: A Compendium of Data on Global Change. 2

[109] McGuire, A. D., Koven, C., Lawrence, D. M., Clein, J. S., Xia, J., Beer, C., Burke, E., Chen, G., Chen, X., Delire, C., Jafarov, E., MacDougall, A. H., Marchenko, S., Nicolsky, D., Peng, S., Rinke, A., Saito, K., Zhang, W., Alkama, R., Bohn, T. J., Ciais, P., Decharme, B., Ekici, A., Gouttevin, I., Hajima, T., Hayes, D. J., Ji, D., Krinner, G., Lettenmaier, D. P.,

Luo, Y., Miller, P. A., Moore, J. C., Romanovsky, V., Schädel, C., Schaefer, K., Schuur, E. A., Smith, B., Sueyoshi, T., and Zhuang, Q. (2016). Variability in the sensitivity among model simulations of permafrost and carbon dynamics in the permafrost region between 1960 and 2009. *Global Biogeochemical Cycles*, 30(7):1015–1037. 2016GB005405. 70

[110] Milewski, R., Chabrillat, S., and Behling, R. (2017). Analyses of Recent Sediment Surface Dynamic of a Namibian Kalahari Salt Pan Based on Multitemporal Landsat and Hyperspectral Hyperion Data. *Remote Sensing*, 9(2). 72

[111] Millard, K. and Richardson, M. (2015). On the Importance of Training Data Sample Selection in Random Forest Image Classification: A Case Study in Peatland Ecosystem Mapping. *Remote Sensing*, 7(7):8489–8515. 107

[112] Miller, P. A. and Smith, B. (2012). Modelling Tundra Vegetation Response to Recent Arctic Warming. *AMBIO*, 41(3):281–291. 2, 46, 70

[113] Mills, R. T., Hoffman, F. M., Kumar, J., and Hargrove, W. W. (2011). Cluster analysis-based approaches for geospatiotemporal data mining of massive data sets for identification of forest threats. In Sato, M., Matsuoka, S., Sloot, P. M., van Albada, G. D., and Dongarra, J., editors, *Proceedings of the International Conference on Computational Science (ICCS 2011)*, volume 4 of *Procedia Comput. Sci.*, pages 1612–1621, Amsterdam. Elsevier. 106

[114] Mills, R. T., Kumar, J., Hoffman, F. M., Hargrove, W. W., Spruce, J. P., and Norman, S. P. (2013). Identification and visualization of dominant patterns and anomalies in remotely sensed vegetation phenology using a parallel tool for principal components analysis. *Procedia Comput. Sci.*, 18(0):2396–2405. 13

[115] Moreno, A., García-Haro, F. J., Martínez, B., and Gilabert, M. A. (2014). Noise reduction and gap filling of fapar time series using an adapted local regression filter. *Remote Sensing*, 6(9):8238–8260. 112

[116] Mutanga, O., Adam, E., and Cho, M. A. (2012). High density biomass estimation for wetland vegetation using WorldView-2 imagery and random forest regression algorithm. *International Journal of Applied Earth Observation and Geoinformation*, 18:399 – 406. 12

[117] Myers-Smith, I. H., Forbes, B. C., Wilmking, M., Hallinger, M., Lantz, T., Blok, D., Tape, K. D., Macias-Fauria, M., Sass-Klaassen, U., Lèvesque, E., Boudreau, S., Ropars, P., Hermanutz, L., Trant, A., Collier, L. S., Weijers, S., Rozema, J., Rayback, S. A., Schmidt, N. M., Schaepman-Strub, G., Wipf, S., Rixen, C., Mènard, C. B., Venn, S., Goetz, S., Andreu-Hayles, L., Elmendorf, S., Ravolainen, V., Welker, J., Grogan, P., Epstein, H. E., and Hik, D. S. (2011). Shrub expansion in tundra ecosystems: dynamics, impacts and research priorities. *Environ. Res. Lett.*, 6(4):045509. 10

[118] Narita, K., Harada, K., Saito, K., Sawada, Y., Fukuda, M., and Tsuyuzaki, S. (2015). Vegetation and Permafrost Thaw Depth 10 Years after a Tundra Fire in 2002, Seward Peninsula, Alaska. *Arctic, Antarctic, and Alpine Research*, 47(3):547–559. 48, 74

[119] Ogden, L. E. (2015). Plants Duke It Out in a Warming Arctic. *BioScience*. 46, 70

[120] Oleson, K. W., Lawrence, D. M., Bonan, G. B., Drewniak, B., Huang, M., Koven, C. D., Levis, S., Li, F., Riley, W. J., Subin, Z. M., Swenson, S. C., Thornton, P. E., Bozbiyik, A., Fisher, R., Heald, C. L., Kluzek, E., Lamarque, J.-F., Lawrence, P. J., Leung, L. R., Lipscomb, W., Muszala, S., Ricciuto, D. M., Sacks, W., Sun, Y., Tang, J., and Yang, Z.-L. (2013). Technical description of version 4.5 of the Community Land Model (CLM). In *NCAR Technical Note*, page 420 pp, Boulder, CO, USA. NCAR/TN-503+STR. 11

[121] Oliveira, S., Oehler, F., San-Miguel-Ayanz, J., Camia, A., and Pereira, J. M. (2012). Modeling spatial patterns of fire occurrence in Mediterranean Europe using Multiple Regression and Random Forest. *Forest Ecology and Management*, 275:117 – 129. 107

[122] Overland, J. E., Wang, M., Walsh, J. E., and Stroeve, J. C. (2014). Future Arctic climate changes: Adaptation and mitigation time scales. *Earth's Future*, 2(2):68–74. 2, 46, 70, 130

[123] Pal, M. (2005). Random forest classifier for remote sensing classification. *International Journal of Remote Sensing*, 26(1):217–222. 113

[124] Panboonyuen, T., Jitkajornwanich, K., Lawawirojwong, S., Srestasathiern, P., and Vateekul, P. (2017). Road Segmentation of Remotely-Sensed Images Using Deep Convolutional Neural Networks with Landscape Metrics and Conditional Random Fields. *Remote Sensing*, 9(7). 66

[125] Park, T., Ganguly, S., Tømmervik, H., Euskirchen, E. S., Høgda, K.-A., Karlsen, S. R., Brovkin, V., Nemani, R. R., and Myneni, R. B. (2016). Changes in growing season duration and productivity of northern vegetation inferred from long-term remote sensing data. *Environmental Research Letters*, 11(8):084001. 124

[126] Parmentier, B. (2014). Characterization of Land Transitions Patterns from Multivariate Time Series Using Seasonal Trend Analysis and Principal Component Analysis. *Remote Sensing*, 6(12):12639. 4

[127] Pearson, R. G., Phillips, S. J., Loranty, M. M., Beck, P. S. A., Damoulas, T., Knight, S. J., and Goetz, S. J. (2013). Shifts in Arctic vegetation and associated feedbacks under climate change. *Nature Clim. Change*, 3(7):673–677. 2, 3, 70

[128] Pedregosa, F., Varoquaux, G., Gramfort, A., Michel, V., Thirion, B., Grisel, O., Blondel, M., Prettenhofer, P., Weiss, R., Dubourg, V., Vanderplas, J., Passos, A., Cournapeau, D., Brucher, M., Perrot, M., and Duchesnay, E. (2011). Scikit-learn: Machine learning in Python. *Journal of Machine Learning Research*, 12:2825–2830. 84, 113, 114

[129] Pfister, G., Hess, P. G., Emmons, L. K., Lamarque, J.-F., Wiedinmyer, C., Edwards, D. P., Pétron, G., Gille, J. C., and Sachse, G. W. (2005). Quantifying CO emissions from the 2004 Alaskan wildfires using MOPITT CO data. *Geophysical Research Letters*, 32(11):n/a–n/a. L11809. 105

[130] Poulter, B., Ciais, P., Hodson, E., Lischke, H., Maignan, F., Plummer, S., and Zimmermann, N. E. (2011). Plant functional type mapping for Earth system models. *Geoscientific Model Development*, 4(4):993–1010. 11

[131] Racine, C., Jandt, R., Meyers, C., and Dennis, J. (2004). Tundra Fire and Vegetation Change along a Hillslope on the Seward Peninsula, Alaska, U.S.A. *Arctic, Antarctic, and Alpine Research*, 36(1):1–10. 48

[132] Ramoelo, A., Cho, M., Mathieu, R., Madonsela, S., van de Kerchove, R., Kaszta, Z., and Wolff, E. (2015). Monitoring grass nutrients and biomass as indicators of rangeland quality and quantity using random forest modelling and WorldView-2 data. *International Journal of Applied Earth Observation and Geoinformation*, 43:43 – 54. 12

[133] Raynolds, M. K., Walker, D. A., and Maier, H. A. (2005). Plant community-level mapping of arctic Alaska based on the Circumpolar Arctic Vegetation Map. *Phytocoenologia*, 35(4):821–848. 77

[134] Regmi, P., Grosse, G., Jones, M. C., Jones, B. M., and Anthony, K. W. (2012). Characterizing Post-Drainage Succession in Thermokarst Lake Basins on the Seward Peninsula, Alaska with TerraSAR-X Backscatter and Landsat-based NDVI Data. *Remote Sensing*, 4(12):3741. 4

[135] Reiche, J., de Bruin, S., Hoekman, D., Verbesselt, J., and Herold, M. (2015). A Bayesian Approach to Combine Landsat and ALOS PALSAR Time Series for Near Real-Time Deforestation Detection. *Remote Sensing*, 7(5):4973. 123

[136] Ren, J., Campbell, J. B., and Shao, Y. (2017). Estimation of SOS and EOS for Midwestern US Corn and Soybean Crops. *Remote Sensing*, 9(7). 112

[137] Richardson, A. D., Keenan, T. F., Migliavacca, M., Ryu, Y., Sonnentag, O., and Toomey, M. (2013). Climate change, phenology, and phenological control of vegetation feedbacks to the climate system. *Agricultural and Forest Meteorology*, 169:156 – 173. 12

[138] Ringaby, E., Friman, O., Forssén, P.-E., Opsahl, T., Haavardsholm, T. V., and Kåsen, I. (2014). Anisotropic scattered data interpolation for pushbroom image rectification. *IEEE Trans. Image Process.*, 23(5):2302–2314. 24

[139] Ronneberger, O., Fischer, P., and Brox, T. (2015). U-net: Convolutional networks for biomedical image segmentation. *CoRR*, abs/1505.04597. 56, 57, 66, 99

[140] Rosenqvist, A., Finlayson, C. M., Lowry, J., and Taylor, D. (2007). The potential of long-wavelength satellite-borne radar to support implementation of the ramsar wetlands convention. *Aquatic Conservation: Marine and Freshwater Ecosystems*, 17(3):229–244. 71

[141] Rouse, J., Haas, R., Schell, J., and Deering, D. (1974). Monitoring vegetation systems in the Great Plains with ERTS-1. In *3rd Earth Resources Technology Satellite Symposium*, pages 309–317, Washington, D.C., USA. NASA. 19, 106

[142] Rowland, J., Jones, C., Altmann, G., Bryan, R., Crosby, B., Hinzman, L., Kane, D., Lawrence, D., Mancino, A., Marsh, P., McNamara, J., Romanovsky, V., Toniolo, H., Travis, B., Trochim, E., Wilson, C., and Geernaert, G. (2010). Arctic landscapes in transition: responses to thawing permafrost. *Eos Trans. AGU*, 91(Issue 26):229 – 236. 2, 10

[143] Rupp, T. S., Chapin, F. S., and Starfield, A. M. (2000). Response of subarctic vegetation to transient climatic change on the Seward Peninsula in north-west Alaska. *Global Change Biology*, 6(5):541–555. 70

[144] Santoro, M., Eriksson, L. E., and Fransson, J. E. (2015). Reviewing ALOS PALSAR Backscatter Observations for Stem Volume Retrieval in Swedish Forest. *Remote Sensing*, 7(4):4290. 97

[145] Schaefer, K. and Jafarov, E. (2016). A parameterization of respiration in frozen soils based on substrate availability. *Biogeosciences*, 13(7):1991–2001. 4

[146] Schaefer, K., Lantuit, H., Romanovsky, V., and Schuur, E. A. G. (2012). *Policy Implications of Warming Permafrost*. United Nations Environment Programme Special Report, Nairobi, Kenya. 2

[147] Schaefer, K., Lantuit, H., Romanovsky, V. E., Schuur, E. A. G., and Witt, R. (2014). The impact of the permafrost carbon feedback on global climate. *Environmental Research Letters*, 9(8):085003. 3

[148] Schuur, E. A. G., McGuire, A. D., Schädel, C., Grosse, G., Harden, J. W., Hayes, D. J., Hugelius, G., Koven, C. D., Kuhry, P., Lawrence, D. M., Natali, S. M., Olefeldt, D., Romanovsky, V. E., Schaefer, K., Turetsky, M. R., Treat, C. C., and Vonk, J. E. (2015). Climate change and the permafrost carbon feedback. *Nature*, 520(8):171–179. 46, 70

[149] Selkowitz, D. J. (2010). A comparison of multi-spectral, multi-angular, and multi-temporal remote sensing datasets for fractional shrub canopy mapping in arctic alaska. *Remote Sensing of Environment*, 114(7):1338 – 1352. 12

[150] Shen, W., Li, M., Huang, C., and Wei, A. (2016). Quantifying Live Aboveground Biomass and Forest Disturbance of Mountainous Natural and Plantation Forests in Northern Guangdong, China, Based on Multi-Temporal Landsat, PALSAR and Field Plot Data. *Remote Sensing*, 8(7). 107

[151] Shimada, M., Itoh, T., Motooka, T., Watanabe, M., Shiraishi, T., Thapa, R., and Lucas, R. (2014). New global forest/non-forest maps from ALOS PALSAR data (2007–2010). *Remote Sensing of Environment*, 155:13 – 31. 78

[152] Silapaswan, C., Verbyla, D., and McGuire, A. (2001). Land Cover Change on the Seward Peninsula: The Use of Remote Sensing to Evaluate the Potential Influences of Climate Warming on Historical Vegetation Dynamics. *Canadian Journal of Remote Sensing*, 27(5):542–554. 48, 74

[153] Simonetti, D., Simonetti, E., Szantoi, Z., Lupi, A., and Eva, H. (2015). First Results From the Phenology-Based Synthesis Classifier Using Landsat 8 Imagery. *Geoscience and Remote Sensing Letters, IEEE*, 12(7):1496–1500. 107

[154] Sloan, V., Brooks, J., Wood, S., Liebig, J., Siegrist, J., Iversen, C., and Norby, R. (2014). Plant community composition and vegetation height, Barrow, Alaska, Ver. 1. Next Generation Ecosystem Experiments Arctic Data Collection, Carbon Dioxide Information Analysis Center, Oak Ridge National Laboratory, Oak Ridge, Tennessee, USA. Data set accessed at http://dx.doi.org/10.5440/1129476. 42

[155] Small, D. (2011). Flattening gamma: Radiometric terrain correction for sar imagery. *Geoscience and Remote Sensing, IEEE Transactions on*, 49(8):3081–3093. 78

[156] Smith, T. M., Shugart, H. H., and Woodward, F. I. (1997). *Plant Functional Types: Their Relevance to Ecosystem Properties and Global Change*. Cambridge University Press. 11

[157] Soja, A. J., Tchebakova, N. M., French, N. H., Flannigan, M. D., Shugart, H. H., Stocks, B. J., Sukhinin, A. I., Parfenova, E., III, F. S. C., and Jr., P. W. S. (2007). Climate-induced boreal forest change: Predictions versus current observations. *Global and Planetary Change*, 56(3–4):274 – 296. Northern Eurasia Regional Climate and Environmental Change. 105

[158] Stewart, L., Alsos, I. G., Bay, C., Breen, A. L., Brochmann, C., Boulanger-Lapointe, N., Broennimann, O., Bültmann, H., Bøcher, P. K., Damgaard, C., Daniëls, F. J. A., Ehrich, D., Eidesen, P. B., Guisan, A., Jónsdóttir, I. S., Lenoir, J., le Roux, P. C., Lévesque, E., Luoto, M., Nabe-Nielsen, J., Schönswetter, P., Tribsch, A., Tveraabak, L. U., Virtanen, R., Walker, D. A., Westergaard, K. B., Yoccoz, N. G., Svenning, J.-C., Wisz, M., Schmidt, N. M., and Pellissier, L. (2016). The regional species richness and genetic diversity of Arctic vegetation reflect both past glaciations and current climate. *Global Ecology and Biogeography*, 25(4):430–442. 46, 70

[159] Stocker, T., Qin, D., Plattner, G.-K., Tignor, M., Allen, S., Boschung, J., Nauels, A., Xia, Y., Bex, V., and Midgley, P., editors (2013a). *Climate Change 2013: The*

Physical Science Basis. Contribution of Working Group I to the Fifth Assessment Report of the Intergovernmental Panel on Climate Change, Cambridge, United Kingdom and New York, NY, USA. Cambridge University Press. 46, 104, 142

[160] Stocker, T. F., Dahe, Q., and Plattner, G.-K. (2013b). Climate change 2013: The physical science basis. *Working Group I Contribution to the Fifth Assessment Report of the Intergovernmental Panel on Climate Change. Summary for Policymakers (IPCC, 2013)*. 70

[161] Stow, D. A., Hope, A., McGuire, D., Verbyla, D., Gamon, J., Huemmrich, F., Houston, S., Racine, C., Sturm, M., Tape, K., Hinzman, L., Yoshikawa, K., Tweedie, C., Noyle, B., Silapaswan, C., Douglas, D., Griffith, B., Jia, G., Epstein, H., Walker, D., Daeschner, S., Petersen, A., Zhou, L., and Myneni, R. (2004). Remote sensing of vegetation and land-cover change in Arctic Tundra Ecosystems. *Remote Sensing of Environment*, 89(3):281 – 308. 12, 42, 105

[162] Sun, W., Liang, S., Xu, G., Fang, H., and Dickinson, R. (2008). Mapping plant functional types from MODIS data using multi-source evidential reasoning. *Remote Sensing of Environment*, 112:1010–1024. 11

[163] Szegedy, C., Vanhoucke, V., Ioffe, S., Shlens, J., and Wojna, Z. (2015). Rethinking the Inception Architecture for Computer Vision. *CoRR*, abs/1512.00567. 54, 73

[164] Tan, Z., Liu, S., Wylie, B., Jenkerson, C., Oeding, J., Rover, J., and Young, C. (2013). MODIS-informed greenness responses to daytime land surface temperature fluctuations and wildfire disturbances in the Alaskan Yukon River Basin. *International Journal of Remote Sensing*, 34(6):2187–2199. 106

[165] Tang, G., Yuan, F., Bisht, G., Hammond, G. E., Lichtner, P. C., Kumar, J., Mills, R. T., Xu, X., Andre, B., Hoffman, F. M., Painter, S. L., and Thornton, P. E. (2016). Addressing numerical challenges in introducing a reactive transport code into a land surface model: a biogeochemical modeling proof-of-concept with CLM–PFLOTRAN 1.0. *Geoscientific Model Development*, 9(3):927–946. 11, 71

[166] Thenkabail, P. S., Lyon, J. G., and Huete, A. (2011). *Hyperspectral Remote Sensing of Vegetation*. CRC Press. 47, 72

[167] Thornton, P. E., Running, S. W., and White, M. A. (1997). Generating surfaces of daily meteorological variables over large regions of complex terrain. *Journal of Hydrology*, 190(3):214 – 251. Aggregate Description of Land-Atmosphere Interactions. 106

[168] Tranvik, L. (2014). Carbon cycling in the Arctic. *Science*, 345(6199):870. 70

[169] Tucker, C. J. (1979). Red and photographic infrared linear combinations for monitoring vegetation. *Remote Sensing of Environment*, 8(2):127 – 150. 106

[170] Ueyama, M., Ichii, K., Iwata, H., Euskirchen, E. S., Zona, D., Rocha, A. V., Harazono, Y., Iwama, C., Nakai, T., and Oechel, W. C. (2013a). Upscaling terrestrial carbon dioxide fluxes in Alaska with satellite remote sensing and support vector regression. *Journal of Geophysical Research: Biogeosciences*, 118(3):1266–1281. 5

[171] Ueyama, M., Iwata, H., Harazono, Y., Euskirchen, E. S., Oechel, W. C., and Zona, D. (2013b). Growing season and spatial variations of carbon fluxes of Arctic and boreal ecosystems in Alaska (USA). *Ecological Applications*, 23(8):1798–1816. 105, 108

[172] Updike, T. and Comp, C. (2010). Radiometric Use of WorldView-2 Imagery. In *Technical Note*, Longmont, Colorado, USA. DigitalGlobe, Inc. 18

[173] Ustin, S. L. and Gamon, J. A. (2010). Remote sensing of plant functional types. *New Phytologist*, 186(4):795–816. 11

[174] Veraverbeke, S., Verstraeten, W. W., Lhermitte, S., Van De Kerchove, R., and Goossens, R. (2012). Assessment of post-fire changes in land surface temperature and surface albedo, and their relation with fire-burn severity using multitemporal MODIS imagery. *INTERNATIONAL JOURNAL OF WILDLAND FIRE*, 21(3):243–256. 4

[175] Verbesselt, J., Zeileis, A., and Herold, M. (2012). Near real-time disturbance detection using satellite image time series. *Remote Sensing of Environment*, 123:98 – 108. 106

[176] Verbyla, D. (2015). Comparison of emodis and mod/myd13a2 {NDVI} products during 2012–2014 spring green-up periods in alaska and northwest canada. *International Journal of Applied Earth Observation and Geoinformation*, 36:83 – 86. 111

[177] Viereck, L. A. (1992). *The Alaska Vegetation Classification*. General technical report. USDA Pacific Northwest Research Station. 48, 51, 74, 76

[178] Villarreal, S., Hollister, R. D., Johnson, D. R., Lara, M. J., Webber, P. J., and Tweedie, C. E. (2012). Tundra vegetation change near Barrow, Alaska (1972–2010). *Environmental Research Letters*, 7(1):015508. 42

[179] Walker, D. A., Breen, A. L., Druckenmiller, L. A., Wirth, L. W., Fisher, W., Raynolds, M. K., Sibík, J., Walker, M. D., Hennekens, S., Boggs, K., Boucher, T., Buchhorn, M., Bültmann, H., Cooper, D. J., Daniëls, F. J., Davidson, S. J., Ebersole, J. J., Elmendorf, S. C., Epstein, H. E., Gould, W. A., Hollister, R. D., Iversen, C. M., Jorgenson, M. T., Kade, A., Lee, M. T., MacKenzie, W. H., Peet, R. K., Peirce, J. L., Schickhoff, U., Sloan, V. L., Talbot, S. S., Tweedie, C. E., Villarreal, S., Webber, P. J., and Zona, D. (2016). The Alaska Arctic Vegetation Archive (AVA-AK). *Phytocoenologia*, 46(2):221–229. 77

[180] Walker, J., de Beurs, K., and Henebry, G. (2015). Land surface phenology along urban to rural gradients in the U.S. Great Plains. *Remote Sensing of Environment*, 165:42 – 52. 13

[181] Wang, T., Zhang, H., Lin, H., and Fang, C. (2016). Textural–Spectral Feature-Based Species Classification of Mangroves in Mai Po Nature Reserve from Worldview-3 Imagery. *Remote Sensing*, 8(1):24. 98

[182] Washburn, A. L. (1978). *Geocryology, A Survey of Periglacial Processes and Environments*. Edward Arnold. 16

[183] Welp, L., Randerson, J., and Liu, H. (2007). The sensitivity of carbon fluxes to spring warming and summer drought depends on plant functional type in boreal forest ecosystems. *Agricultural and Forest Meteorology*, 147(3):172 – 185. 124

[184] Wu, H. and Prasad, S. (2017). Convolutional Recurrent Neural Networks for Hyperspectral Data Classification. *Remote Sensing*, 9(3). 55

[185] Wullschleger, S. D., Epstein, H. E., Box, E. O., Euskirchen, E. S., Goswami, S., Iversen, C. M., Kattge, J., Norby, R. J., van Bodegom, P. M., and Xu, X. (2014). Plant functional types in Earth system models: past experiences and future directions for application of dynamic vegetation models in high-latitude ecosystems. *Annals of Botany*, 114(1):1–16. 11

[186] Wylie, B., Rigge, M., Brisco, B., Murnaghan, K., Rover, J., and Long, J. (2014). Effects of Disturbance and Climate Change on Ecosystem Performance in the Yukon River Basin Boreal Forest. *Remote Sensing*, 6(10):9145–9169. 124

[187] Yi, Y., Kimball, J. S., Jones, L. A., Reichle, R. H., Nemani, R., and Margolis, H. A. (2013). Recent climate and fire disturbance impacts on boreal and arctic ecosystem productivity estimated using a satellite-based terrestrial carbon flux model. *Journal of Geophysical Research: Biogeosciences*, 118(2):606–622. 105

[188] Yu, Q., Wang, S., Mickler, R. A., Huang, K., Zhou, L., Yan, H., Chen, D., and Han, S. (2014). Narrowband Bio-Indicator Monitoring of Temperate Forest Carbon Fluxes in Northeastern China. *Remote Sensing*, 6(9):8986–9013. 72

[189] Zeiler, M. D. and Fergus, R. (2013). Visualizing and Understanding Convolutional Networks. *CoRR*, abs/1311.2901. 54, 55, 56, 83

[190] Zhang, L., Zhang, L., and Du, B. (2016). Deep Learning for Remote Sensing Data: A Technical Tutorial on the State of the Art. *IEEE Geoscience and Remote Sensing Magazine*, 4(2):22–40. 54, 55, 73

[191] Zhang, P., Niu, X., Dou, Y., and Xia, F. (2017). Airport Detection on Optical Satellite Images Using Deep Convolutional Neural Networks. *IEEE Geoscience and Remote Sensing Letters*, PP(99):1–5. 55

[192] Zhang, W., Miller, P. A., Smith, B., Wania, R., Koenigk, T., and Döscher, R. (2013). Tundra shrubification and tree-line advance amplify arctic climate warming: results from an individual-based dynamic vegetation model. *Environmental Research Letters*, 8(3):034023. 46, 70

Appendices

Appendix A

Surface Water Analysis

Provided here is a description of possible surface water conditions within the WorldView-2 satellite images and impacts on the IDW model. No *in situ* estimates for surface water conditions during the 2012 vegetation sampling campaign or for the 2010 WorldView-2 images were recorded. For inundated areas in the sampling plots, the observed PFT fraction included the vegetation above and below the surface water. The Normalized Difference Surface Water Index (NDSWI) was used to estimate surface water conditions for the 2010 WorldView-2 images used for the *with phenology* case and one image on 2012 July 19, a period during the vegetation sampling time (Figure A.1). NDSWI is a proxy of water table height and works in shallow water bodies [50]. A few images in the *with phenology* case (2010 June 24, 2010 July 21, and 2010 July 26) were possibly inundated with high NDSWI values. This is especially true for Area A and Area D dominated by the low center polygons. The image on 2012 July 19 looks dry with low NDSWI values, which corresponds to the visual estimates and photographs made in the field around this time (Figure 2.3 d). The IDW upscaling model was applied using the 2012 July 19 WorldView-2 spectral characteristics to estimate PFT distribution. The ground-truthing dataset, used in the manuscript, was applied to these PFT distributions and the correlation coefficient was lower (R^2=0.69) than the *with phenology* PFT distributions. Also, the R^2 values in the wet sampling areas (A and D) were higher (0.85 and 0.72, respectively) in the *with phenology* case compared to the 2012 July 19 image (0.75 and 0.68, respectively).

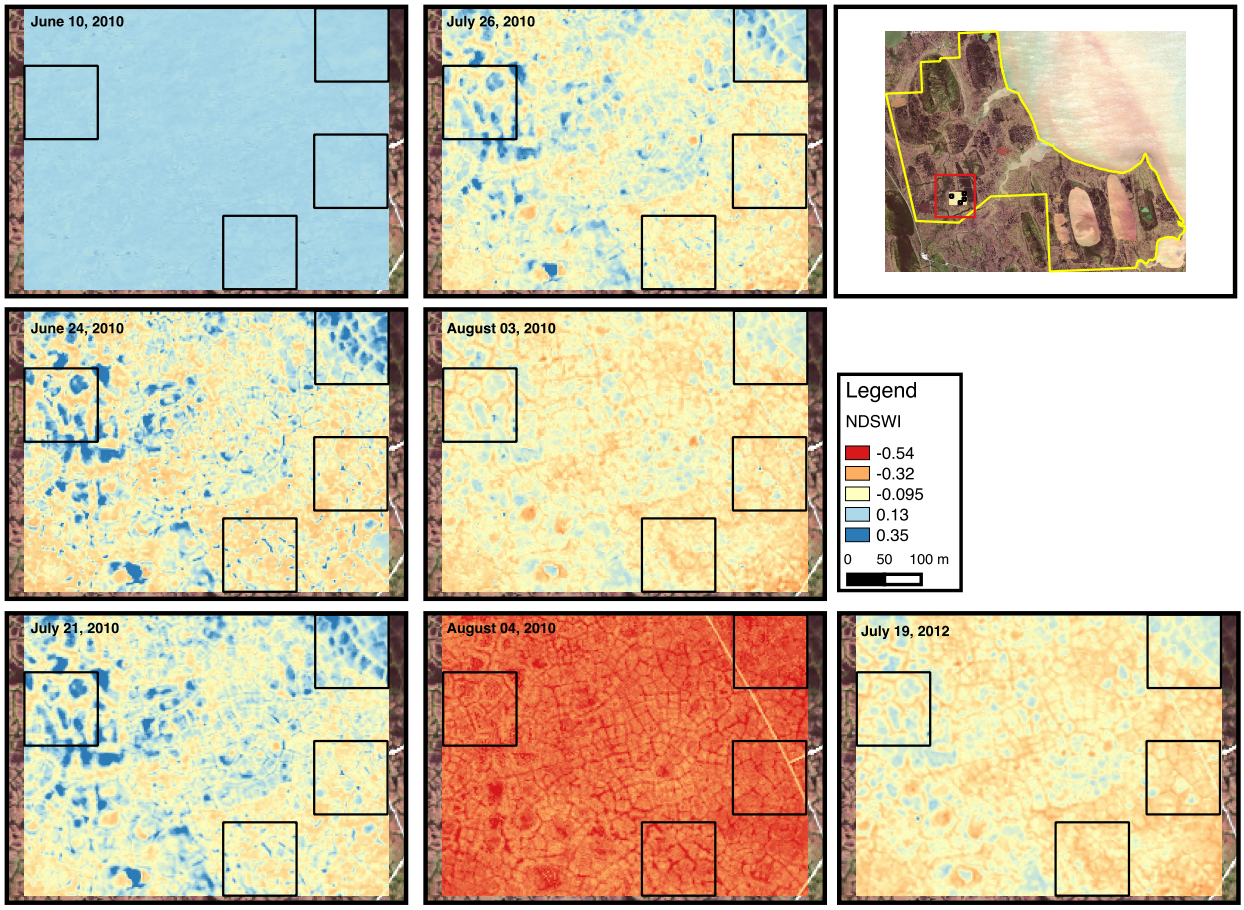


Figure A.1: NDSWI values for areas A, B, C, and D for 2010 WorldView-2 images (June 10, June 24, July 21, July 26, August 03, and August 04) and one WorldView-2 image in 2012 July 19.

Vita

Zachary L. Langford was born and raised in Jackson, Mississippi. He received his Bachelor of Science in Earth System Science from the University of Alabama-Huntsville in 2011. He went on to graduate school at Pennsylvania State University, receiving a Master's Degree in Civil Engineering in 2013 with a Master's Thesis title "Are the Dry Valleys Getting Wetter? A Preliminary Assessment of Wetness Across the McMurdo Dry Valleys Landscape" under the direction of Michael N. Gooseff. He then started an internship at Oak Ridge National Laboratory with the Environmental Sciences Division, where he worked on projects related to image processing and data analytics in Arctic ecosystems. He continued his research pursuing a PhD degree in Energy Science and Engineering at the University of Tennessee-Knoxville. He plans to continue his research in applying innovative machine learning and data mining algorithms to environmental datasets.